学位論文

Origin of the Diffuse Near-Infrared Radiation
Observed with *COBE*/DIRBE
(*COBE*/DIRBE により観測された
近赤外線拡散放射の起源)

平成 28 年 12 月博士（理学）申請

東京大学大学院理学系研究科
天文学専攻
佐野　圭

ii

Abstract

Near-infrared (IR) diffuse sky brightness is contributed from zodiacal light (ZL), integrated starlight (ISL), diffuse Galactic light (DGL), and diffuse isotropic light including extragalactic background light (EBL). The diffuse near-IR radiation was studied by all-sky maps obtained with the Diffuse Infrared Background Experiment (DIRBE) onboard *Cosmic Background Explorer* (*COBE*). In the previous analysis, however, large ISL uncertainty in a star-counts model caused non-detection of the DGL and diffuse isotropic light. In this thesis, the diffuse near-IR radiation is reanalyzed by improving the ISL evaluation.

In the present analysis, DIRBE all-sky maps at 1.25, 2.2, 3.5, and $4.9\,\mu$m are used as total diffuse near-IR brightness. To improve the ISL evaluation, star catalogs based on Two Micron All-Sky Survey (2MASS) and *Wide-field Infrared Survey Explorer* (*WISE*) are used. As a result, the DIRBE sky brightness is decomposed into the ZL, DGL, ISL, and diffuse isotropic light in high Galactic latitudes.

The near-IR DGL consists of scattered light and thermal emission from interstellar dust. Using the DGL result at $3.5\,\mu$m, mass fraction of very small grains and polycyclic aromatic hydrocarbon is constrained to be $\sim 2\%$–8%. The scattered light observed at 1.25 and $2.2\,\mu$m is redder than that expected from a current dust model. This trend may suggest the presence of larger dust grains in the diffuse interstellar medium.

At 1.25 and $2.2\,\mu$m, intensity ratios of the DGL to $100\,\mu$m emission are found to increase toward low Galactic latitudes. The observed latitude dependence is steeper than a scattered light model in which the scattering phase function reproduces a current dust model. This may imply stronger forward scattering by larger grains, which is consistent with the implication from the redder spectrum of the scattered light.

The diffuse isotropic light obtained at 1.25 and 2.2 μm is several times larger than integrated galaxy light and EBL limit derived from high-energy γ-ray observation, indicating local origin of the excess light. To explain the excess, hypothetical interplanetary dust distributed around the Sun is introduced. Additional 5%–10% density relative to the known interplanetary dust can explain the excess light. In the future, observation outside the Earth orbit will be useful to confirm the origin of the diffuse isotropic light.

Contents

List of Figures

viii

List of Tables

Chapter 1

Introduction

1.1 Historical review of diffuse light study

In the astrophysical study, observations of discrete sources, such as individual stars and galaxies, have been mainly conducted. In addition, diffuse measurements are important for understanding astrophysical phenomena, which are associated with dust and unresolved objects such as faint galaxies. Figure 1.1 illustrates the spectra of the diffuse sky emission components observed from the ground, where the atmospheric airglow is dominant. When observing from space, diffuse light includes zodiacal light (ZL), faint stars (integrated starlight: ISL), interstellar dust emission (Galactic cirrus), and extragalactic background light (EBL). The ZL includes the scattered sunlight and thermal emission from interplanetary dust (IPD). Galactic cirrus comprises scattered light and thermal emission from interstellar dust grains, so called diffuse Galactic light (DGL). The EBL consists of light emitted from entire extragalactic objects.

In this section, history and scientific values of the ZL, DGL, and EBL observation are reviewed. To avoid the airglow contamination, satellites and rocket-borne experiments have carried out the observations. Throughout the thesis, "ultraviolet (UV)", "optical", "near-infrared (IR)", "mid-IR", and "far-IR" indicate, respectively, the wavelength ranges ~ 0.1–$0.3\,\mu$m, ~ 0.4–$1.0\,\mu$m, ~ 1–$5\,\mu$m, ~ 5–$50\,\mu$m, and ~ 50–$300\,\mu$m. In addition, the word "DGL" is defined as the Galactic scattered light and thermal emission observed from UV to near-IR.

1.1.1 Zodiacal light

Over three centuries ago, Cassini (1685) observed the visual pattern of night-sky brightness and first formulated the hypothesis of the IPD cloud. He thought the lenticular dust

1
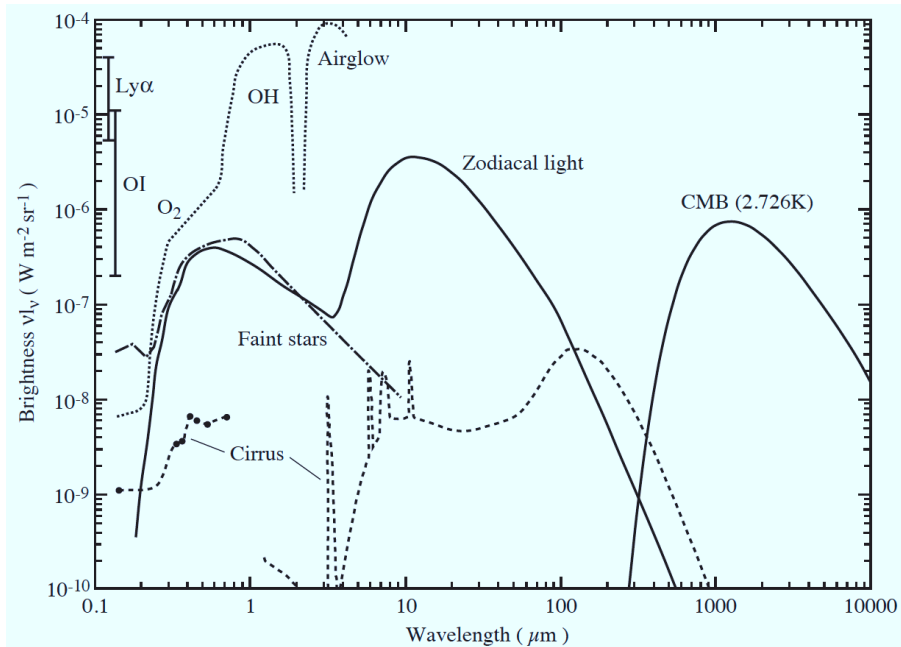
Figure 1.1 Overview on the sky brightness outside the lower terrestrial atmosphere and at high ecliptic and Galactic latitudes (Leinert et al. 1998). The ZL and ISL are derived in the south ecliptic pole ($l = 276°$, $b = -30°$). The bright magnitude cut-off for the stellar component is $V = 6.0$ mag for 0.3–1 μm. In the IR, stars brighter than 15 Jy between 1.25 and 4.85 μm and brighter than 85 Jy at 12 μm are excluded. No cut-off was applied to the UV data ($\lambda < 0.3 \,\mu$m). The interstellar cirrus component is normalized for a hydrogen column density of 10^{20} cm^{-2} corresponding to a visual extinction of 0.053 mag. Sources for $\lambda > 1.25 \,\mu$m come from the *COBE*/DIRBE and *COBE*/FIRAS measurements (Désert et al. 1996). The IR cirrus spectrum represents the model fitted to the *IRAS* photometry (Désert et al. 1990). The short-wavelength data, $\lambda < 1.0 \,\mu$m, are from the following sources: ZL: Leinert & Grün (1990); ISL: Gondhalekar (1990), Mattila (1979). The geocoronal Lyman α (121.6 nm) and the OI (130.4, 135.6 nm) line intensities were measured with the Faint Object Camera of *HST* at a height of 610 km (Caulet et al. 1994).

2
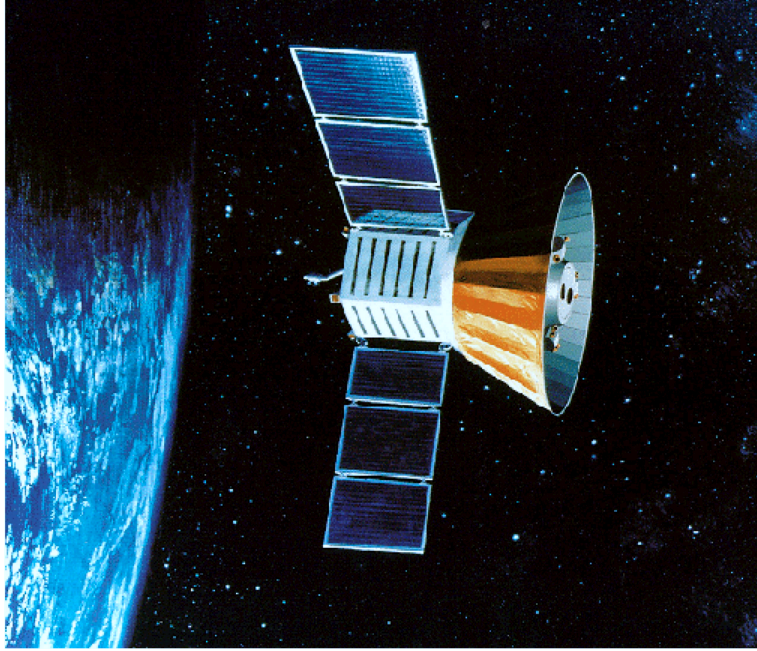
Figure 1.2 Illustration of the *COBE* satellite (image credit: NASA).

distribution centered at the Sun with its major axis lying in the ecliptic plane. After that, Struve (1943) presented another interpretation of the IPD structure. He assumed the IPD distribution as prolate spheroid surrounded by dust torus surrounded by fragmentation of asteroids in the asteroid belt.

In 1980s, *Infrared Astronomical Telescope* (*IRAS*) observed the sky in wavelengths range of 12–100 μm and investigated the thermal emission component of the ZL. The *IRAS* data revealed the structure of asteroidal dust bands in addition to the smooth IPD cloud (Low et al. 1984; Spiesman et al. 1995). In addition, theoretical studies predicted the presence of the circumsolar ring that was constructed by the IPD trapped in the Earth orbit (e.g., Dermott et al. 1994).

After *IRAS*, NASA launched the *CosmicBackgroundExplorer* (*COBE*) satellite in the late 1990s (Figure 1.2). The Diffuse Infrared Background Experiment (DIRBE) onboard *COBE* observed all sky in 10 broad photometric bands from 1.25–240 μm. Over a 10 months observation with solar elongation angle of 64°–124° provided valuable data for studying the scattered light component of the ZL as well as the thermal emission. Figure 1.3 shows 1.25 μm all-sky map created by the DIRBE observation. At this point, Reach et al. (1995) revealed the presence of circumsolar ring, using the DIRBE data with a simple IPD model.
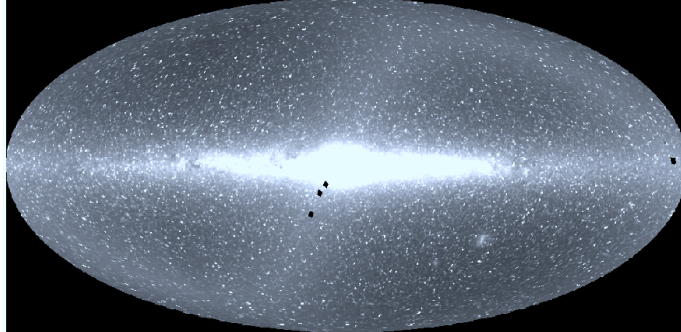
Figure 1.3 All-sky DIRBE $\epsilon = 90°$ intensity map at $1.25\,\mu$m in Galactic Mollweide projection with the Galactic center in the middle. The "S" shape indicates the ecliptic plane.

Since the primary purpose of DIRBE was measuring the IR EBL, the brightest foreground emission, ZL must be removed precisely. By fitting the physical IPD model to the time variation of the DIRBE brightness, Kelsall et al. (1998) modeled the ZL intensity as a function of observation time (t) and sky coordinates (i.e., DIRBE pixel number p):

$$I_\lambda(p,t) = \sum_c \int n_c(X,Y,Z)[A_{c,\lambda}\,F_\lambda^\odot\,\phi_\lambda(\theta) + (1 - A_{c,\lambda})\,E_{c,\lambda}\,B_\lambda(T)\,K_\lambda(T)]ds, \qquad (1.1)$$

where $n_c(X,Y,Z)$ is the three-dimensional density of each IPD component c, i.e., smooth cloud, dust bands, and circumsolar ring. By adopting the solar flux $F_\lambda^\odot$, the IPD properties are characterized by albedo $A_{c,\lambda}$, scattering phase function $\phi_\lambda(\theta)$, emissivity modification factor $E_{c,\lambda}$, Planck function $B_\lambda(T)$, and color correction factor $K_\lambda(T)$ with the dust temperature T. The first and second terms in Equation (1.1) thus represent the intensity of scattered sunlight and thermal emission from the IPD, respectively. Figure 1.4 shows the density distribution of each IPD component determined by this method (Kelsall et al. 1998). Hereafter, this IPD model is referred to as "DIRBE ZL model".

After *COBE*/DIRBE, the *AKARI* satellite conducted all-sky survey from mid to far-IR wavelength range (Murakami et al. 2007). Adopting strategy similar to DIRBE, ZL models have been created by Kondo et al. (2016) and Ootsubo et al. (2016) from the all-sky maps taken by Infrared Camera (IRC: Onaka et al. 2007) and Far-Infrared Surveyor (FIS: Kawada et al. 2007), respectively. Since the spatial resolution of *AKARI* is much higher

a) Cloud + Bands + Ring

b) Cloud Only

[0.2, 0.4, 0.6, 0.8, 1.0, 1.2, 1.4, 1.6, 1.8, 2.0]

c) Bands Only

d) Ring Only

Height Above Ecliptic Plane (AU)

Distance from Sun in Ecliptic Plane (AU)
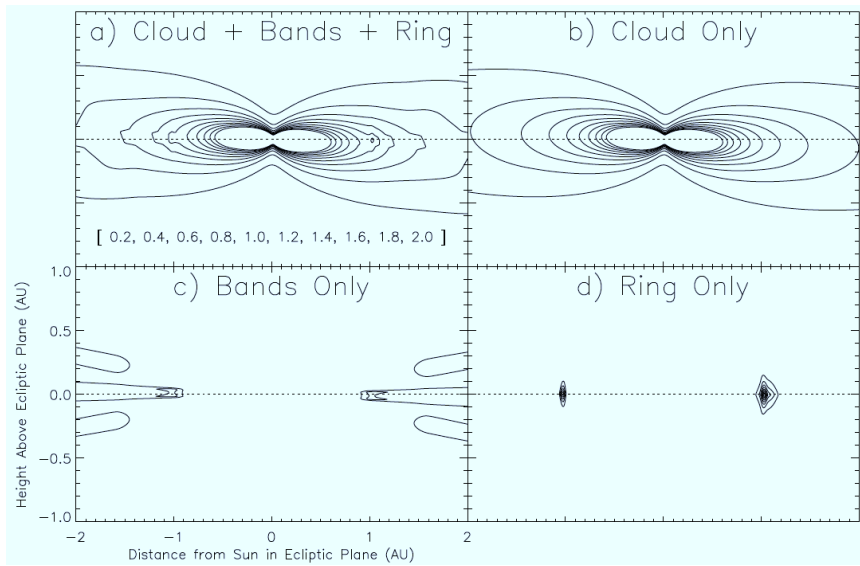
Figure 1.4 Three-dimensional distribution of the IPD components (Kelsall et al. 1998). Isodensity contours of the IPD model components, shown for a cross-sectional slice perpendicular to the ecliptic plane: (a) all components; (b) smooth cloud; (c) dust bands; (d) circumsolar ring. The density contour levels used in (a) and (b) are listed in brackets at the bottom of (a), in units of $10^{-7}\,\mathrm{AU}^{-1}$. Contour levels used in (c) and (d) are a factor of 8 smaller.
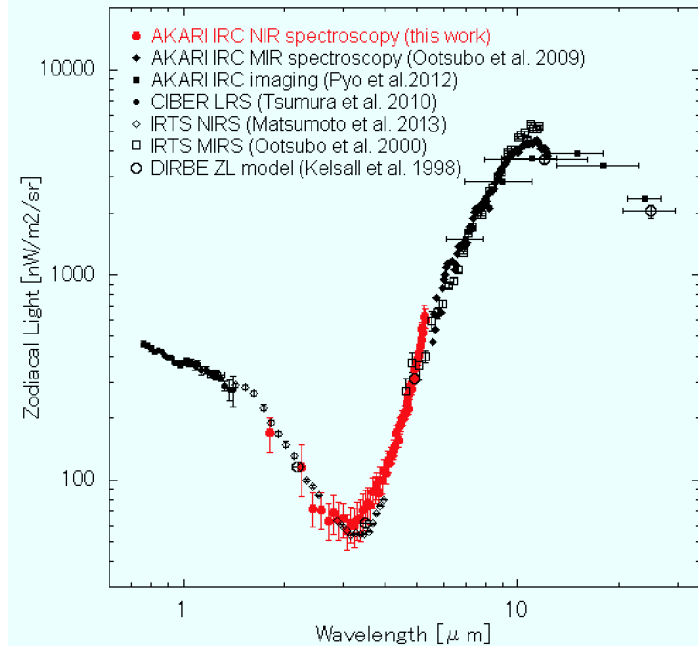
Figure 1.5 Compilation of spectral measurements of ZL from near to mid-IR (Tsumura et al. 2013a). References of the individual symbols are presented at the upper left. All results are normalized to the data from the DIRBE ZL model (Kelsall et al. 1998).

than that of DIRBE, more detailed structure of dust bands was investigated.

In addition to the study of the IPD structure, spectroscopic observations have been conducted to investigate the composition and origin of the IPD. Based on the near-IR observation by rocket-borne experiment, Matsuura et al. (1995) found the ZL color redder than the solar spectrum, indicating contribution of large IPD ($\gtrsim 1.0\,\mu$m) to the scattered light. Analyzing data taken by Near-Infrared Spectrometer (NIRS) onboard *Infrared Telescope in Space* (*IRTS*), Matsumoto et al. (1996) also reported the redder ZL spectrum.

Recently, the spectroscopic study of ZL has been conducted by *AKARI*/IRC and Low Resolution Spectrometer (LRS) onboard *Cosmic Infrared Background Experiment* (*CIBER*). The obtained ZL spectra from near to mid-IR are summarized in Figure 1.5. All studies exhibit the similar spectral shape. Particularly, Tsumura et al. (2010) reported an absorption feature at $\sim 0.9\,\mu$m by analyzing the *CIBER*/LRS data. They attributed this feature to silicate compounds such as pyroxene and/or olivine.

One major problem in the ZL study is how to supply the IPD. The IPD is expected to fall into the Sun by the Poynting-Robertson drag or leave the solar system by the radiation

pressure in a time scale of 10^3–10^7 years, much shorter than the age of the solar system (Mann et al. 2006). Therefore, the IPD particles that are responsible for the ZL should have been supplied continuously by asteroids or comets, though the contribution of each component to the IPD is unclear. To identify the IPD supplier, it is helpful to compare the reflectance spectrum of the ZL with those of asteroids and comets. Here, the reflectance means reflected fraction of light against the solar spectrum. Combining the ZL reflectance observed with *CIBER*/LRS and *IRTS*/NIRS, Tsumura et al. (2010) suggested that the spectral shape is similar to that of a S-type asteroid, such as 25143-Itokawa (Binzel et al. 2001) in ~ 0.8–$2.5\,\mu$m. In the near-IR, Yang & Ishiguro (2015) showed that the reflectance of the ZL is also similar to that of comets classified as D-type asteroids (Bus & Binzel 2002). They suggested that most of the IPD particles originate from comets (D-type asteroids) by comparing optical properties (i.e., albedo and spectral gradient) of various asteroids (Bus & Binzel 2002) with those of the ZL (Ishiguro et al. 2013). This result is consistent with a numerical simulation taking into account kinematic and dynamical processes of the IPD particles (Nesvorný et al. 2010).

1.1.2 Diffuse Galactic light

Interstellar dust plays crucial roles in various astrophysical phenomena. Presence of interstellar dust was first inferred from "extinction" of the starlight (Trumpler 1930). From the wavelength-dependence of the extinction, variety in the grain size is implied. The dust extinction includes absorption and scattering, which are strictly determined by the Mie theory for spherical grains (Mie 1908; Debye 1909). After the absorption, dust grains reemit thermal emission. Therefore, interstellar dust properties can be investigated through the observation of scattered light and the thermal emission.

The scattered component in the diffuse interstellar medium (ISM) was noticed as "optical cirrus" in late 1930s. Several studies (e.g., Elvey & Roach 1937; Henyey & Greenstein 1941; van de Hulst & de Jong 1969; Mattila 1979) revealed that the optical diffuse component is starlight scattered off by interstellar dust grains illuminated by the interstellar radiation field (ISRF). Over 50 years later, diffuse far-IR emission, so called IR cirrus, was discovered by *IRAS* (Low et al. 1984). Immediately, the IR cirrus was found to be also visible in the optical wavelength (de Vries & Le Poole 1985; Paley et al. 1991) and the IR cirrus was recognized as a counterpart of the optical cirrus. Subsequently, the correlation analysis between diffuse optical light and far-IR emission was first conducted by Beichman (1987) and Guhathakurta & Tyson (1989) to study the scattering property of interstellar dust.

Combining data obtained with *IRAS* and *COBE*/DIRBE, Schlegel et al. (1998) created
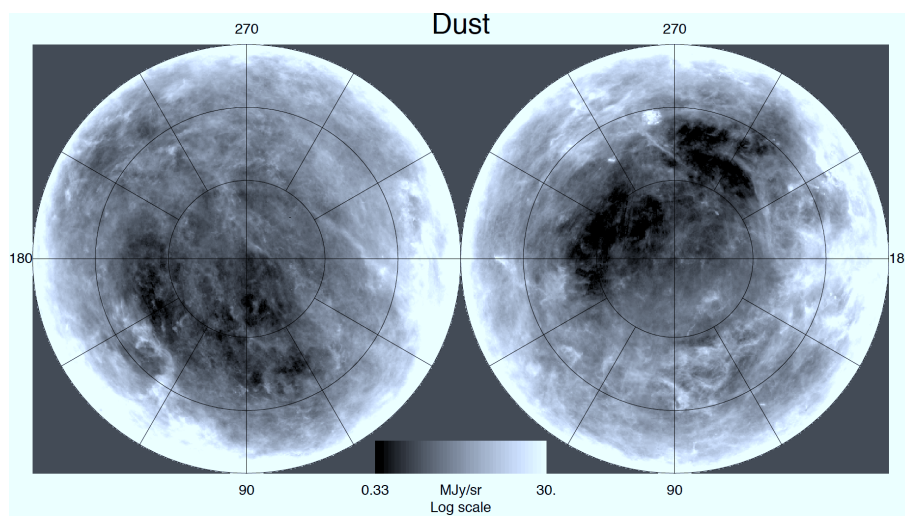
Figure 1.6 Full-sky $100\,\mu$m intensity map for the north (left) and south (right) Galactic regions in Lambert projection (Schlegel et al. 1998).
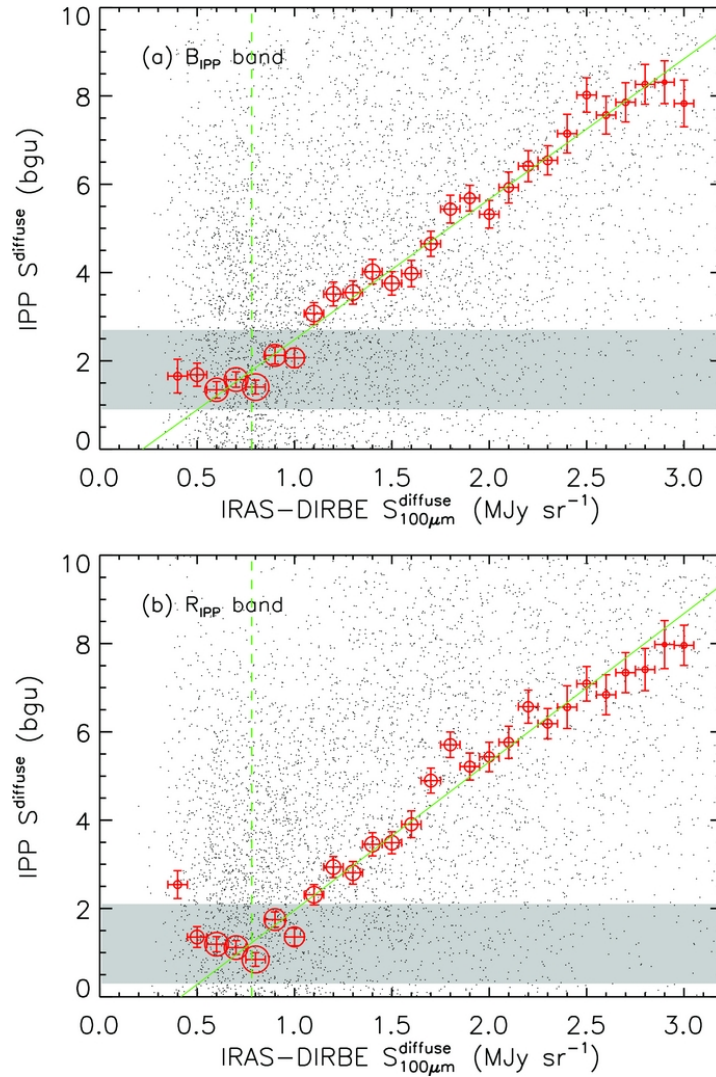
Figure 1.7 Correlation between $100\,\mu$m emission and diffuse optical light in the B (panel a) and R band (panel b) observed with *Pioneer 10/11* in high Galactic latitudes ($|b| > 35°$; Matsuoka et al. 2011). Black dots indicate the observed value. Red circles and the vertical error bars indicate the averaged values of the sample in a x-direction bin and the weighted standard errors, respectively, with the size of the circles proportional to each sample size. Green solid line denotes the best-fit line for red circles. Vertical green dashed line indicates the $100\,\mu$m EBL intensity derived from Lagache et al. (2000).

9

all-sky $100\,\mu$m emission map from which the ZL contribution is removed (hereafter "SFD" map). The $100\,\mu$m emission map is shown in Figure 1.6. Utilizing the high spatial resolution of this map (pixel scale $\sim 2'$), several studies have conducted the correlation analysis against the diffuse optical light (e.g., Matsuoka et al. 2011; Brandt & Draine 2012; Ienaka et al. 2013). Figure 1.7 shows the result of Matsuoka et al. (2011), who analyzed the Imaging Photopolarimeter (IPP) data on board $Pioneer10/11$ in high Galactic latitudes ($|b| > 35°$). The figure shows the linear correlation between the $100\,\mu$m map and scattered light observed with $Pioneer10/11$. In the UV, Murthy et al. (2010) reported the correlation by analyzing the data obtained with $Galaxy\ Evolution\ Explorer$ ($GALEX$).

The correlation between the scattered light and $100\,\mu$m emission is naturally expected in the optically thin limit. The scattered intensity I_{sca} is approximated as

$$I_{\mathrm{sca}} \approx \omega \sigma_{\mathrm{ext}} N I_{\mathrm{ISRF}}, \tag{1.2}$$

where ω, σ_{ext}, N, and I_{ISRF} denote, respectively, the albedo, extinction cross section, column density of the interstellar dust, and ISRF intensity. The $100\,\mu$m intensity I_{100} is represented by

$$I_{100} \approx (1 - \omega_{100})\sigma_{100} N B(T), \tag{1.3}$$

where ω_{100}, σ_{100}, and $B(T)$ are, respectively, the albedo, extinction cross section at $100\,\mu$m, and Planck function with dust temperature T. These equations result in

$$I_{\mathrm{sca}} \approx \frac{\omega \sigma_{\mathrm{ext}} I_{\mathrm{ISRF}}}{(1 - \omega_{100})\sigma_{100} B(T)} I_{100}. \tag{1.4}$$

According to the Mie theory (Mie 1908; Debye 1909), dust-scattered light shows anisotropy as a function of scattering angle θ, which depends on the relation between the electromagnetic wavelength (λ) and grain size (a). The scattering is forward directed in case of $\lambda \sim a$ (Mie scattering), whereas the forward and backward scattering become identical in case of $\lambda \gg a$ (Rayleigh scattering). The scattering anisotropy is characterized by scattering phase function. For interstellar scattering, Henyey & Greenstein (1941; hereafter HG41) approximated the phase function $\phi(\theta)$ in an analytical form:

$$\phi(\theta) = \frac{1}{4\pi} \frac{1 - g^2}{(1 + g^2 - 2g\cos\theta)^{3/2}}, \tag{1.5}$$

where parameter g corresponds to the first moment of the phase function, indicating the degree of forward scattering:

$$g \equiv \langle \cos\theta \rangle = \int \phi(\theta)\cos\theta\, d\Omega, \tag{1.6}$$

where Ω is solid angle. By this definition, the g-factor has the range of $-1 \le g \le 1$ and forward scattering becomes dominant as it is higher. Figure 1.8 shows the HG41 scattering
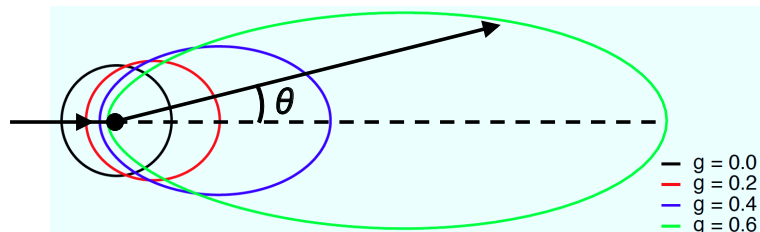
Figure 1.8 Scattering anisotropy in the HG41 phase function (Equation 1.5) with $g \equiv \langle \cos\theta \rangle = 0.0, 0.2, 0.4, 0.6$.

phase function with $g = 0.0, 0.2, 0.4, 0.6$. The g-factor has been measured by observation of scattered light in diffuse ISM, clouds, and reflection nebulae. Literature has shown that the g-factor of ~ 0.5 in the optical wavelengths (Draine 2003b: references therein). This fact indicates that the interstellar scattering is contributed by grains with $a > \lambda/2\pi \sim 0.1\,\mu$m in the optical (Draine 2011).

Considering the scattering anisotropy, the scattered intensity is expected to show Galactic latitude-dependence since Galactic stars are concentrated to the Galactic plane. Numerical calculation by Jura (1979) approximated the intensity ratio of scattered light to $100\,\mu$m emission as a function of Galactic latitude b:

$$\frac{I_{\text{sca}}}{I_{100}} \propto 1 - 1.1g\sqrt{\sin|b|}. \tag{1.7}$$

In this calculation, Jura (1979) adopted the HG41 phase function and assumed uniform illuminating sources located at the Galactic plane. Though the g-factor can be constrained from the b-dependence of the scattered light, such relation has not been observed so far.

In addition to the scattered light in the diffuse ISM, IR observation by *IRAS* and *COBE*/DIRBE confirmed the presence of thermal emission in the diffuse ISM from near to mid-IR wavelengths (Low et al. 1984; Arendt et al. 1998). Interstellar dust grains in thermal equilibrium with temperature $\sim 20\,$K create the radiation with the Planck function peaked in far-IR and such particles should not contribute to the near to mid-IR emis-

sion. Therefore, the observed emission is supposedly attributed to the very small grains ($a \lesssim 0.005\,\mu\mathrm{m}$) which are not in thermal equilibrium but are stochastically heated by ISRF. The *IRAS* data also showed the excess against continuous emission at $12\,\mu\mathrm{m}$, indicating the presence of spectral line feature in that wavelength. Such a feature was also found by the spectroscopic observation by *IRTS* toward low Galactic latitudes ($|b| < 5°$; Tanaka et al. 1996; Onaka et al. 1996). One candidate of the feature is large molecules, polycyclic aromatic hydrocarbon (PAH: Leger & Puget 1984). The PAH vibrational modes explain the 3.3, 6.2, 7.7, 8.6, and $11.3\,\mu\mathrm{m}$ features observed in HII regions and planetary nebulae.

The DIRBE observation found that the IR emission at 12, 25, 60, 140, and $240\,\mu\mathrm{m}$ linearly correlates with that at $100\,\mu\mathrm{m}$ in the diffuse ISM (Arendt et al. 1998). This indicates that the various size of interstellar dust grains and PAH are well mixed in the diffuse ISM. Arendt et al. (1998) also reported linear correlation between HI gas column density and $100\,\mu\mathrm{m}$ dust emission. This finding confirmed the mixture of gas and dust in the diffuse ISM.

To reproduce the observed properties of interstellar dust (i.e., extinction curve; albedo; g-factor; IR emission), various dust models have been developed. Mathis et al. (1977) proposed the silicate-graphite model in which the size distribution follows the power-law $dn/da \propto a^{-3.5}$, so called "MRN" model. After recognition of importance of PAH, the MRN model has been extended to silicate-graphite-PAH model (Siebenmorgen & Krügel 1992; Li & Draine 2001; Weingartner & Draine 2001, hereafter WD01). Figure 1.9 shows the size distribution of the WD01 model. The abundance of the very small grains and PAH changes the shape of the size distribution in the small-grain range ($a \lesssim 0.01\,\mu\mathrm{m}$). Other dust models include the silicate core carbonaceous mantle model (Désert et al. 1990; Jones et al. 1990; Li & Greenberg 1997) and the composite model assuming the dust to be aggregates of silicate and carbonaceous particles (Mathis & Whiffen 1989; Mathis 1996; Zubko et al. 2004). The WD01 model reportedly reproduces the observed extinction curve (e.g., Fitzpatrick 1999) from UV to near-IR (Draine 2011).

Based on these models, spectra of the dust emission have been expected. Such studies include Dwek et al. (1997), Li & Draine (2001), Draine & Li (2007; hereafter DL07), Compiégne et al. (2011). In the calculation of the emission spectra, ISRF intensity needs to be assumed. The ISRF model created by Mathis et al. (1983; hereafter MMP83) has been widely used. In $\lambda > 0.246\,\mu\mathrm{m}$, MMP83 approximated the local ISRF intensity (10 kpc from the Galactic center) as a sum of three dilute Planck function with $T = 3000$, 4000, and 7000 K, with the dilution factors 5×10^{-13}, 1.65×10^{-13}, and 10^{-14}, respectively. In
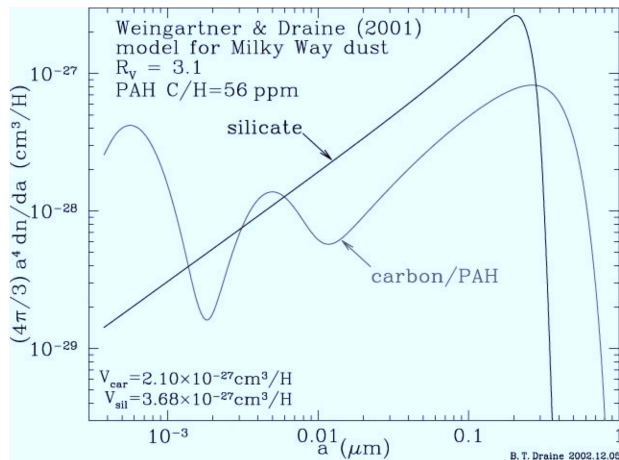
Figure 1.9 Size distribution of carbonaceous-silicate-PAH grains in the WD01 model for $R_V = 3.1$ dust (Draine 2003a). The grain abundances are reduced by factor 0.93 from the original WD01.
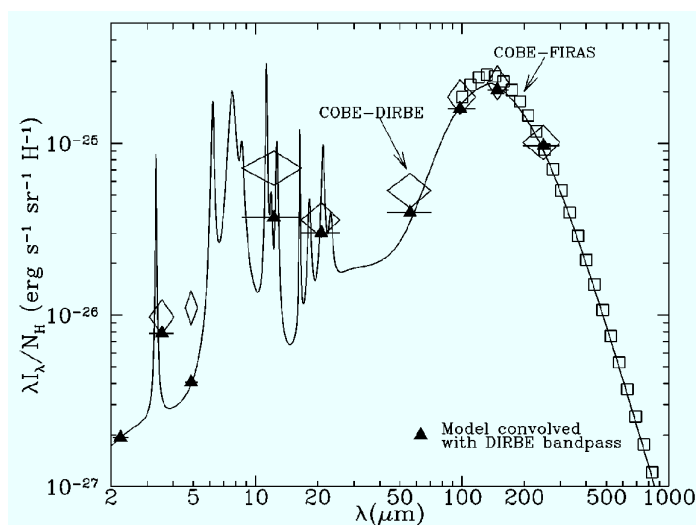
Figure 1.10 Spectra of IR dust emission normalized by hydrogen column density (Draine 2003a). Solid curve indicates model spectrum of Li & Draine (2001). Observed results from *COBE*/DIRBE (Arendt et al. 1998) and *COBE*/FIRAS (Finkbeiner et al. 1999) are indicated by diamonds and squares, respectively. Filled triangles represent the model values convolved with DIRBE bands.

$0.0912 \, \mu\mathrm{m} < \lambda < 0.246 \, \mu\mathrm{m}$, the ISRF is presented by three power-low segments:

$$
\begin{cases}
2.373 \times 10^{-14} (\lambda/\mu\mathrm{m})^{-0.6678} \, \mathrm{erg \, cm^{-3}} \ (0.134 - 0.246 \, \mu\mathrm{m}) \\
6.825 \times 10^{-13} (\lambda/\mu\mathrm{m}) \, \mathrm{erg \, cm^{-3}} \ (0.110 - 0.134 \, \mu\mathrm{m}) \\
1.287 \times 10^{-9} (\lambda/\mu\mathrm{m})^{4.4172} \, \mathrm{erg \, cm^{-3}} \ (0.0912 - 0.110 \, \mu\mathrm{m})
\end{cases}
\tag{1.8}
$$

Figure 1.10 shows the DL07 dust emission model estimated from the WD01 dust model with MMP83 ISRF. The model is marginally consistent with the observation (*COBE*/DIRBE; Arendt et al. 1998, *COBE*/FIRAS; Finkbeiner et al. 1999).

In the near-IR, the DGL observation has been controversial due to its faintness by the low optical depth. However, it is important to measure the near-IR DGL for understanding the properties of interstellar dust in diffuse ISM, because the scattered light and thermal emission components are expected to coexist in the wavelengths. In particular, the strong PAH feature at $3.3 \, \mu\mathrm{m}$ is useful to determine the mass fraction of the very small grains and PAH. In the study of the scattered light, Brandt & Draine (2012) developed model spectra of the scattered light by adopting the interstellar dust models and ISRF. According to their prediction, a dust model including larger grains shows redder spectra than that with smaller grains, particularly in the near-IR. Therefore, the near-IR scattered light provides information on size distribution of the interstellar dust, which is crucial in understanding the interstellar dust properties.

1.1.3 Extragalactic background light

Penzias & Wilson (1965) found the EBL in the radio wave, known as cosmic microwave background (CMB). In 1989, the *COBE* satellite was launched to investigate the spectrum and the anisotropy of the CMB with Far-infrared absolute spectrophotometer (FIRAS) and Differential microwave radiometer (DMR), respectively. As a result, the CMB spectrum was found to be fitted to the $2.7 \, \mathrm{K}$ black-body radiation (Mather et al. 1990) and the CMB fluctuation was found to be an order of $\sim 10^{-5}$ throughout the sky (Smoot et al. 1992). Thanks to these studies, the CMB is now thought to be the afterglow light of the big bang.

By measuring the redshift-luminosity relation of Ia supernovae, the universe expansion has been found to be accelerated in the present epoch (Riess et al. 1998; Schmidt et al. 1998; Perlmutter et al. 1999). The accelerating energy is now called dark energy. After *COBE*, *WilkinsonMicrowaveAnisotropyProbe* (*WMAP*) and *Planck* have measured the CMB fluctuation more precisely and determined the cosmological parameters. Such measurements have revealed that the dark energy is dominant component in the current universe, compared to the baryon and dark matter. Figure 1.11 illustrates the cosmic history in the current cosmology.

14
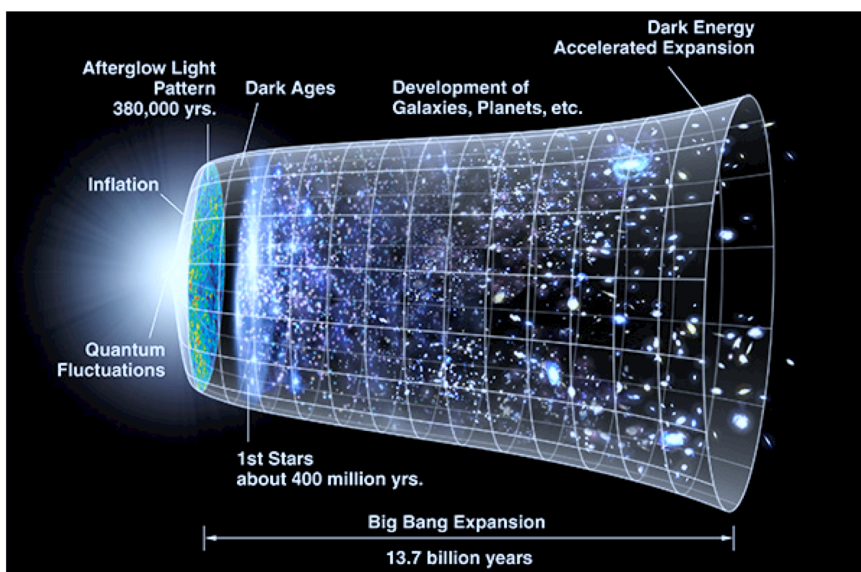
Figure 1.11 Cosmic history in the modern cosmology (image credit: NASA/WMAP Science team).

In the UV to IR wavelengths, the EBL is thought to contain entire radiation emitted throughout the epoch of galaxy formation. Such radiation originates from evolved galaxies, protogalaxies, intergalactic matter, and possible exotic processes (e.g., Bond, Carr, & Hogan 1986). Theoretically, the EBL intensity at redshift z_0 and wavelength λ_0 is calculated as the redshift (z) integration of the comoving specific luminosity density $L_\nu(\lambda, z)$ with the cosmological parameters (e.g., Dwek & Krennrich 2013):

$$I_{\nu,\mathrm{EBL}}(\lambda_0, z_0) = \frac{c}{4\pi} \int_{z_0}^{\infty} L_\nu(\lambda, z) \left| \frac{dt}{dz} \right| dz \qquad (1.9)$$

$$= \frac{c}{4\pi} \int_{z_0}^{\infty} \frac{L_\nu(\lambda, z)}{H_0(1+z)[\Omega_m(1+z)^3 + \Omega_\Lambda]^{1/2}} dz, \qquad (1.10)$$

where c, H_0, Ω_m, and Ω_Λ are, respectively, the speed of light, Hubble constant, dimensionless parameters of matter, and cosmological constant Λ. In the current cosmology for flat universe, these parameters are $H_0 = 70\,\mathrm{km\,s^{-1}\,Mpc^{-1}}$, $\Omega_m = 0.27$, $\Omega_\Lambda = 0.73$ (e.g., Hinshaw et al. 2009). The quantity $L_\nu(\lambda, z)$ reflects the star formation rate at z, an indicator of the star formation history. Therefore, the EBL measurement is crucial in constraining the star formation history and the cosmological parameters. The EBL from UV to near-IR is an indicator of direct stellar component, while that in the far-IR serves as a tracer of dust-obscured star formation.

Figure 1.12 compiles current measurements of UV to far-IR EBL. The lower limit of the EBL is given by integrated light of the individual galaxies. Thanks to recent deep galaxy counts, the integrated galaxy light (IGL) has been measured with small uncertainties from UV to far-IR (e.g., Madau & Pozzetti 2000; Totani et al. 2001; Gardner et al. 2000; Fazio et al. 2004; Elbaz et al. 2002; Driver et al. 2016).

In the direct measurement of the EBL, foreground emissions described in the prior sections must be removed from the sky brightness and the residual isotropic light is thought to include the EBL. Due to the intense ZL foreground, the measurements of the residual light have not been successful in the mid-IR. In the far-IR, most results are marginally converged to the same intensity as the IGL (e.g., Lagache et al. 2000; Matsuura et al. 2011). This indicates that the IGL is a dominant component in the EBL and contribution of other unknown emissions is small in the far-IR.

In contrast to the situation in the longer wavelengths, the optical to near-IR measurements have been more controversial. In these wavelengths, the measurements have been conducted by *HST* (Bernstein et al. 2002; Bernstein 2007), *COBE*/DIRBE (e.g., Hauser et al. 1998; Hauser & Dwek 2001; Gorjian et al. 2000; Cambrésy et al. 2001; Levenson et al. 2007; Levenson & Wright 2008), *IRTS* (Matsumoto et al. 2005; Matsumoto et al. 2015), and *AKARI* (Tsumura et al. 2013c). Some authors have reported that the intensity of the
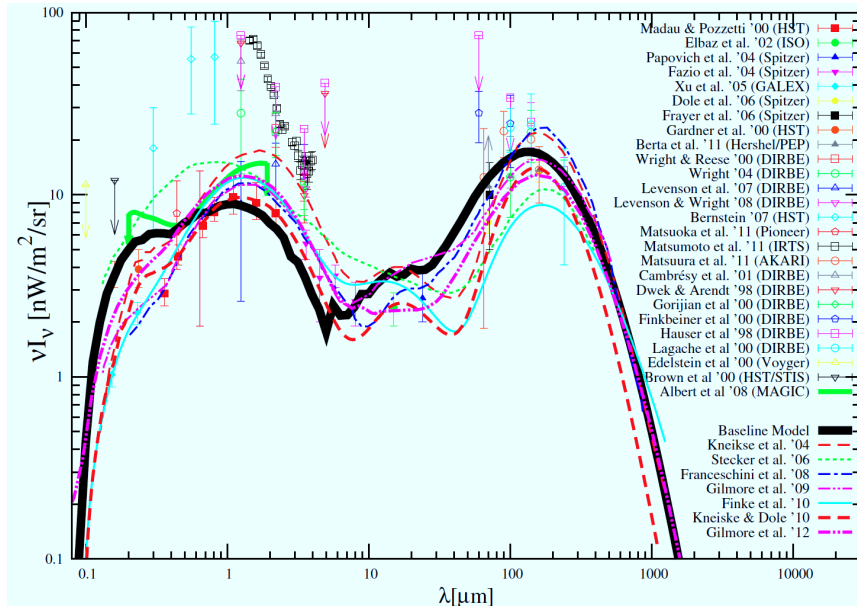
Figure 1.12 Current measurements of EBL intensity from UV to far-IR (Inoue et al. 2013). References of the individual results are shown in the right. Diffuse measurements come from Wright & Reese (2000), Wright (2004), Levenson et al. (2007), Levenson & Wright (2008), Bernstein (2007), Matsuoka et al. (2011), Matsumoto et al. (2011), Matsuura et al. (2011), Cambrésy et al. (2001), Dwek & Arendt (1998), Gorjian et al. (2000), Finkbeiner et al. (2000), Hauser et al. (1998), Lagache et al. (2000), Edelstein et al. (2000), and Brown et al. (2000). IGL observations are from Madau & Pozzetti (2000), Elbaz et al. (2002), Papovich et al. (2004), Fazio et al. (2004), Xu et al. (2005), Dole et al. (2006), Frayer et al. (2006), Gardner et al. (2000), and Berta et al. (2011). IGL models are from Kneiske et al. (2004), Stecker et al. (2006), Franceschini et al. (2008), Gilmore et al. (2009), Finke et al. (2010), Kneiske & Dole (2010), and Gilmore et al. (2012). EBL constraint from γ-ray observation is derived from Albert et al. (2008).

17
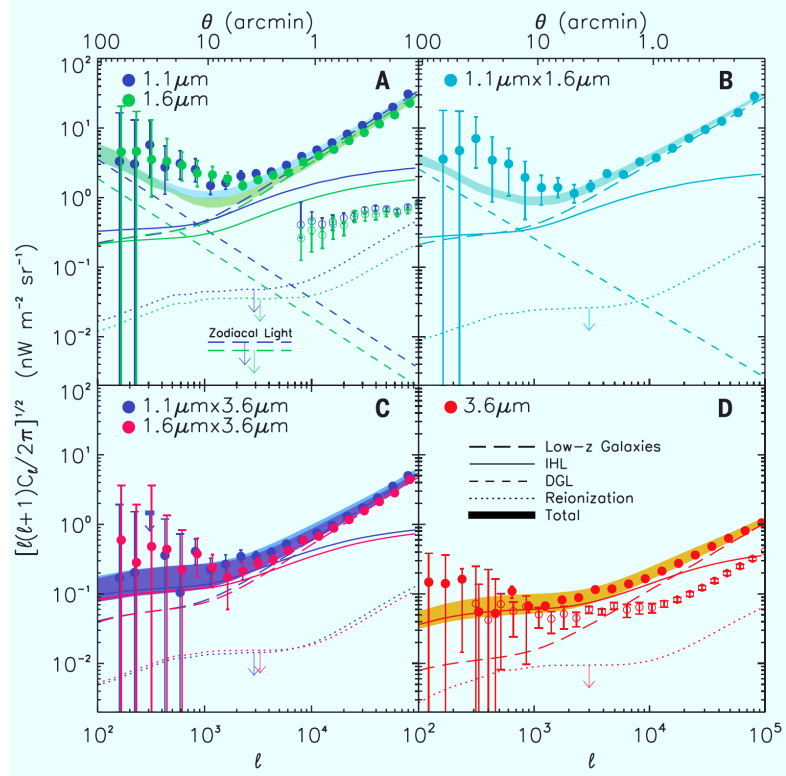
Figure 1.13 Auto- and cross- power spectra of the diffuse near-IR radiation observed with *CIBER* (1.1 and 1.6 μm) and *Spitzer* (3.6 μm) (Zemcov et al. 2014). Filled circles in panels (A), (B), (C), and (D) indicate, respectively, the auto-spectra (1.1 μm and 1.6 μm), cross-spectra (1.1 μm with 1.6 μm), cross-spectra (1.1 μm with 3.6 μm and 1.6 μm with 1.6 μm, and auto spectra (3.6 μm). In each panel, expected contributions from low-z galaxies, IHL, DGL, $z > 7$ first galaxies, and the total of these components are represented by curves indicated in the upper part of Panel (D).

residual light is several times higher than the IGL intensity, which may be attributed to the exotic extragalactic sources. To explain the near-IR excess light peaked at $\sim 1.6\,\mu$m Matsumoto et al. (2005) suggested the contribution of primordial Population-III (Pop-III) stars, based on prediction from Salvaterra & Ferrara (2003). However, Dwek et al. (2005a) showed some difficulties in creating the excess light by primordial stars. For one thing, to produce such strong radiation, the Pop-III star formation rate is required to be 4–10 times the nominal prediction. For another thing, about 10% of the baryon must be converted to the creation of the Pop III stars. After that, theoretical predictions have shown that the Pop-III contribution to the EBL is only less than 1% of the IGL intensity (e.g., Inoue et al. 2013)

In the optical wavelengths, Matsuoka et al. (2011) analyzed the IPP data on board *Pioneer10/11*, the probers of Jupiter and Saturn. The data were taken beyond ~ 3 AU from the Sun, where the ZL contribution is below the detection limit of the instrument (Hanner et al. 1974). They reported low-level isotropic light, which is consistent with the IGL intensity (Figure 1.12).

Other constraints on the EBL intensity have been given by observations of high-energy γ-ray from blazars. By interaction between γ-rays and the EBL photons in the intergalactic space, pairs of electron and positron are created, so called "pair production". The EBL intensity is then estimated by comparing the observed spectra of blazars with the assumed intrinsic spectra. Though there is an uncertainty in the assumption of the intrinsic spectra of blazars, most studies have derived low-level EBL intensity close to the IGL, indicating a small amount of the EBL component other than IGL. (e.g., Guy et al. 2000; Dwek & Krennrich 2005; Schroedter 2005; Aharonian et al. 2006; Albert et al. 2008; Mazin & Raue 2007; Orr et al. 2011; Meyer et al. 2012; Abramowski et al. 2013). If the entire excess light observed with *IRTS* originates from the reionization epoch ($z \gtrsim 6$), intrinsic spectra of blazer are expected to show physically unnatural shape (Dwek et al. 2005b). In terms of the EBL constraints from the γ-ray observations, the excess light is thought to originate from the local universe.

In the measurements of EBL intensity from the Earth orbit, methods for subtracting the ZL component have been controversial. Though the DIRBE ZL model (Kelsall et al. 1998) has been widely used for the ZL subtraction, Wright (1998)-based model, hereafter called as "Wright model" has been available as well. In the Wright model, an isotropic light component is arbitrarily added to the ZL model under "no zodi principle". The Wright model thus yields the residual isotropic light lower than the DIRBE ZL model does. However, such an isotropic component has not been observationally confirmed and the intensity is unknown even if it exists. From the physical viewpoint, the DIRBE ZL model

may be preferable since the model is determined by the IPD physical parameters, without adding the isotropic component.

To measure the EBL intensity by eliminating the uncertainty associated with the ZL model, "dark cloud method" was suggested by Mattila in 1970s. This method utilizes the shielding effect of a dark cloud with large optical depth. If the EBL is completely shielded by the dark cloud, the intensity difference between the cloud and surrounding regions corresponds to the EBL intensity. In principle, the ZL component is canceled out by taking the difference. Similarly, Tsumura et al. (2014) utilized eclipse of Jovian satellite to measure the EBL. However, these techniques have not been successful in detecting the EBL due to the difficulty in the evaluation of other diffuse emissions, such as DGL or atmospheric light of Jupiter.

Complementary to the intensity measurements of the EBL, several studies have analyzed the angular power spectrum of diffuse near-IR light, whose advantage is free from the uncertainty of the foreground subtraction (e.g., Cooray et al. 2007; 2012a; Kashlinsky et al. 2005; 2012; Thompson et al. 2007; Matsumoto et al. 2011; Zemcov et al. 2014). Some authors have reported excess power in a few arcsec-scale, which cannot be explained by faint galaxies or other known components, such as ZL and DGL. Figure 1.13 illustrates an example of the fluctuation analysis in the near-IR (Zemcov et al. 2014). They attributed the excess origin to intra halo light (IHL), which are created by tidally stripped stars from their parent galaxies by mergers or collisions (Cooray et al. 2012b). On the other hand, Yue et al. (2013) raised possibility of accretion of direct collapse black hole (DCBH) in the early universe ($z \gtrsim 10$). These hypothetical sources may contribute to not only the power spectrum but also the EBL intensity. However, these components are not expected to create the high EBL intensity in the near-IR.

1.2　Problems in the near-infrared measurement

Figure 1.14 illustrates the diffuse near-IR emissions in the solar system, Milky Way, and extragalactic field. Regardless of the scientific importance of the diffuse near-IR emissions, particularly the DGL and EBL, measurements of these components have been controversial since the epoch of *COBE*/DIRBE observation. In the near-IR, *COBE*/DIRBE created all-sky maps which were appropriate for analyzing the diffuse emissions (Figure 1.3). Thanks to the DIRBE ZL model based on the physical properties of IPD, the ZL evaluation was rather successful (Kelsall et al. 1998). Since the ISL also largely contributes to the near-IR sky brightness and the DIRBE beam is too large to mask individual stars ($\sim 0.7° \times 0.7°$), the ISL intensity must be evaluated precisely to analyze the other emission components, i.e., DGL
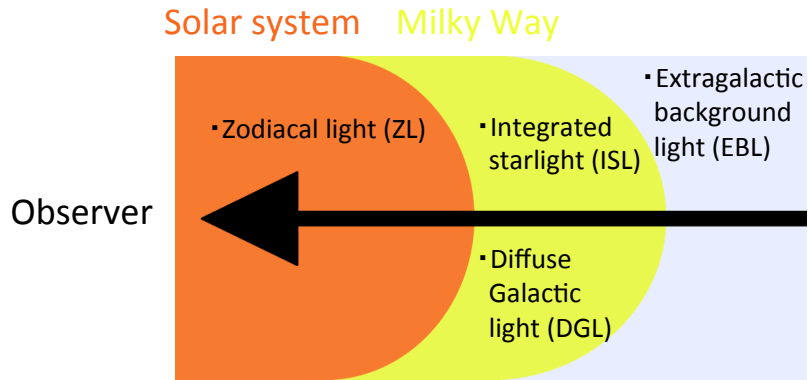
Figure 1.14 Near-IR emission components observed from the Earth.
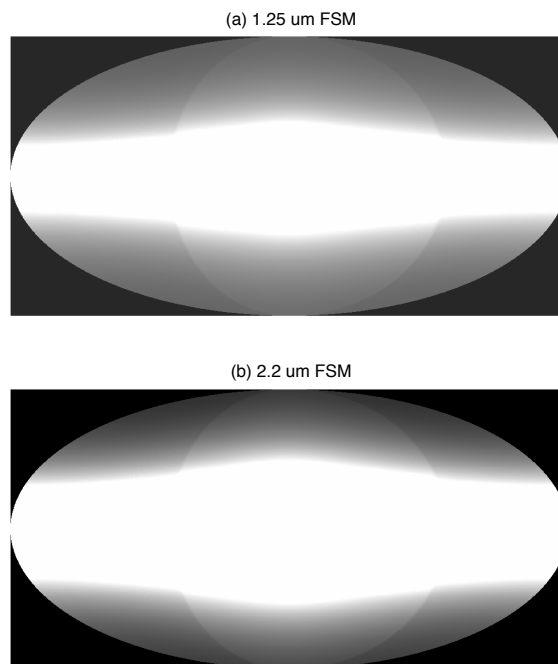
Figure 1.15 FSM intensity maps at $1.25\,\mu$m (upper panel) and $2.2\,\mu$m (lower panel) in Galactic Mollweide projection with the Galactic center in the middle.

Table 1.1 IR intensity ratios derived in the previous DIRBE analysis (Arendt et al. 1998)

Band (μm)	I_ν/I_{100}	Analyzed Region
1.25	—	—
2.2	—	—
3.5	0.00183 ± 0.00001	$|b| < 30°, |\beta| > 40°, 54° < l < 138°, 234° < l < 318°$
4.9	0.00291 ± 0.00003	$|b| < 30°, |\beta| > 40°, 54° < l < 138°, 234° < l < 318°$
12	0.0462 ± 0.0001	$b > 10°, \beta > 70°$
25	0.0480 ± 0.0002	$b > 10°, \beta > 70°$
60	0.171 ± 0.0003	$|b| > 30°, |\beta| > 40°$
100	1.00	—
140	1.696 ± 0.008	$|b| > 45°$
240	1.297 ± 0.005	$|b| > 45°$

and EBL. In the initial DIRBE analysis, however, the ISL intensity was estimated from not actual photometric flux of stars but star-counts model assuming the star formation rate and interstellar extinction of the Milky Way (Wainscoat et al. 1992; Cohen 1993, 1994, 1995). The star-counts model optimized for the DIRBE analysis is called "DIRBE faint source model (FSM)". Figure 1.15 shows the FSM maps used in the previous DIRBE analysis (Arendt et al. 1998).

Due to the large uncertainty in the FSM, Arendt et al. (1998) failed to extract the DGL components at 1.25 and 2.2 μm. In other words, they did not find the correlation between 100 μm dust emission and the diffuse light observed with DIRBE, as shown in Table 1.1. Therefore, the DGL contribution to the sky brightness was uncertain, and studies after the DIRBE analysis have ignored the DGL components at 1.25 and 2.2 μm. In contrast to the conclusion of Arendt et al. (1998), Leinert et al. (1998) suggested that the Galactic component observed by the DIRBE in the near-IR bands undoubtedly contains a scattered light contribution. As a supportive evidence for this prediction, Arai et al. (2015) recently derived spectrum of intensity ratios of the DGL to 100 μm emission at 0.95–1.65 μm from the *CIBER*/LRS data. However, their results were obtained in the limited fields, i.e., six small regions in the sky. It is then questionable whether the near-IR DGL ubiquitously exists in the diffuse ISM and the intensity ratio of the DGL to 100 μm emission can be applicable to the entire high-latitude sky.

In the longer near-IR wavelengths at 3.5 and 4.9 μm, Arendt et al. (1998) extracted the DGL component from the DIRBE data in low Galactic ($|b| < 30°$) and high ecliptic latitudes ($|\beta| > 40°$) to enhance the interstellar dust emission and avoid the strong ZL emission (Table 1.1). Because of its low precision in the ISL evaluation same as 1.25 and 2.2 μm, their results were derived not by direct correlation against 100 μm emission but by

the color-color method, which makes use of the color difference between the ISL and DGL. More critically, they assumed that the DGL results in the low Galactic latitudes, including the region close to the Galactic plane, are the same as that in the high-latitude region where is appropriate for the EBL measurements. Naturally, it is questionable whether the DGL results at low latitudes are applicable to those at high latitudes because the ISRF intensity and/or the dust properties could be different between these regions. After that, the DGL results at low latitudes have been used as the high-latitudes DGL contribution in the EBL measurements (Dwek & Arendt 1998; Gorjian et al. 2000). In the high Galactic latitudes ($|b| > 30°$), Tsumura et al. (2013b) and Matsumoto et al. (2015) reported no detection of DGL in their analysis of the diffuse sky spectrum obtained with *AKARI* and *IRTS*, probably because of the low signal-to-noise ratio in their analyses of limited regions of the sky.

The poor ISL evaluation in the initial DIRBE analysis affected not only the DGL values but also the EBL measurements. As a result, Hauser et al. (1998) reported only upper limit of the near-IR residual light. In addition, Mattila (2006) predicted that the near-IR DGL has significant contribution to the sky brightness. Therefore, the large residual light observed with *IRTS* (Matsumoto et al. 2005) may become smaller if the DGL component is accurately evaluated. To determine the DGL and residual isotropic light in the near-IR, ISL evaluation must be improved.

As indicated from Equation (1.7), Galactic latitude dependence of the scattered light component of the DGL is useful in constraining the g-factor that reflects the grain size of the interstellar dust. By surface brightness observations of a globule, for example, Lehtinen & Mattila (1996) derived the near-IR grain albedo, but no study has determined the near-IR g-factor. In the near-IR, isotropic scattering due to the Rayleigh scattering is expected to be dominant since the wavelength would be much larger than the typical grain size in the recent dust models, such as WD01. Therefore, the near-IR g-factor estimated from Galactic latitude dependence of the scattered light is also helpful in constraining the interstellar dust model.

1.3 Strategy of the improved analysis

As described in the previous section, the ISL evaluation must be improved to confirm the diffuse near-IR emission components. For the diffuse sky-brightness data, DIRBE is the most appropriate to investigate the high-latitude DGL component since they provide all-sky maps of higher signal-to-noise ratio thanks to the wide-band photometry. The all-sky data are also needed to measure Galactic latitude dependence of the scattered light component

23

of the DGL.

After 2000s, Two Micron All-Sky Survey (2MASS) project conducted all-sky survey in the $J(\sim 1.25)$, $H(\sim 1.6)$, and $K_s(\sim 2.2\,\mu\text{m})$ bands using ground-based telescopes (Cutri et al. 2003). Consequently, all-sky Point Source Catalog (PSC) was created with the completeness limit of 15.8 mag at J band (Skrutskie et al. 2006). Since then, the PSC has been used to estimate the ISL contribution at these bands in the EBL measurements (e.g., Gorjian et al. 2000, Cambrésy et al. 2001), though the DGL contribution has been ignored. In the longer near-IR wavelengths, *Wide-field Infrared Survey Explorer* (*WISE*) conducted the all-sky survey at 3.4, 4.6, 12, 22 μm (Wright et al. 2010). The latest "AllWISE" catalog achieved the detection limit of 17.1 mag at $3.4\,\mu$m, comparable to the 2MASS sensitivity. This catalog is also useful in calculating the near-IR ISL intensity.

1.4   Outline of this thesis

Figure 1.16 illustrates the conceptual scheme of this thesis. By improving the ISL evaluation using the 2MASS and *WISE* source catalogs, the present study succeeds in determining the contribution of each diffuse emission component in the near-IR. In particular, the near-IR DGL measurement provides wealthy information on the interstellar dust in the diffuse ISM. In addition, intensity of the residual isotropic light is first determined with the evaluation of the DGL components.

The remainder of this thesis is organized as follows. Chapter 2 describes the DIRBE observation and characteristics of all-sky maps used in the present study. In Chapter 3, the near-IR ISL maps are created using 2MASS and AllWISE catalogs. After that, the DIRBE brightness is decomposed to the ZL, DGL, ISL, and diffuse isotropic light. Each component is compared with earlier observations. In Chapter 4, interstellar dust properties in the diffuse ISM are investigated by comparing the observed near-IR DGL with models of scattered light and thermal emission. From the observed Galactic latitude dependence of the DGL, scattering anisotropy by dust grains is constrained. In Chapter 5, origin of the near-IR isotropic light is discussed in comparison with EBL models and constraints from the γ-ray observation. As one interpretation of the isotropic light, hypothetical IPD is first quantitatively evaluated. Summary of this thesis appears in Chapter 6.

In this thesis, the sky brightness is expressed in units of $\text{nW}\,\text{m}^{-2}\,\text{sr}^{-1}$, $\text{MJy}\,\text{sr}^{-1}$, or $\text{erg}\,\text{s}^{-1}\,\text{cm}^{-2}\,\text{sr}^{-1}$. The conversion formula between these units are

$$\nu I_\nu\,(\text{nW}\,\text{m}^{-2}\,\text{sr}^{-1}) = [3000/\lambda\,(\mu\text{m})]\,I_\nu\,(\text{MJy}\,\text{sr}^{-1}), \tag{1.11}$$

$$\nu I_\nu\,(\text{nW}\,\text{m}^{-2}\,\text{sr}^{-1}) = 10^{-6} \times \nu I_\nu\,(\text{erg}\,\text{s}^{-1}\,\text{cm}^{-2}\,\text{sr}^{-1}). \tag{1.12}$$
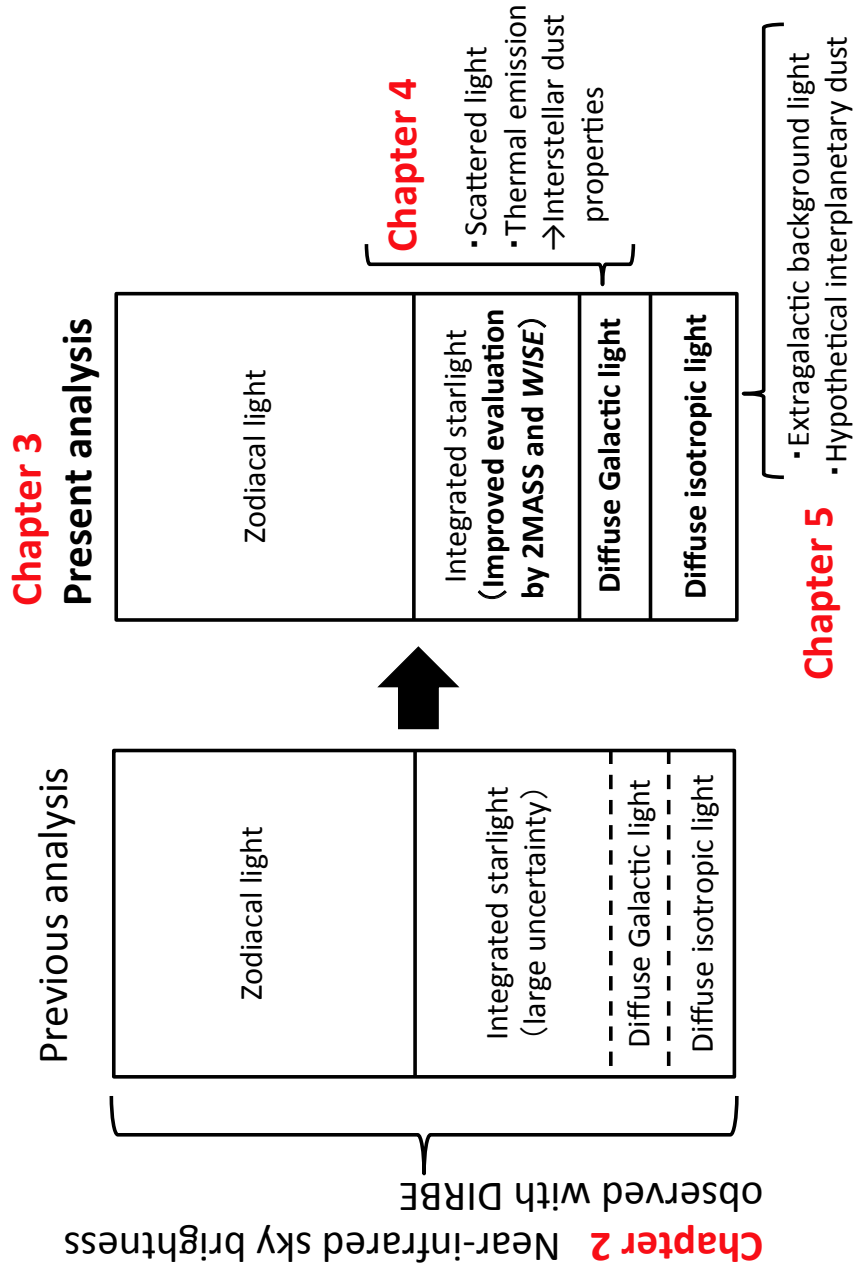
Figure 1.16 Conceptual scheme of this thesis.

Chapter 2

Data: DIRBE All-Sky Map

2.1 Overview of DIRBE mission

DIRBE was one of the instruments onboard the *COBE* spacecraft and was designed to investigate the near to far-IR EBL. The observational approach was to make absolute brightness maps of full sky in 10 photometric bands, 1.25, 2.2, 3.5, 4.9, 12, 25, 60, 100, 160, and 240 μm. Its cryogenic operation was implemented from 1989 November 24 to 1990 September 21. During these 10 months, full sky was observed with solar elongation angle ranging from 64° to 124°. This section gives an overview of the DIRBE instrument and the observation.

2.1.1 DIRBE instrument

Characteristics of the DIRBE instrument including telescope, detector, and filter are summarized in Table 2.1 and 2.2. The DIRBE optical configuration was carefully designed to reject stray light from the Sun, Earth limb, Moon, or other off-axis celestial radiation, as well as radiation from the other *COBE* instruments (Magner 1987). Figure 2.2 shows optics diagram of DIRBE (COBE/DIRBE Explanatory Supplement 1998). At any wavelengths, the stray light contamination in a single field of view do not exceed $1\,\mathrm{nW\,m^{-2}\,sr^{-1}}$.

The instrument was maintained at a temperature below $2\,\mathrm{K}$ within the superfluid helium dewar. Absolute brightness was measured by chopping between the sky signal and a zero-flux internal reference at $32\,\mathrm{Hz}$. Instrumental offsets were measured about 5 times per orbit by closing shutter located at the prime focus. The final uncertainties in the instrumental offset are quite negligible at wavelengths shorter than $140\,\mu$m (Hauser et al. 1998).

Stability and linearity of the instrument response were measured by internal radiative references that stimulated all detectors when the shutter was closed. Highly redundant sky
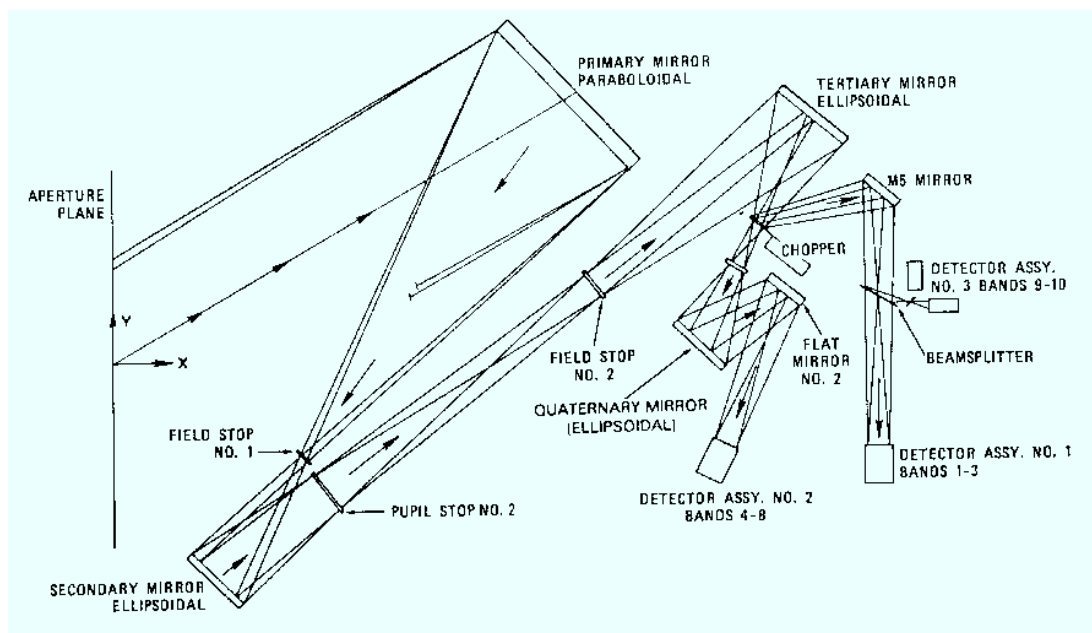
Figure 2.1 Optics diagram of DIRBE (COBE/DIRBE explanatory supplement 1998). The full beam shutter (not shown) was located at field stop 1. The cold beam stop (not shown), viewed by all detectors when not exposed to the sky, was located to the left of the chopper blades in this fiure.

Table 2.1 Instrument characteristics (COBE/DIRBE Explanatory Supplement 1998)

Telescope diameter (primary)	19 cm
Telescope type	Cryogenic off-axis folded Gregorian
Telescope effective focal length	14.24 cm
Instantaneous field of view	$0.7° \times 0.7°$
Instrument type	absolute photometer and polarimeter
Photometric bands (μm)	1.25, 2.2, 3.5, 4.9, 12, 25, 60, 100, 140, 240
Polarimetric bands (μm)	1.25, 2.2, 3.5

Table 2.2 Detector and filter characteristics (Hauser et al. 1998)

Band	λ (μm)	Detector type	Filter Construction[a]
1	1.25	InSb[b]	Coated Glass
2	2.2	InSb[b]	Coated Glass
3	3.5	InSb[b]	Coated Germanium
4	4.9	InSb[b]	MLIF/Germanium
5	12	Si:Ga BIB	MLIF/Germanium/ZnSe
6	25	Si:Ga BIB	MLIF/Silicon
7	60	Ge:Ga	MLIF/Sapphire/KRS5/Crystal Quarts
8	100	Ge:Ga	MLIF/KCI/CaF$_2$/Sapphire
9	140	Si/diamond bolometer	Sapphire/MeshGrids/BaF$_2$/KBr
10	240	Si/diamond bolometer	Sapphire/Grids/BaF$_2$/CsI/AgCl

[a] MLIF = multilayer interference filter.

[b] Antireflection coated for the band center wavelength.

sampling allowed the stable celestial sources to provide photometric closure throughout the sky. Consequently, it accomplished reproducible photometry to better than $\sim 1\%$ (Hauser et al. 1998).

2.1.2 All-sky observation

A 900 km altitude was chosen for *COBE*. In observation from the Earth orbit, the diffuse IR brightness varies as a result of our motion within IPD. Therefore, the DIRBE was designed to scan half the sky every day, providing the brightness variation of every pixel over the 10-month mission. This sampling is necessary to discriminate the ZL component. The scanning was conducted by tilting the DIRBE line of sight by 30° from the *COBE* axis fixed at a solar elongation angle 94°. This provides the sampling at a solar elongation angle ranging from 64° to 124°. Sky coverage within each period during the mission is shown in Figure 2.2.

Table 2.3 lists the 1σ sensitivity achieved for each $0.7° \times 0.7°$ field of view in the 10-months cryogenic operation in the near-IR bands. These values are well below the total

Table 2.3 Characteristics of near-IR DIRBE maps (Hauser et al. 1998)

Band	1	2	3	4
Nominal wavelength (μm)	1.25	2.2	3.5	4.9
Effective band width (μm)	0.31	0.36	0.90	0.66
Sensitivity ($\mathrm{nW\,m^{-2}\,sr^{-1}}$)	2.4	1.6	0.9	0.8
Calibration source	Sirius	Sirius	Sirius	Sirius
Pixel size (CSC projection)	$0.32° \times 0.32°$	$0.32° \times 0.32°$	$0.32° \times 0.32°$	$0.32° \times 0.32°$
Number of total pixels	393216	393216	393216	393216
Gain calibration uncertainty (%)	3.1	3.1	3.1	3.0

sky brightness and EBL prediction. During the mission, the DIRBE photometric scale was calibrated by observations of bright celestial sources. Table 2.3 lists the absolute calibration source for each wavelength with the uncertainties in the absolute gain.
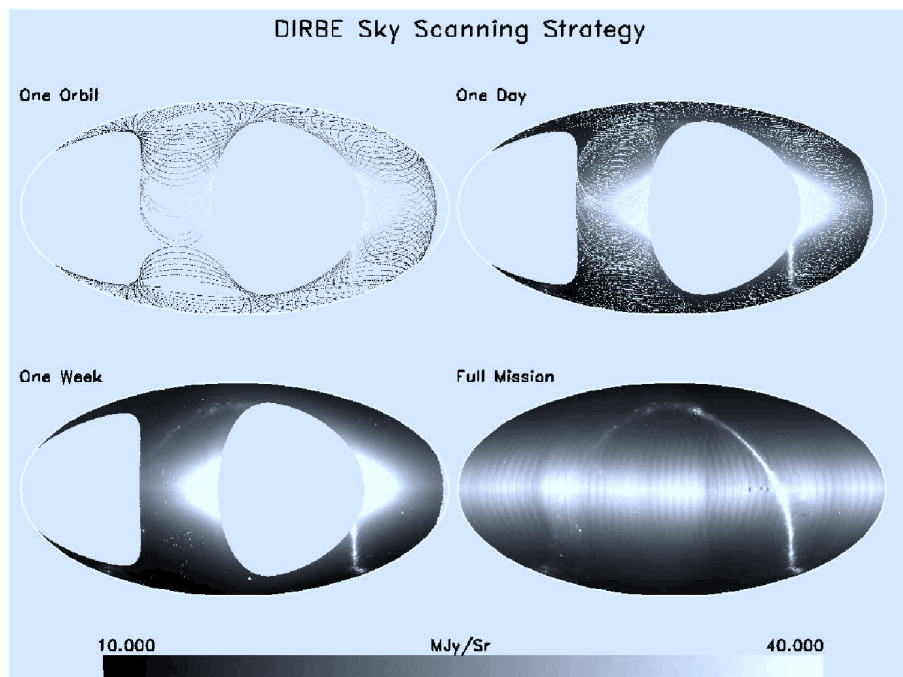
Figure 2.2 Sky coverage achieved for a orbit, a day, a week, and the entire cryogenic mission (COBE/DIRBE explanatory supplement 1998). The maps show the $12\,\mu$m intensity in an ecliptic Mollweide projection.

2.2 The DIRBE data

Telemetry data from the DIRBE instrument were calibrated and converted to various data products through executed set of programs. See COBE/DIRBE Explanatory Supplement (1998) for detail about the data products. This section briefly describes solar elongation (ϵ) = 90° maps used in the present study.

2.2.1 Initial pipeline processing

Unprocessed DIRBE data consisted of $\frac{1}{8}$-second sampled observations of the sky brightness. The attitude used to determine the line of sight in each sample was based on locations of Sun, Earth, and isolated bright stars detected in the $2.2\,\mu$m band. The rms accuracy of the attitude solution is approximately $1.5'$, which is about one order of magnitude smaller than the beam size.

Observations were interrupted when the *COBE* satellite passed through the South Atlantic Anomaly (SAA) or when the instrument calibration stability was checked. The time-ordered sky observations were calibrated photometrically relative to the internal reference source. They were converted to daily sky maps by associating each sample with a pixel on the sky. Pixel area and location were determined by the *COBE* Quadrilateralized Spherical Cube (CSC) projection which is adopted in the DIRBE data products. On average, each pixel in a daily map was observed about 2.4 times while half of the sky is covered.

2.2.2 Solar elongation angle $\epsilon = 90°$ sky map

In the DIRBE observation, a solar elongation angle (ϵ) varies from 64° to 124°. In principle, DIRBE observed the sky with $\epsilon = 90°$ once every 6 months, i.e., once or twice during the 10-month observation. When two $\epsilon = 90°$ observations were made, sky brightness values were different between the two epochs since the Earth was not at the same heliocentric distance at these time and the IPD distribution is not symmetric around the Sun or the ecliptic plane. The $\epsilon = 90°$ sky maps provide the intensity values for each $\epsilon = 90°$ epoch observed for each pixel.

To be precise, few pixels were observed when ϵ was exactly 90°. To create the $\epsilon = 90°$ map, the weekly-averaged intensities were monitored as a function of ϵ as time progressed and then interpolated to $\epsilon = 90°$. Figure 2.3 shows the brightness variation as a function of $\frac{90}{\epsilon} - 1$ for a certain pixel. A straight line was fitted to $I_\nu(\epsilon, \lambda, \beta)$ vs $\frac{90}{\epsilon} - 1$ and the y-intercept was adopted as the $\epsilon = 90°$ intensity for ecliptic coordinates (λ, β). The data used in the fitting was limited within ± 19 days of the $\epsilon = 90°$ point at each pixel to ensure a more linear trend. The weight assigned to each weekly-averaged intensity was based on the
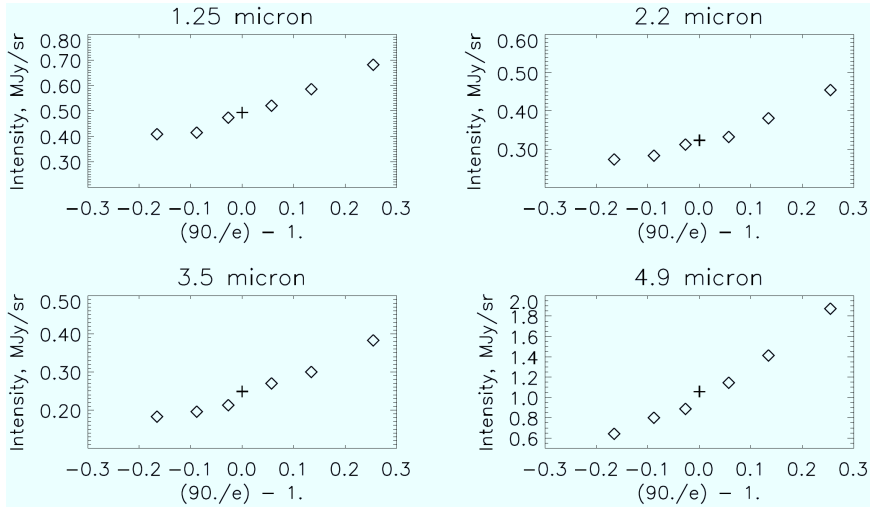
Figure 2.3 Sky brightness as a function of $\frac{90}{\epsilon} - 1$ for DIRBE pixel $(\lambda, \beta) \sim (198.3°, 1.1°)$ at 1.25, 2.2, 3.5, and 4.9 μm (COBE/DIRBE Explanatory Supplement 1998). The diamonds represent weekly-averaged DIRBE intensities and the plus symbols denote the intensities interpolated to $\epsilon = 90°$.

standard deviation of the weekly-averaged value σ_{I_ν}. When the weekly-averaged intensity from 5 or fewer observations, then the weight for that observation was based on $0.01 I_\nu$ or σ_{I_ν}, whichever was greater.

The standard deviation assigned to the interpolated intensity was the formal statistical error in the intercept at $\epsilon = 90°$. For each pixel, pixel number in the CSC projection (i.e., sky coordinates), observation time, interpolated $\epsilon = 90°$ intensity, and the standard deviation are stored as FITS binary table and are available at the DIRBE website, "lambda.gsfc.nasa.gov/product/cobe/". Both the sky coordinates and the observation date for each pixel are necessary to calculate the ZL intensity using the DIRBE ZL model (Kelsall et al. 1998). Figure 2.4 illustrates the intensity of $\epsilon = 90°$ maps in the near-IR four bands, which are created by 6 month observations, starting from 1990 January 1. In the following analysis, these data are used as total near-IR brightnesses.
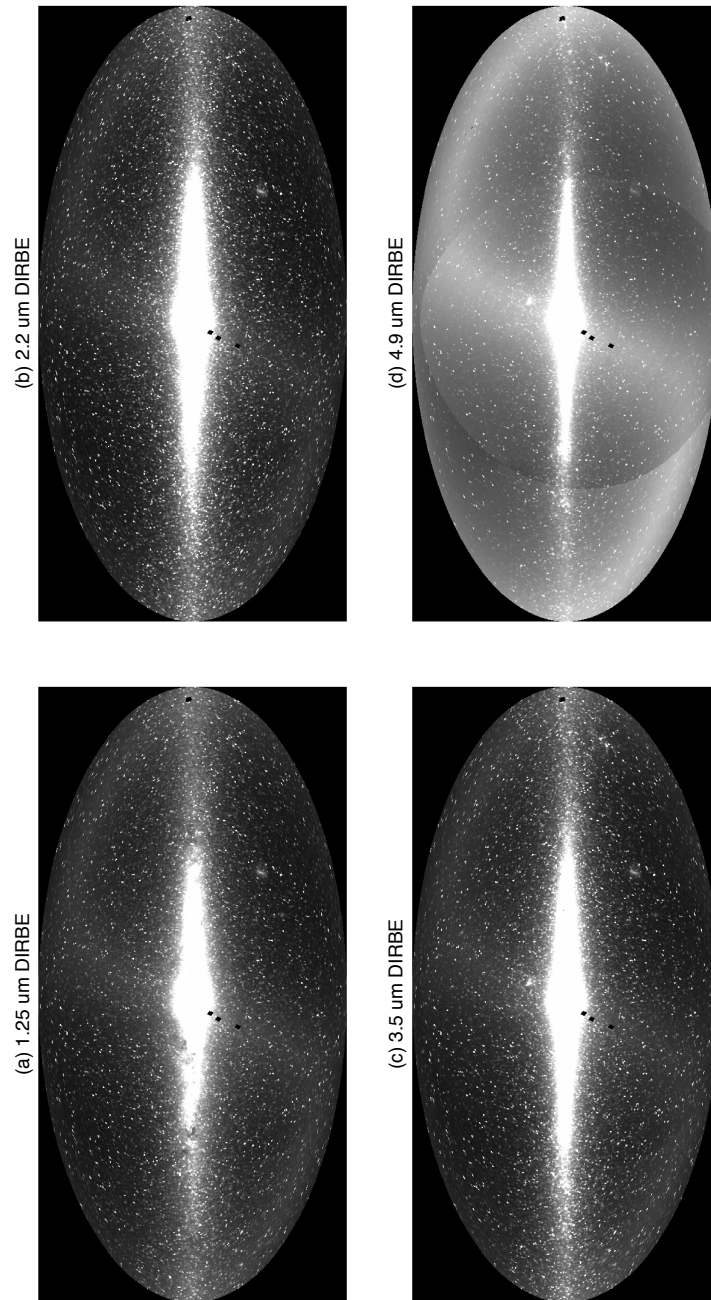
Figure 2.4 All-sky DIRBE $\epsilon = 90°$ intensity maps at 1.25 (panel a), 2.2 (panel b), 3.5 (panel c), and 4.9 μm (panel d) in Galactic Mollweide projection with the Galactic center in the middle. The "S" shape in each panel indicates the ecliptic plane. Each map is arbitrarily scaled for illustration.

2.2.3 *COBE* Quadrilateralized Spherical Cube projection

The *COBE* Quadrilateralized Spherical Cube (CSC) is an approximately equal-area projection in which the celestial sphere is projected onto an inscribed cube. Each cube face is divided into 256×256 pixels; thus, all-sky maps have $256^2 \times 6 = 393216$ pixels, whose scales are approximately $0.32° \times 0.32°$ (COBE/DIRBE Explanatory Supplement 1998). An advantage of the CSC over the Aitoff, Mollweide, and Global-Sinusoidal projections is that the polar singularities are avoided. Figure 2.5 illustrates CSC projection in which Galactic and ecliptic coordinates of each region are indicated. Figure 2.6 compares the CSC and Mollweide projection. The following analysis is performed on the maps in the CSC projection. Characteristics of the near-IR DIRBE data ($\epsilon = 90°$ maps) used in the present study are summarized in Table 2.3.
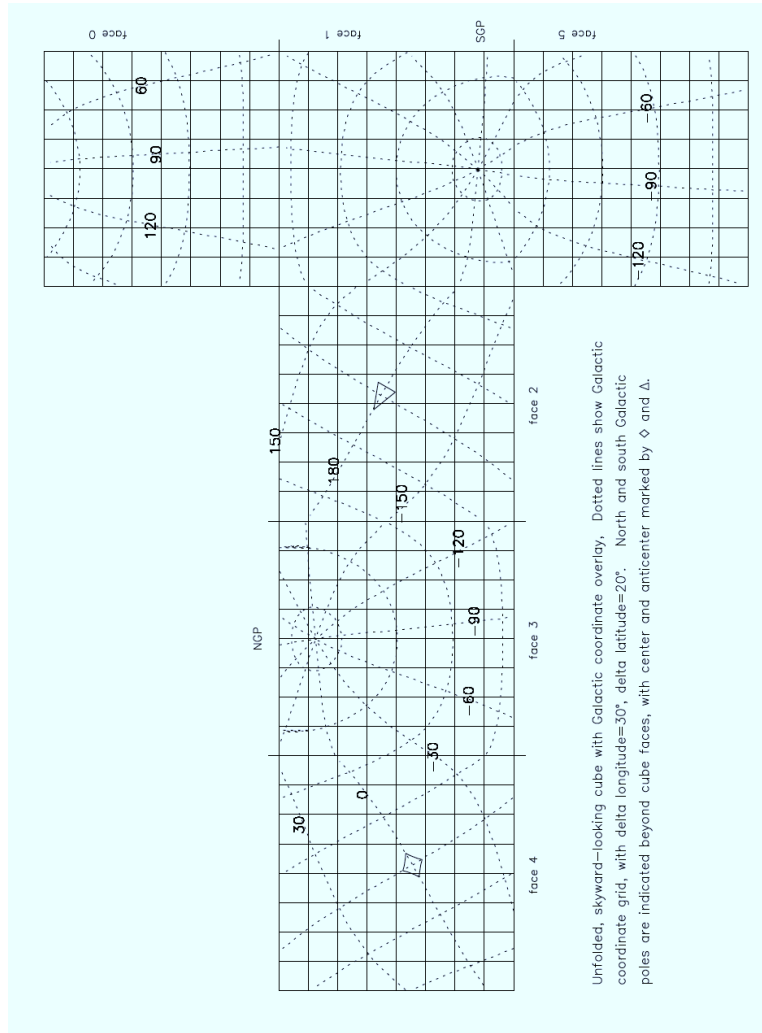
Figure 2.5 All-sky DIRBE maps in the CSC projection (COBE/DIRBE Explanatory Supplement 1998). Unfolded, skyward-looking cube in ecliptic coordinates with Galactic coordinate overlay. The ecliptic plane runs horizontally through the middle of the unfolded cube. The north ecliptic pole is centered on "face 0" and the south ecliptic pole is centered on "face 5". Each grid contains $32 \times 32 = 1024$ pixels.

COBE Quadrilateralized Spherical Cube projection
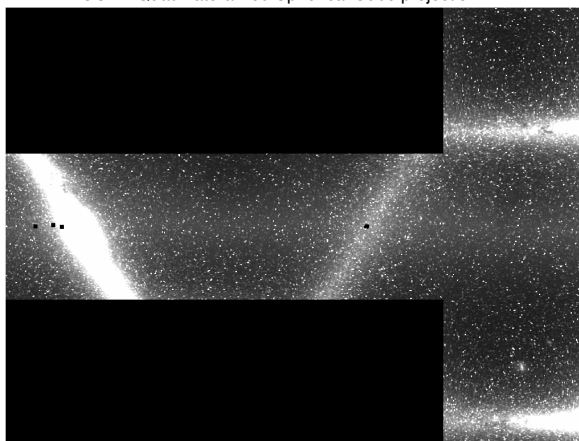
Mollweide projection
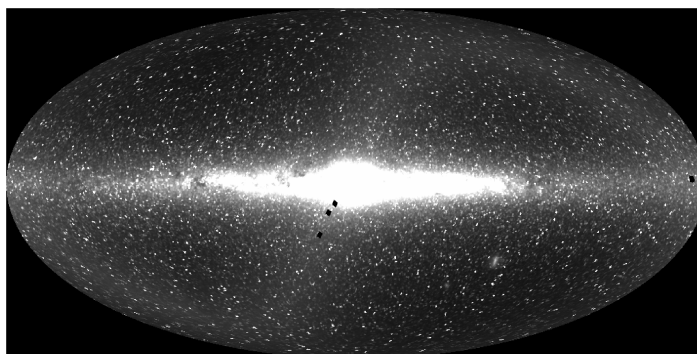
Figure 2.6 All-sky DIRBE $\epsilon = 90°$ maps in the CSC and Mollweide projection at $1.25\,\mu$m.

Chapter 3

Analysis and Result

3.1 Creation of integrated starlight maps from 2MASS and *WISE*

As described in Chapter 1, precise ISL evaluation is necessary to achieve the purpose of this thesis. In the near-IR, the photometric data of all-sky objects are available in 2MASS PSC and AllWISE Source Catalog, which are based on 2MASS and *WISE* project, respectively. Table 3.1 lists the characteristics of these catalogs.

The proposal for 2MASS was submitted by the University of Massachusetts and the Infrared Processing and Analysis Center (IPAC), with Principal Investigator Susan Kleinmann. 2MASS used two 1.3 m telescopes, one at Mt. Hopkins, Arizona, and one at Cerro Tololo, Chile. Each telescope was equipped with a three-channel camera which was capable of observing the sky simultaneously at J (1.24 μm), H (1.66 μm), K_s (2.16 μm). The facility at Mt. Hopkins began survey operations in 1997 June and completed scanning the northern sky in 2000 December. The southern telescope began the operation in 1998

Table 3.1 Characteristics of 2MASS PSC and AllWISE source catalog

Band	2MASS PSC[a]		AllWISE Source Catalog[b]	
	J	K_s	W1	W2
Wavelength (μm)	1.24	2.16	3.4	4.6
Band width (μm)	0.162	0.262	—	—
Sensitivity (mag)	15.8	14.3	16.9	16.0
Zero-mag flux (Jy)	1594	666.7	306.681	170.663
Zero-mag flux uncertainty (Jy)	27.8	12.6	4.60	2.56

[a] Cutri et al. (2003)

[b] Wright et al. (2010)
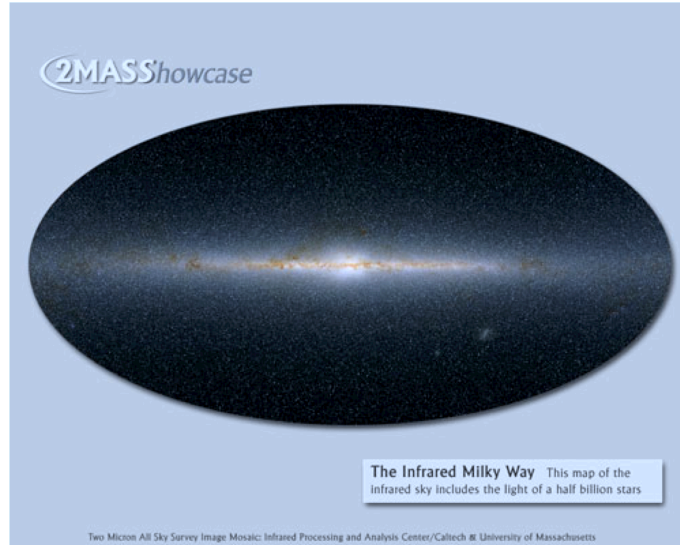
Figure 3.1 All-sky illustration of near-IR sources detected by 2MASS, taken from website "www.ipac.caltech.edu/2mass/gallery/showcase/allsky_stars/index.html".

March and finished the scan in 2001 February. As a result, 99.998% of the sky was scanned and PSC containing $\sim 470,000,000$ objects was published. Figure 3.1 shows all-sky image constructed by the 2MASS sources.

WISE is a MIDEX (medium class Explorer) mission funded by NASA. The project is managed and operated by the Jet Propulsion Laboratory (JPL), with Principal Investigator Edward L. Wright. Figure 3.2 shows the *WISE* flight system. After its launch on 2009 December 14, *WISE* began surveying the sky on 2010 January. *WISE* scanned all sky in four bands centered at 3.4, 4.6, 12, and $22\,\mu$m, which are called W1, W2, W3, and W4 bands, respectively. Based on images obtained by the *WISE* survey, the AllWISE Source Catalog was created. The catalog contains accurate position and photometry of $\sim 750,000,000$ objects.

In the present analysis, integrated brightness maps are created using the 2MASS (1.25 and $2.2\,\mu$m) and AllWISE (3.5 and $4.9\,\mu$m) sources, to estimate the ISL intensity at each region of the sky. Previous studies have reported that the correlation slope between the intensity of DIRBE and that of the 2MASS-derived ISL can deviate from 1.0 by $\sim 10\%$–20% (e.g., Cambrésy et al. 2001; Levenson et al. 2007). This is due to the photometric calibration difference between DIRBE and 2MASS, that is, Sirius was used for DIRBE but several faint stars were for 2MASS. Thus it is necessary that the intensity of the 2MASS-

38
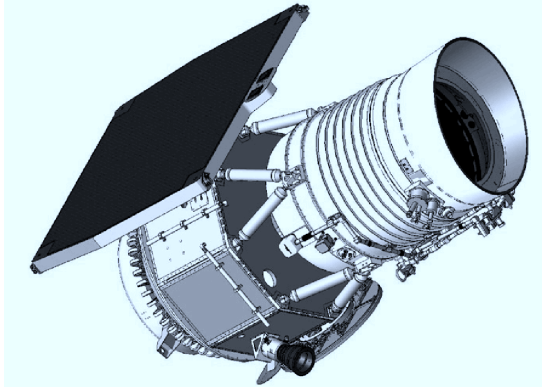
Figure 3.2 *WISE* flight system in survey configuration with cover off (Wright et al. 2010).

derived ISL is scaled to that of the DIRBE by changing the zero magnitude flux density from the originally derived value using the response function of 2MASS. Levenson et al. (2007) conducted the correlation analysis between the integrated brightness of the 2MASS PSC sources and the DIRBE intensity in 40 high Galactic latitude regions. They derived the common zero magnitudes of 1467 and 540 Jy at 1.25 and 2.2 μm, respectively. Accordingly, these values are used as the zero magnitudes in the following analysis at 1.25 and 2.2 μm to convert the magnitude of the 2MASS source to the flux density in the DIRBE band.

As shown in Figure 3.3, because the spectral response function of the *WISE* band is different from that of DIRBE, the flux densities of the sources in the DIRBE bands at 3.5 and 4.9 μm need to be estimated from those in the W1 and W2 bands, respectively. At 3.5 and 4.9 μm, a vast majority of the Galactic sources exhibit the Rayleigh-Jeans spectrum;

$$F_\nu \propto \nu^2, \tag{3.1}$$

where F_ν is the flux density per unit frequency. Then, the conversion formula between the weighted-mean flux density in the *WISE* band (F^{W_i}) and that in the DIRBE band (F^{D_i}) is described as

$$F^{D_i} = \left(\frac{\int F_\nu R_\nu^{D_i}/\nu \, d\nu}{\int R_\nu^{D_i}/\nu \, d\nu} \bigg/ \frac{\int F_\nu R_\nu^{W_i}/\nu \, d\nu}{\int R_\nu^{W_i}/\nu \, d\nu} \right) F^{W_i} \tag{3.2}$$

$$\equiv \alpha_i F^{W_i}, \tag{3.3}$$

where $R_\nu^{D_i}$ and $R_\nu^{W_i}$ are the spectral response functions of DIRBE and *WISE* in the i band, respectively, taken from the COBE/DIRBE explanatory supplement (1998) and Wright et al. (2010). Equation (3.2) adopts the formula of flux density at the isophotal wavelength,

39
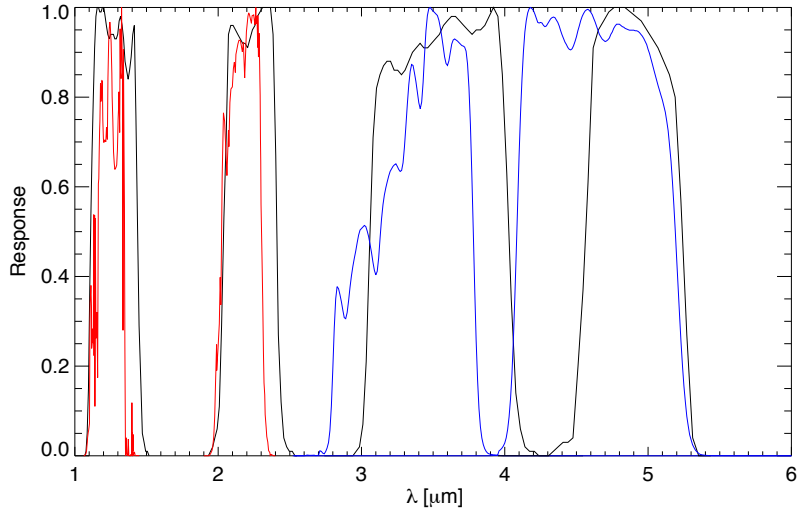
Figure 3.3 Spectral response function of DIRBE (black curves), 2MASS (red curves), and *WISE* (blue curves). Each response curve is normalized at unity. The data of DIRBE, 2MASS, and *WISE* are taken from COBE/DIRBE Explanatory Supplement (1998), Cutri et al. (2003), and Wright et al. (2010), respectively.

which was defined in Tokunaga & Vacca (2005). The derived conversion terms, α_i, are 0.902 and 0.882 at 3.5 and 4.9 μm, respectively.

As described in Wright et al. (2010), F^{W_i} is defined as

$$F^{W_i} = F_0^{W_i} 10^{-0.4m_i}, \tag{3.4}$$

where m_i is the magnitude of the source in the AllWISE catalog and $F_0^{W_i}$ is the zero magnitude at the *WISE* photometric system — 306.681 and 170.663 Jy in the W1 and W2 bands, respectively. The magnitude of the AllWISE source is derived under an assumed source spectrum of $F_\nu \propto \nu^{-2}$ (Wright et al. 2010). As described in Table 1 of Wright et al. (2010), the difference of the flux density between the sources of the Rayleigh-Jeans spectrum $F_\nu \propto \nu^2$ and $F_\nu \propto \nu^{-2}$ is less than 1%. On the other hand, the intensity of the DIRBE map is estimated by assuming $F_\nu \propto \nu^{-1}$ (COBE/DIRBE explanatory supplement 1998), and the divergence from the spectrum of $F_\nu \propto \nu^2$ is less than $\sim 2\%$. These differences associated with the color correction are small in comparison to the ISL value derived in the following section.

In the AllWISE Source Catalog, only point sources (Galactic stars) should be selected for the ISL evaluation. The probability of each source being an extended object is indicated by the digit 0, 1, 2, 3, 4, or 5 in the "ext_flg" of the catalog. The probability increases as
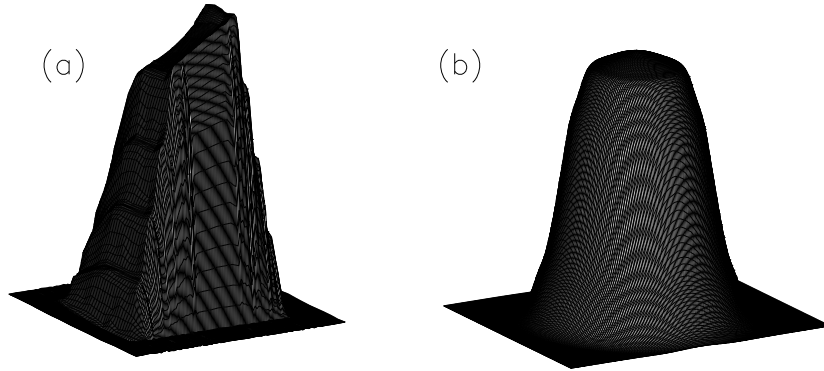
Figure 3.4 Profiles of DIRBE beams. (a): the DIRBE beam for daily maps (FWHM $\simeq 0.7°$) at $1.25\,\mu$m, available as "Beam Profile Maps", in the *COBE*/DIRBE website. (b): an averaged beam (FWHM $\simeq 1°$), created by averaging the beams of the daily maps (a). The ISL maps are created by applying the averaged beam to the 2MASS or AllWISE sources in each band.

the digit increases (see the AllWISE documentation). The sources with ext_flg of 0,1,2 are assumed as the Galactic stars. The selected sources correspond to more than 99% of all AllWISE sources.

To create the ISL maps of the DIRBE spatial resolution, the DIRBE beam is applied to the 2MASS and AllWISE sources. An effective DIRBE beam used to create a daily map at $1.25\,\mu$m is illustrated in Figure 3.4 (a), available from the DIRBE website. This beam profile measures the relative response of the DIRBE to a point source, and includes the sky scanning and data sampling effects. For the $\epsilon = 90°$ maps, the averaged beam should reflect the observation period of 6 months rather than the daily beam, because the intensity of the $\epsilon = 90°$ maps is derived as the average of dozens of observations. As illustrated in Figure 3.4 (b), the averaged beam shapes for the $\epsilon = 90°$ maps are estimated by averaging the daily beam profiles (Figure 3.4 a). Similar averaged profiles are obtained in the four bands, with full width at half-maximums (FWHMs) of $\sim 1°$. Since the beam shapes do not largely depend on the location in the CSC projection sky map adopted for the DIRBE maps (COBE/DIRBE Explanatory Supplement 1998), each 2MASS or AllWISE source is assumed to isotropically transfer its flux to the nearest 13 pixels on the map according to the averaged beam shape (Figure 3.4 b). This method is identical to the ISL calculation presented by Cambrésy et al. (2001).

To all sources brighter than the sensitivity limits in the 2MASS PSC and AllWISE
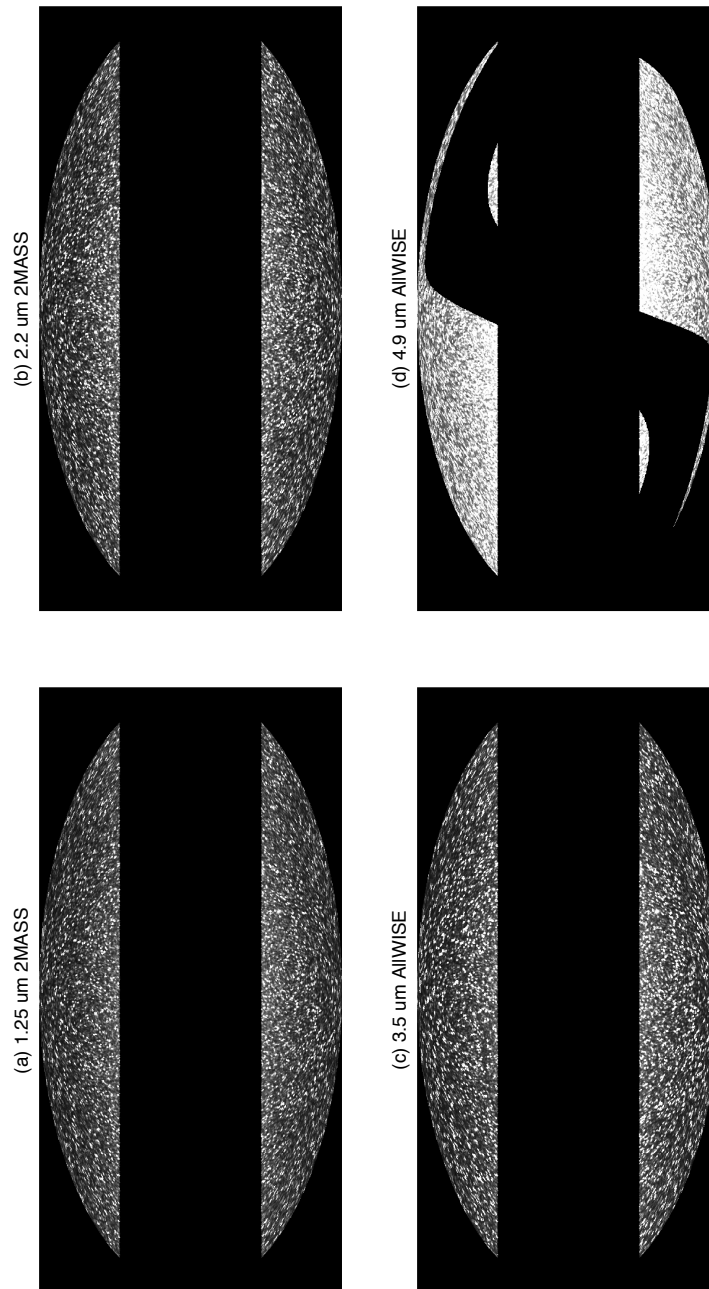
Figure 3.5 Maps of ISL intensity at 1.25 (a), 2.2 (b), 3.5 (c), and 4.9 μm (d), created by 2MASS PSC and AllWISE source catalog. At 1.25, 2.2, and 3.5 μm, the region is limited to high Galactic latitudes ($|b| > 35°$). At 4.9 μm, the region is limited to high Galactic and ecliptic latitudes ($|b| > 35°$ and $|\beta| > 20°$) to reduce the effect of incompleteness in the DIRBE ZL model (Kelsall et al. 1998). The way to create these maps is described in subsection 3.1. Each map is arbitrarily scaled for illustration.

catalog ($J = 15.8$, $K_s = 14.3$, W1 $= 16.9$, and W2 $= 16.0\,\mathrm{mag}$), their integrated intensities, $I_i(\mathrm{DISL})$, are calculated using the averaged DIRBE beam profiles (Figure 3.4 b). These maps are described in Figure 3.5. In contrast to the FSM maps used in the previous DIRBE analysis (Figure 1.15), wherein the surface brightness smoothly changes across the sky, the 2MASS or AllWISE-derived maps show clear fluctuations reflecting the astrometry and photometry of the actual source counts. The created maps are used in the evaluation of the ISL intensity as follows.

3.2 Decomposition analysis

3.2.1 Fitting strategy

To decompose each emission component from the DIRBE maps, a brightness model of the diffuse near-IR radiation is assumed. In the following analysis, intensity of the DIRBE $\epsilon = 90°$ map, $I_i(\mathrm{Obs})$, is modeled as $I_i(\mathrm{Model})$, where the subscript "i" refers to one of the four bands (1.25, 2.2, 3.5 or 4.9 μm). At each band, the sky brightness is assumed to be a linear combination of the four components, i.e., the ZL, DGL, ISL, and residual light including the EBL. The $I_i(\mathrm{Model})$ is therefore described as

$$I_i(\mathrm{Model}) = I_i(\mathrm{ZL}) + I_i(\mathrm{DGL}) + I_i(\mathrm{ISL}) + I_i(\mathrm{Resid}), \qquad (3.5)$$

where $I_i(\mathrm{ZL})$, $I_i(\mathrm{DGL})$, $I_i(\mathrm{ISL})$, and $I_i(\mathrm{Resid})$ indicate the intensities of the ZL, DGL, ISL, and residual light, respectively. These four components are modeled as follows.

The ZL term $I_i(\mathrm{ZL})$ is defined as

$$I_i(\mathrm{ZL}) = a_i I_i(\mathrm{Kel}), \qquad (3.6)$$

where a_i is a free parameter and $I_i(\mathrm{Kel})$ denotes the ZL intensity estimated by the DIRBE ZL model (Kelsall et al. 1998). To evaluate the scaling factor of the model against the DIRBE data themselves, the free parameter a_i is introduced. If the DIRBE ZL model completely reproduces the seasonal variation observed by DIRBE, the parameter a_i should be unity.

The near-IR DGL is thought to contain both scattered light and thermal emission (Chapter 1). The scattered intensity is expected to linearly correlate with that of the 100 μm emission (Equation 1.4). It is natural that the near-IR thermal emission also shows linear correlation against the 100 μm emission. Therefore, the near-IR DGL intensity is modeled as

$$I_i(\mathrm{DGL}) = b_i I_{100}, \qquad (3.7)$$

where b_i is a free parameter and I_{100} denotes the interstellar $100\,\mu$m emission estimated from the SFD map. The different pixel scales between the SFD map ($0.04° \times 0.04°$) and the DIRBE $\epsilon = 90°$ maps ($0.32° \times 0.32°$) cause photometric bias in the analysis. Therefore, an 8×8 pixel binning is applied to the SFD map to obtain the same spatial resolution as that of the DIRBE $\epsilon = 90°$ maps. Lagache et al. (2000) derived the $100\,\mu$m EBL intensity of $0.78 \pm 0.21\,\mathrm{MJy\,sr^{-1}}$. In addition, Matsuoka et al. (2011) showed the intensity correlation of the SFD map and the diffuse optical light observed by *Pioneer 10/11*, and found a correlation break below $\approx 0.8\,\mathrm{MJy\,sr^{-1}}$ on the SFD map, indicating the $100\,\mu$m EBL intensity is an order of $0.8\,\mathrm{MJy\,sr^{-1}}$ (Figure 1.7). Based on these results, the isotropic EBL at $100\,\mu$m is assumed as $0.78\,\mathrm{MJy\,sr^{-1}}$ and this amount is subtracted from the SFD map to obtain the $100\,\mu$m emission from interstellar dust. Interstellar $100\,\mu$m emission is then represented by

$$I_{100} = I_{\mathrm{SFD}} - 0.78\,\mathrm{MJy\,sr^{-1}}, \tag{3.8}$$

with I_{SFD} being the $100\,\mu$m intensity of the binned SFD map.

Using the intensity $I_i(\mathrm{DISL})$ derived from 2MASS and AllWISE stars (section 3.1), the ISL term is defined as

$$I_i(\mathrm{ISL}) = c_i I_i(\mathrm{DISL}), \tag{3.9}$$

where c_i is a free parameter that reflects the contributions of fainter sources than the 2MASS PSC or AllWISE sensitivity limits. At 3.5 and $4.9\,\mu$m, the photometric calibration difference between DIRBE and *WISE* also influences the parameter c_i. The ISL model also assumes that the ISL intensity of fainter sources has same spatial distribution as that of brighter sources, $I_i(\mathrm{DISL})$. In previous studies using the 2MASS data for starlight subtraction (e.g., Cambrésy et al. 2001, Wright 2001) at 1.25 and $2.2\,\mu$m, the analyzed region was sufficiently small to assume isotropic ISL of fainter stars; thus the contributions of fainter stars were subtracted by star-counts models (e.g., Wainscoat et al. 1992). In contrast, the present analysis covers a wide field of the high-latitude sky, where the ISL of fainter and brighter stars may have the similar spatial distribution.

The residual light $I_i(\mathrm{Resid})$, which includes the EBL, is assumed to be independent of the region. It is defined as

$$I_i(\mathrm{Resid}) = d_i, \tag{3.10}$$

where d_i is a free parameter.

At this stage, the model of the diffuse near-IR emission, $I_i(\mathrm{Model})$ is described as

$$I_i(\mathrm{Model}) = I_i(\mathrm{ZL}) + I_i(\mathrm{DGL}) + I_i(\mathrm{ISL}) + I_i(\mathrm{Resid}) \tag{3.11}$$

$$= a_i I_i(\mathrm{Kel}) + b_i I_{100} + c_i I_i(\mathrm{DISL}) + d_i. \tag{3.12}$$

44

Table 3.2 Number of pixels used in decomposition analysis

Band	1.25 μm ($|b| > 35°$)	2.2 μm ($|b| > 35°$)	3.5 μm ($|b| > 35°$)	4.9 μm ($|b| > 35°$, $|\beta| > 20°$)
Total pixels[a]	167702	167702	167702	97772
Used pixels[b]	116578	119394	103709	64363

[a] Number of pixels in $|b| > 35°$ (1.25, 2.2, 3.5 μm) and in $|b| > 35°$, $|\beta| > 20°$ (4.9 μm).

[b] Number of pixels survived the masking procedure (subsection 3.2.1).

Prior to the determination of each parameter, some specific regions that might perturb the analysis should be removed. As suggested by the Explanatory Supplement to the 2MASS All Sky Data Release and Extended Mission Products (Cutri et al. 2003), the high Galactic latitude region of $|b| > 35°$ is free from the reddening effect due to the Galactic extinction at 1.25 and 2.2 μm. In order not to break the linear combination model (Equation 3.12), analyzed regions are limited to the $|b| > 35°$ region. Kelsall et al. (1998) pointed out that the DIRBE ZL model leaves systematic residuals in the low-ecliptic latitudes of $|\beta| < 15°$ at 4.9 μm. Therefore, the analyzed region is limited to $|b| > 35°$ and $|\beta| > 20°$ at 4.9 μm.

The circular regions around the Magellanic Clouds and probable Galactic extended sources are also removed. To suppress the large photometric uncertainty of bright stars, the pixels around stars brighter than $J = 5$, $K_s = 4$, W1 = 4, and W1 = 4 mag at 1.25, 2.2, 3.5, and 4.9 μm respectively, are masked. Furthermore, regions with $I_{\rm SFD} < 10\,{\rm MJy\,sr^{-1}}$ at 1.25 and 2.2 μm and $I_{100} < 6\,{\rm MJy\,sr^{-1}}$ at 3.5 and 4.9 μm are selected. In addition, outliers are excluded by applying 2-sigma clipping to the ISL intensities, $I_i({\rm DISL})$. The AllWISE sources in the ecliptic longitude range of 44.7°~54.8° or 230.9°~238.7°, which were observed during the early 3-band Cryo phase of the *WISE* mission, are reported to have missing or elevated uncertainty in the W1 band. These regions are excluded in the analysis at 3.5 μm. As shown in Table 3.2, approximately 60%–70% of the region survived these masking procedures. The survived regions are used in the following analysis.

Finally, each component is decomposed from the DIRBE intensity according to Equation (3.12). To determine the parameters a_i, b_i, c_i, and d_i, the following χ^2 function is minimized in each band:

$$\chi_i^2 = \sum_j \frac{[I_i({\rm Obs}) - I_i({\rm Model})]^2}{\sigma_i^2} \tag{3.13}$$

$$= \sum_j \frac{[I_i({\rm Obs}) - a_i I_i({\rm Kel}) - b_i I_{100} - c_i I_i({\rm DISL}) - d_i]^2}{\sigma_i^2}, \tag{3.14}$$

where "j" refers to the pixels used in this fitting.

The total uncertainty, σ_i, at each pixel is calculated as

$$\sigma_i^2 = \sigma_i^2(\mathrm{Obs}) + b_i^2 \sigma_{100}^2 + c_i^2 \sigma_i^2(\mathrm{DISL}), \tag{3.15}$$

where $\sigma_i(\mathrm{Obs})$, σ_{100}, and $\sigma_i(\mathrm{DISL})$ are the standard deviations of the intensities of the $\epsilon = 90°$ map, that of the $100\,\mu\mathrm{m}$ emission, and that of the ISL intensity $I_i(\mathrm{DISL})$, respectively. The value $\sigma_{100} = 0.35\,\mathrm{MJy\,sr^{-1}}$ is derived by Ienaka et al. (2013). The $\sigma_i(\mathrm{DISL})$ at each pixel is calculated in the same way as $I_i(\mathrm{DISL})$, convolved with the DIRBE beam profile (see section 3.1). At 1.25 and $2.2\,\mu\mathrm{m}$, the $\sigma_i(\mathrm{DISL})$ is calculated as

$$\sigma_i^2(\mathrm{DISL}) = [-0.4\,(\log 10)\,10^{-0.4 m_i}\sigma_{m_i} F_{i0}]^2, \tag{3.16}$$

where m_i, σ_{m_i}, and F_{i0} denotes the magnitude of each cataloged source, the uncertainty, and the zero-magnitude flux, respectively. At 3.5 and $4.9\,\mu\mathrm{m}$, the $\sigma_i(\mathrm{DISL})$ is calculated as

$$\sigma_i^2(\mathrm{DISL}) = [\alpha_i 10^{-0.4 m_i}]^2 \sigma_{F_0^{W_i}}^2 + [-0.4\,(\log 10)\,10^{-0.4 m_i}\alpha_i F_0^{W_i}]^2 \sigma_{m_i}^2 + [F_0^{W_i} 10^{-0.4 m_i}]^2 \sigma_{\alpha_i}^2, \tag{3.17}$$

where $\sigma_{F_0^{W_i}}$ and σ_{α_i}, respectively, denote the uncertainties of the zero magnitude in the *WISE* band and that of the conversion factor α_i, set to be 1% of α_i. Sources with no uncertainty entry in the 2MASS PSC or AllWISE Source Catalog are assigned an uncertainty, σ_{m_i}, of $0.5\,\mathrm{mag}$.

3.2.2 All-sky results

By conducting the fitting, the parameters a_i, b_i, c_i, and d_i are determined. The results of the decomposition analysis at 1.25, 2.2, 3.5, and $4.9\,\mu\mathrm{m}$ in high Galactic latitudes ($|b| > 35°$) are shown in Figure 3.6, 3.7, 3.8, and 3.9, respectively. Filled circles and error bars in each panel, respectively, represent the weighted means $\overline{y_i}$ and the uncertainties $\overline{\sigma_i}$ of the data within a certain x-axis range, which are defined as

$$\overline{y_i} = \sum_k \frac{y_i}{\sigma_i^2} \Big/ \sum_k \frac{1}{\sigma_i^2}, \tag{3.18}$$

$$\overline{\sigma_i}^2 = 1 \Big/ \sum_k \frac{1}{\sigma_i^2}, \tag{3.19}$$

where k denotes the data within each bin. y_i and σ_i indicate, respectively, the value of each data and the uncertainty calculated from Equation (3.15). The number of the points within a certain x-axis range is shown in the bottom histogram of each panel. Each panel shows that the four components are decomposed from the DIRBE sky brightness, according to the assumed linear combination model (Equation 3.12). In particular, Panels (b) of the

46

figures illustrate the linear correlation between the intensity of interstellar $100\,\mu$m emission and that of the diffuse near-IR light, which confirms the presence of a DGL component in the high-latitude diffuse ISM.

Table 3.3 and 3.4 list the parameters a_i, b_i, c_i, and d_i determined by the decomposition analysis in high Galactic latitudes ($|b| > 35°$). The determined values and their statistical uncertainties are listed in the "Result" and "Statistical" rows, respectively. Owing to the large sample size with over tens of thousands of points, the statistical uncertainty of each component is small.

Table 3.5 exhibits the typical intensity of each component derived in the high-latitude region. At $4.9\,\mu$m, the ZL accounts for more than 95% of the sky brightness on average. Such a strong ZL intensity makes the analysis more difficult and causes larger deviation from the linear correlation in the faint DGL decomposition (Figure 3.9 b).
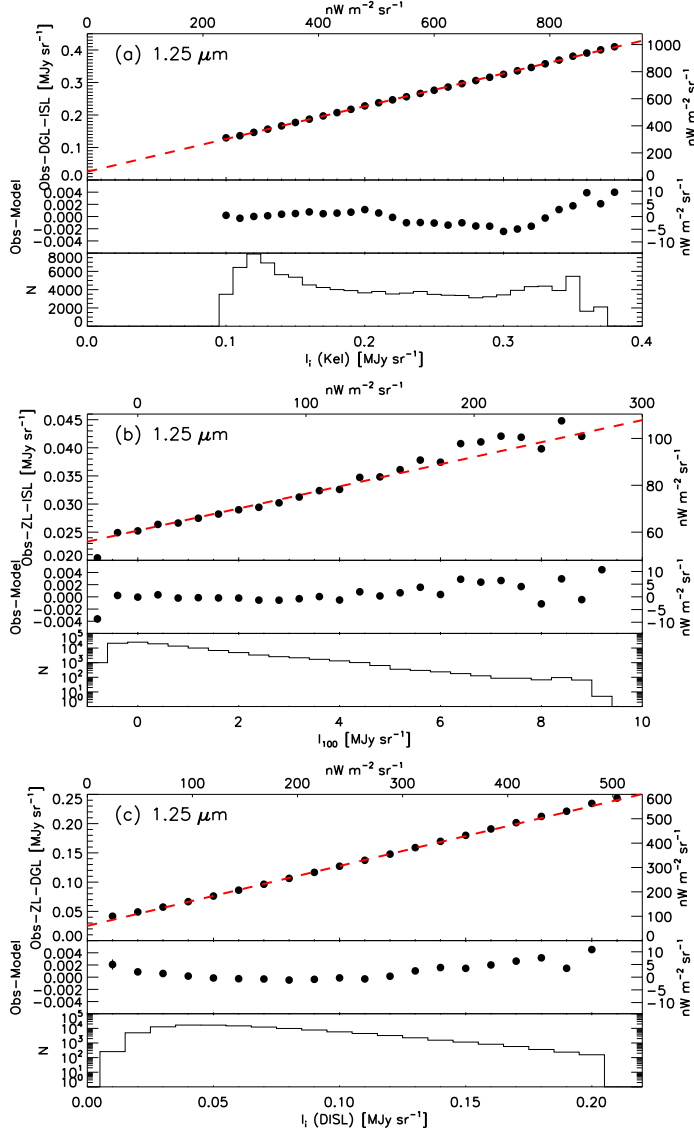
Figure 3.6 Result of the decomposition analysis at $1.25\,\mu$m ($|b| > 35°$). The panel (a) plots $I_i(\mathrm{Obs}) - I_i(\mathrm{DGL}) - I_i(\mathrm{ISL})$ (i.e., $a_i I_i(\mathrm{Kel}) + d_i$) vs $I_i(\mathrm{Kel})$; the panel (b) plots $I_i(\mathrm{Obs}) - I_i(\mathrm{ZL}) - I_i(\mathrm{ISL})$ (i.e., $b_i I_{100} + d_i$) vs I_{100}, and the panel (c) plots $I_i(\mathrm{Obs}) - I_i(\mathrm{ZL}) - I_i(\mathrm{DGL})$ (i.e., $c_i I_i(\mathrm{DISL}) + d_i$) vs $I_i(\mathrm{DISL})$. In each panel, determined parameters are indicated by the red dashed lines. The middle and bottom parts of each panel plot $I_i(\mathrm{Obs}) - I_i(\mathrm{Model})$ and the number of pixels, respectively. Filled circles and error bars represent the weighted means and standard errors of the sample within an arbitrary x-axis bin, which are calculated by Equation (3.18) and (3.19), respectively.

48
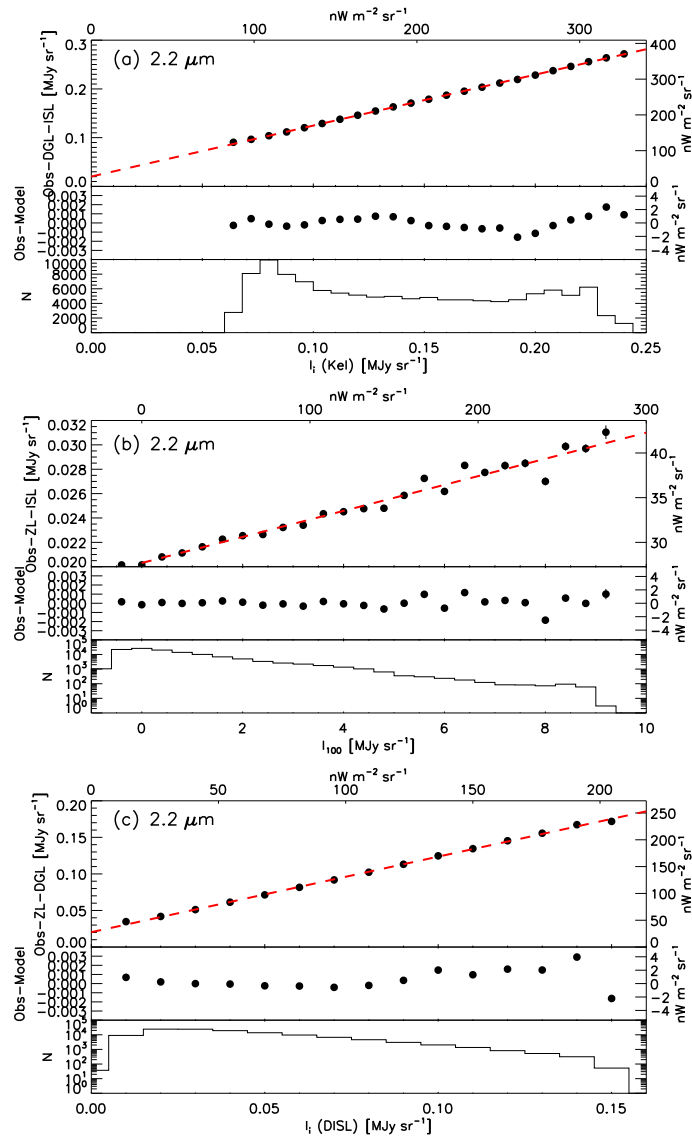
Figure 3.7 Same as Figure 3.6, but at $2.2\,\mu\mathrm{m}$ ($|b| > 35°$).
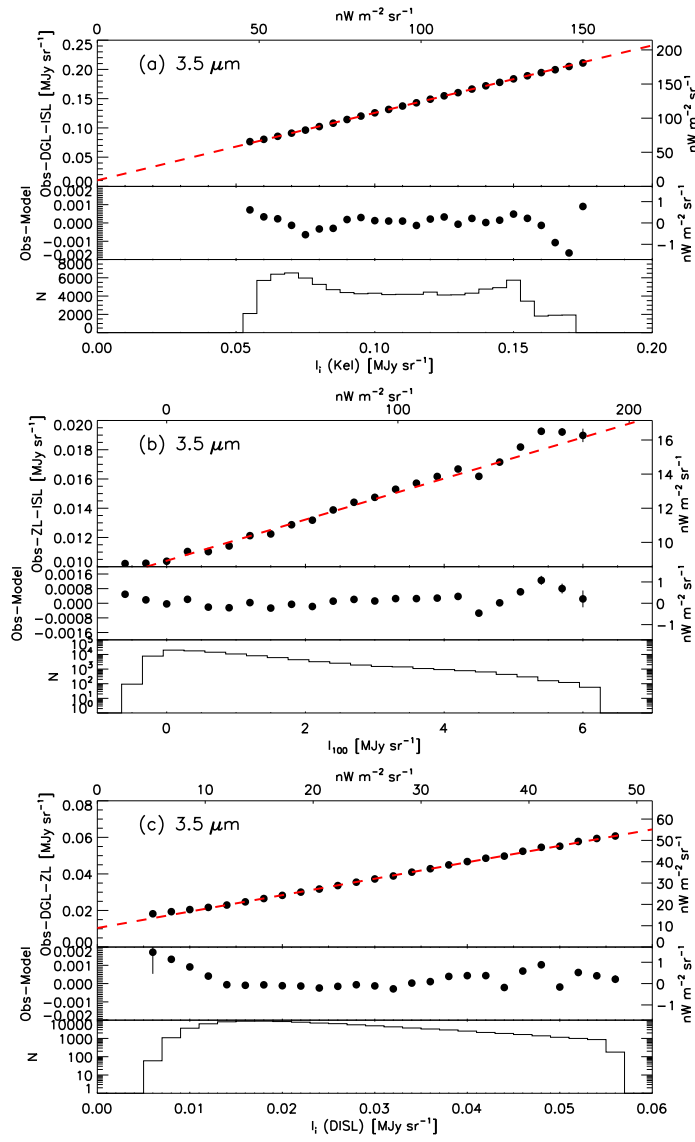
Figure 3.8 Same as Figure 3.6, but at $3.5\,\mu\mathrm{m}$ ($|b| > 35°$).
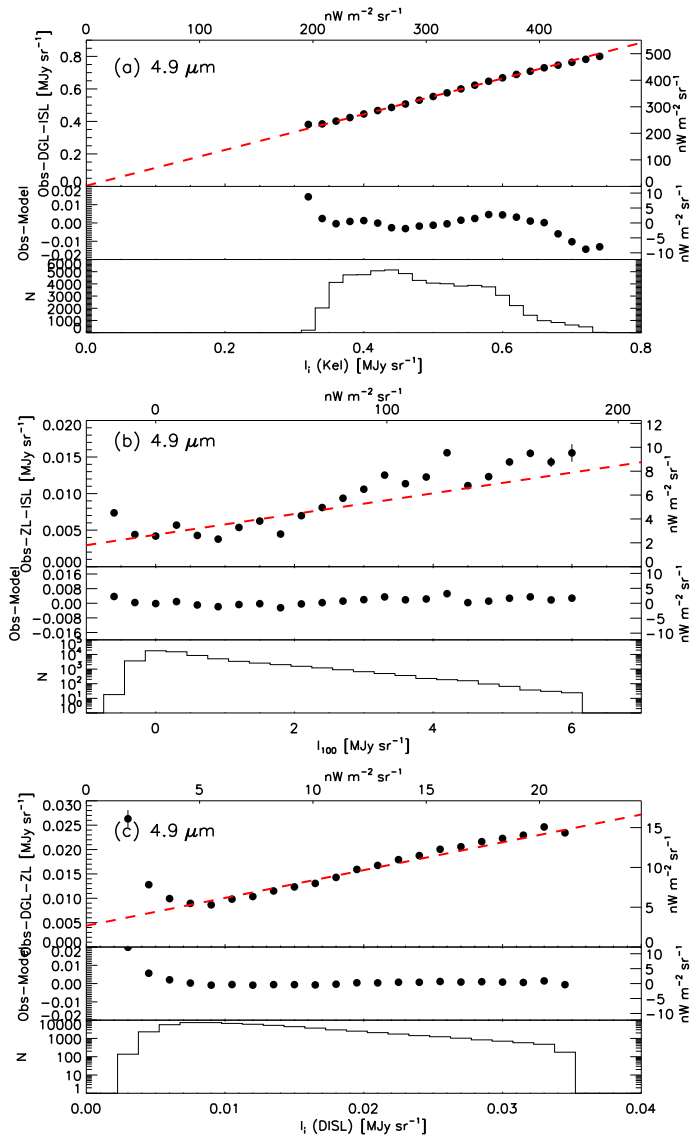
Figure 3.9 Same as Figure 3.6, but at $4.9\,\mu$m ($|b| > 35°$ and $|\beta| > 20°$).

Table 3.3 Results of decomposition analysis for parameters a_i, b_i, and c_i

Band (μm)	a_i (MJy sr^{-1})/(MJy sr^{-1})				$\nu_i b_i$ (nW m^{-2} sr^{-1})/(MJy sr^{-1})				c_i (MJy sr^{-1})/(MJy sr^{-1})			
	1.25	2.2	3.5	4.9	1.25	2.2	3.5	4.9	1.25	2.2	3.5	4.9
Result	1.0079	1.0447	1.1531	1.1003	4.72	1.46	1.205	0.868	1.0236	1.0330	0.899	0.570
Statistical	0.0001	0.0002	0.0003	0.0002	0.02	0.01	0.008	0.010	0.0003	0.0004	0.001	0.002
Regional variation	0.012	0.012	0.0282	0.0506	2.83	0.99	0.433	2.042	0.014	0.011	0.015	0.254
Quadrature sum	0.012	0.012	0.0282	0.0506	2.83	0.99	0.433	2.042	0.014	0.011	0.015	0.254

Table 3.4 Results of decomposition analysis for parameter d_i

Band (μm)	$\nu_i d_i$ (nW m^{-2} sr^{-1})			
	1.25	2.2	3.5	4.9
Result	60.66	27.69	8.92	2.67
Statistical	0.08	0.04	0.04	0.05
Regional variation	5.77	1.35	2.59	14.12
Gain	1.88	0.86	0.28	0.08
Galaxies	0.12	0.14	0.04	0.04
ZL model	15	6	2.1	5.9
Quadrature sum	16.18	6.21	3.35	15.30

Table 3.5 Typical intensity of each component

Component (nW m^{-2} sr^{-1})	1.25 μm	2.2 μm	3.5 μm	4.9 μm
$\nu_i I_i(\mathrm{ZL}) = \nu_i a_i I_i(\mathrm{Kel})$	539.3 ± 197.3	198.8 ± 70.7	108.1 ± 32.3	334.2 ± 61.6
$\nu_i I_i(\mathrm{DGL}) = \nu_i b_i I_{100}$	4.7 ± 6.1	1.4 ± 1.9	1.0 ± 1.3	0.4 ± 0.8
$\nu_i I_i(\mathrm{ISL}) = \nu_i c_i I_i(\mathrm{DISL})$	170.9 ± 78.5	64.0 ± 33.5	20.0 ± 8.2	5.0 ± 2.3
$\nu_i I_i(\mathrm{Resid}) = \nu_i d_i$	60.7 ± 16.2	27.7 ± 6.2	8.9 ± 3.4	2.7 ± 15.3
$\nu_i I_i(\mathrm{Obs})$	787.1 ± 220.3	304.2 ± 87.4	138.7 ± 36.1	343.2 ± 62.7

Note. — Except for $I_i(\mathrm{Resid})$, intensity is represented by its average and the standard deviation of the analyzed samples.

3.2.3 Regional variation of emission components

To investigate the regional variation of each parameter, the decomposition analysis is conducted in divided regions as a function of l and b. As explained in Chapter 1, b-dependence of the scattered DGL measures the scattering anisotropy of the interstellar dust grains.

The analyzed high-b region is divided into six Galactic longitude fields, i.e., $0° < l < 60°$, $60° < l < 120°$, $120° < l < 180°$, $180° < l < 240°$, $240° < l < 300°$, and $300° < l < 360°$. In each region, the fitting method is identical to that described in subsection 3.2.1. The results obtained in each region at each band are summarized in Table 3.6. Because each region contains over several thousand points, the statistical uncertainty in this analysis remains small. Figure 3.10, 3.11, 3.12, and 3.13 illustrate, respectively, the determined parameters at 1.25, 2.2, 3.5, and 4.9 μm in each Galactic longitude region. Though there seems no systematic dependence, each parameter varies as a function of l. Therefore, the standard deviation of the parameters obtained in the six regions is assumed as a typical variation of the results at each band. The values are listed in the row "Regional variation" in Table 3.3 and 3.4. The "Regional variation" is dominant over the "Statistical" uncertainty. In the following, quadrature sum of "Statistical" and "Regional variation" is used as total uncertainties of the parameters a_i, b_i, and c_i in high-b region.

The regional variation may be caused by the simultaneous decomposition of each component from the sky brightness. If some components have similar spatial distributions in a region, it is possible that the component is partly absorbed or given by other components, so called "multicollinearity". Difference of the degree of multicollinearity among the analyzed regions causes the regional variation in the fitting results. This phenomenon is inevitable in the decomposition analysis of multiple components over the wide field of the sky.

At 1.25 and 2.2 μm, the parameters obtained in the six regions are randomly distributed around those derived in the $|b| > 35°$ field (Figure 3.10 and 3.11). At 3.5 μm, however, the panels (b) and (c) of Figure 3.12 show that all or most of the values at the six divided regions fall into one side of the all-sky value. These phenomena may be attributed to the intensity difference of each component. As shown in Table 3.5, at 3.5 μm, the typical intensity of the ZL can be 10 to 100 times higher than that of the ISL and DGL. In this situation, the small difference of the ZL intensity between each region could cause the biased fitting results in the ISL and DGL components. Similarly at 4.9 μm, the "Regional variation" of each parameter is significantly larger than those derived in the other bands (Figure 3.13).

Table 3.6 Fitting results in six Galactic longitude-divided regions

Band (μm)	Region (deg)	Number of pixels	a_i (MJy sr^{-1}/MJy sr^{-1})	$\nu_i b_i$ (nW m^{-2} sr^{-1}/MJy sr^{-1})	c_i (MJy sr^{-1}/MJy sr^{-1})	$\nu_i d_i$ (nW m^{-2} sr^{-1})
1.25	$\|b\| > 35$	116578	1.0079 ± 0.0001	4.72 ± 0.02	1.0236 ± 0.0003	60.66 ± 0.08
1.25	$0 < l < 60$	18557	1.0013 ± 0.0004	8.57 ± 0.05	1.0201 ± 0.0009	65.0 ± 0.2
1.25	$60 < l < 120$	19714	0.9949 ± 0.0003	2.01 ± 0.05	1.0265 ± 0.0008	64.8 ± 0.2
1.25	$120 < l < 180$	19582	0.9988 ± 0.0003	5.46 ± 0.04	1.0237 ± 0.0009	69.1 ± 0.2
1.25	$180 < l < 240$	20275	1.0222 ± 0.0003	3.98 ± 0.04	0.9986 ± 0.0008	56.4 ± 0.2
1.25	$240 < l < 300$	19516	1.0224 ± 0.0002	0.61 ± 0.06	1.0224 ± 0.0008	53.9 ± 0.2
1.25	$300 < l < 360$	18934	1.0018 ± 0.0003	5.61 ± 0.05	1.0407 ± 0.0009	59.6 ± 0.2
2.2	$\|b\| > 35$	119394	1.0447 ± 0.0002	1.46 ± 0.01	1.0330 ± 0.0004	27.69 ± 0.04
2.2	$0 < l < 60$	18852	1.0346 ± 0.0006	2.75 ± 0.03	1.0386 ± 0.0011	28.04 ± 0.13
2.2	$60 < l < 120$	20309	1.0282 ± 0.0004	0.91 ± 0.03	1.0407 ± 0.0010	29.31 ± 0.10
2.2	$120 < l < 180$	20213	1.0530 ± 0.0005	1.33 ± 0.02	1.0289 ± 0.0011	27.93 ± 0.11
2.2	$180 < l < 240$	20748	1.0488 ± 0.0005	1.24 ± 0.02	1.0196 ± 0.0011	28.99 ± 0.11
2.2	$240 < l < 300$	20011	1.0596 ± 0.0004	-0.14 ± 0.03	1.0312 ± 0.0010	26.07 ± 0.10
2.2	$300 < l < 360$	19261	1.0358 ± 0.0005	2.06 ± 0.02	1.0508 ± 0.0010	26.28 ± 0.12
3.5	$\|b\| > 35$	103709	1.1531 ± 0.0003	1.20 ± 0.01	0.8992 ± 0.0010	8.92 ± 0.04
3.5	$0 < l < 60$	15233	1.1707 ± 0.0012	1.38 ± 0.02	0.9394 ± 0.0028	3.96 ± 0.12
3.5	$60 < l < 120$	18416	1.1453 ± 0.0007	1.61 ± 0.02	0.9095 ± 0.0025	8.37 ± 0.08
3.5	$120 < l < 180$	18264	1.1637 ± 0.0008	1.36 ± 0.02	0.9224 ± 0.0027	8.71 ± 0.08
3.5	$180 < l < 240$	16990	1.1498 ± 0.0009	1.52 ± 0.03	0.9440 ± 0.0028	10.80 ± 0.10
3.5	$240 < l < 300$	18064	1.1834 ± 0.0007	0.57 ± 0.02	0.9098 ± 0.0025	7.19 ± 0.08
3.5	$300 < l < 360$	16742	1.1024 ± 0.0007	1.84 ± 0.02	0.9156 ± 0.0027	10.95 ± 0.10
4.9	$\|b\| > 35,\ \|\beta\| > 20$	64363	1.1003 ± 0.0002	0.87 ± 0.01	0.570 ± 0.002	2.67 ± 0.05
4.9	$0 < l < 60$	10858	1.1008 ± 0.0005	-1.34 ± 0.02	0.763 ± 0.006	-5.78 ± 0.20
4.9	$60 < l < 120$	10785	1.0345 ± 0.0006	3.65 ± 0.03	0.432 ± 0.006	18.28 ± 0.16
4.9	$120 < l < 180$	10930	1.1544 ± 0.0004	0.75 ± 0.03	0.737 ± 0.005	-11.09 ± 0.14
4.9	$180 < l < 240$	11888	1.1157 ± 0.0005	1.25 ± 0.02	0.870 ± 0.006	6.01 ± 0.19
4.9	$240 < l < 300$	10329	1.1814 ± 0.0005	-1.24 ± 0.03	1.218 ± 0.006	-22.71 ± 0.15
4.9	$300 < l < 360$	9573	1.1024 ± 0.0004	2.78 ± 0.03	0.745 ± 0.006	-3.84 ± 0.16

Note. — Error associated with each parameter represents the statistical uncertainty determined by the fitting.
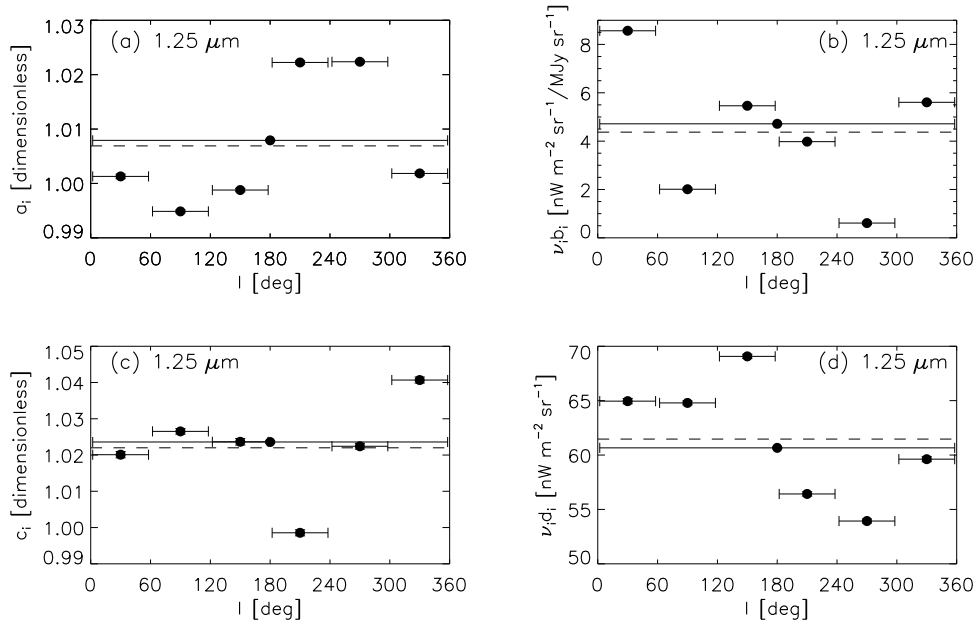
Figure 3.10 Parameter variation as a function of Galactic longitude at $1.25\,\mu$m. Panels (a), (b), (c), and (d) illustrate, respectively, longitudinal variation for parameters a_i, b_i, c_i and d_i. Black circles are the parameters derived in the six-divided and $|b| > 35°$ regions with horizontal error bars indicating the analyzed field. Horizontal dashed lines represent averages of the six-divided regions.
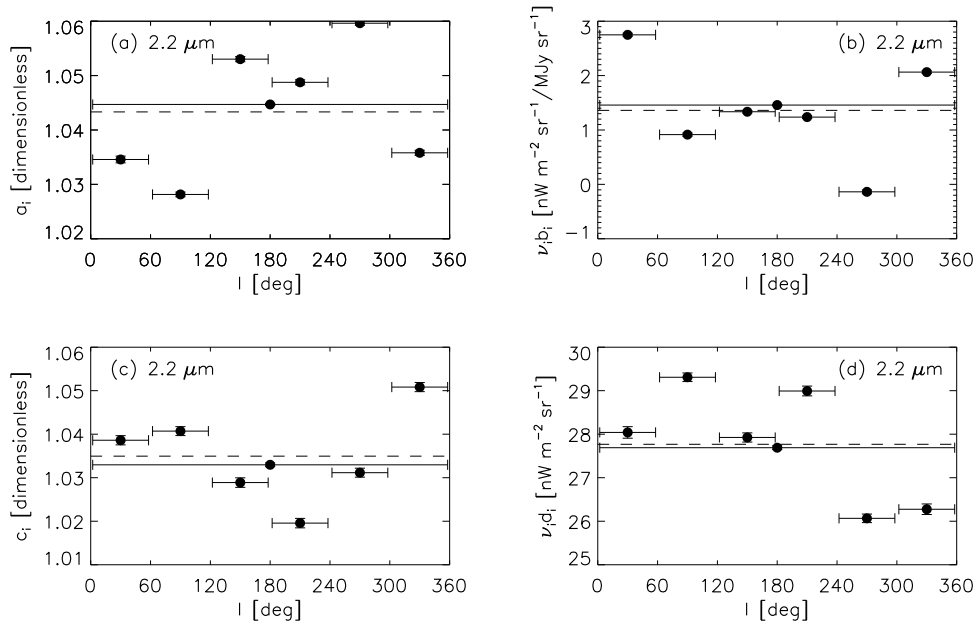
Figure 3.11 Same as Figure 3.10, but at $2.2\,\mu\mathrm{m}$
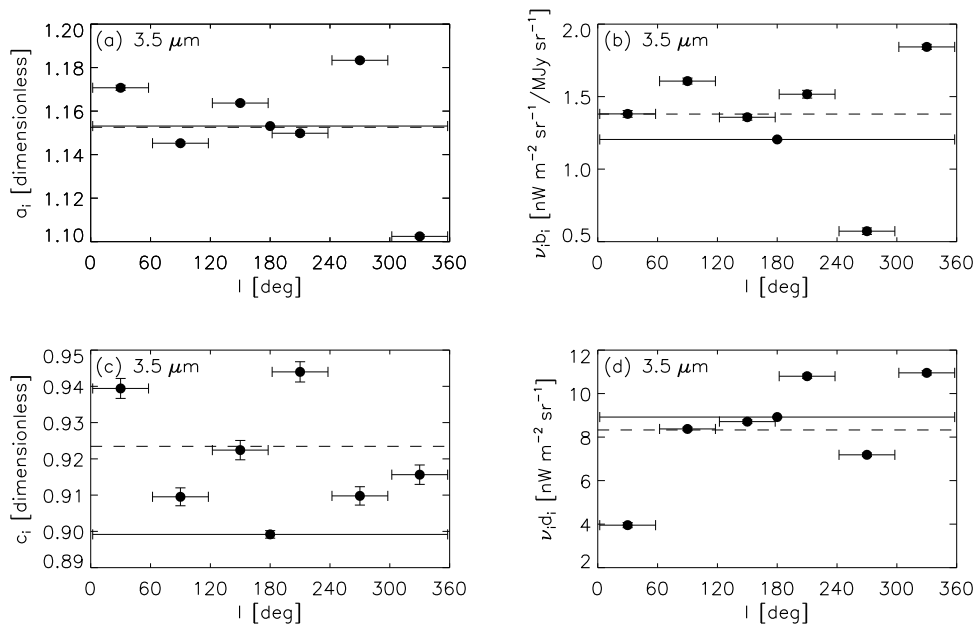
Figure 3.12 Same as Figure 3.10, but at $3.5\,\mu\mathrm{m}$

57
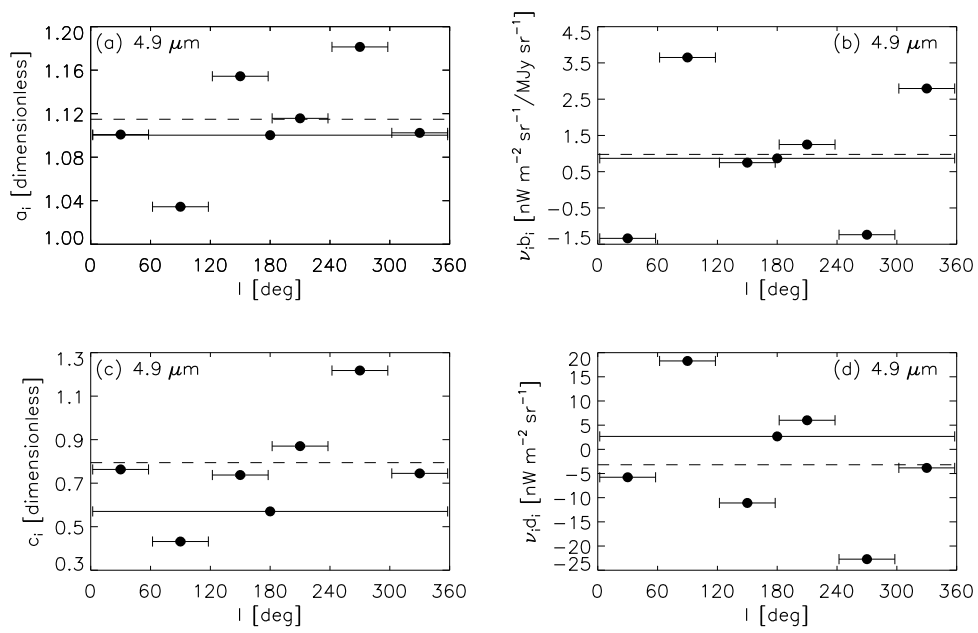
Figure 3.13 Same as Figure 3.10, but at $4.9\,\mu$m.

Table 3.7 Fitting results in five Galactic latitude-divided regions

Band (μm)	Region (deg)	Number of pixels	$\nu_i b_i$ (nW m^{-2} sr^{-1}/MJy sr^{-1})	c_i (MJy sr^{-1}/MJy sr^{-1})	$\nu_i d_i$ (nW m^{-2} sr^{-1})
1.25	$|b| > 35$	116578	4.72 ± 0.02	1.0236 ± 0.0003	60.66 ± 0.08
1.25	$25 < |b| < 30$	15683	6.64 ± 0.03	1.0582 ± 0.0008	59.89 ± 0.26
1.25	$30 < |b| < 35$	17108	6.08 ± 0.03	1.0356 ± 0.0008	63.77 ± 0.22
1.25	$35 < |b| < 40$	17215	4.33 ± 0.03	1.0192 ± 0.0008	67.06 ± 0.20
1.25	$40 < |b| < 45$	17136	3.98 ± 0.04	1.0086 ± 0.0009	66.60 ± 0.18
1.25	$45 < |b| < 90$	82227	3.26 ± 0.03	1.0063 ± 0.0004	62.57 ± 0.06
2.2	$|b| > 35$	119394	1.46 ± 0.01	1.0330 ± 0.0004	27.69 ± 0.04
2.2	$25 < |b| < 30$	15772	1.80 ± 0.02	1.0725 ± 0.0010	29.88 ± 0.12
2.2	$30 < |b| < 35$	17278	1.62 ± 0.02	1.0444 ± 0.0010	30.53 ± 0.10
2.2	$35 < |b| < 40$	17167	1.14 ± 0.02	1.0315 ± 0.0010	30.44 ± 0.10
2.2	$40 < |b| < 45$	17303	1.01 ± 0.02	1.0204 ± 0.0011	30.17 ± 0.09
2.2	$45 < |b| < 90$	84924	1.06 ± 0.02	1.0190 ± 0.0005	28.11 ± 0.03
3.5	$|b| > 35$	103709	1.20 ± 0.01	0.8992 ± 0.0010	8.92 ± 0.04
3.5	$25 < |b| < 30$	12541	1.22 ± 0.02	0.9406 ± 0.0023	9.56 ± 0.09
3.5	$30 < |b| < 35$	14279	1.15 ± 0.02	0.9116 ± 0.0023	10.28 ± 0.08
3.5	$35 < |b| < 40$	13965	0.94 ± 0.02	0.8751 ± 0.0026	11.04 ± 0.08
3.5	$40 < |b| < 45$	13093	0.97 ± 0.02	0.8690 ± 0.0029	10.58 ± 0.07
3.5	$45 < |b| < 90$	75366	1.06 ± 0.01	0.8672 ± 0.0013	9.33 ± 0.03

Note. — These results are derived with the ZL coefficient a_i fixed to the value determined in the $|b| > 35°$ region, i.e., 1.0079 ± 0.0001, 1.0447 ± 0.0002, and 1.1531 ± 0.0003 at 1.25, 2.2, and 3.5 μm, respectively. Error associated with each parameter represents the statistical uncertainty determined by the fitting.

Due to the difficulty in evaluating the ZL component at 4.9 μm, b-dependence of each parameter is investigated in the other three bands, 1.25, 2.2, and 3.5 μm. In this analysis, the parameter a_i is fixed to the all-sky value ($|b| > 35°$) in each band to reduce the deviation caused by the brightest ZL component. In five different Galactic latitude regions, i.e., $25° < |b| < 30°$, $30° < |b| < 35°$, $35° < |b| < 40°$, $40° < |b| < 45°$, and $45° < |b| < 90°$, the χ^2 minimum analysis is implemented. Owing to the faintness of the DGL component in the higher Galactic latitudes, the wider field ($45° < |b| < 90°$) is analyzed.

The parameters b_i, c_i, and d_i determined in each region are listed in Table 3.7. At 1.25 and 2.2 μm, the intensity ratios of near-IR DGL to 100 μm emission $\nu_i b_i$ increase toward low Galactic latitudes. Similar to $\nu_i b_i$, the ISL parameter c_i increases toward the low Galactic latitudes. This phenomenon may be caused if faint stars not on the catalog increase toward low Galactic latitudes due to the masking by nearest bright sources and/or the spatial distribution of the intensity of bright and faint stars changes in different regions.

In each band, the parameters $\nu_i b_i$ and c_i derived in the $|b| > 35°$ region are not the intermediate value of those at $35° < |b| < 40°$, $40° < |b| < 45°$, and $45° < |b| < 90°$, but larger than these results (Table 3.7). Because the DGL and ISL intensity is naturally expected to change as a function of Galactic latitude, the parameters $\nu_i b_i$ and c_i might be biased to larger values when analyzing a wide field in Galactic latitude, e.g., $|b| > 35°$. This effect may cause the residual light $\nu_i d_i$ at $|b| > 35°$ slightly smaller than those obtained in

the divided regions. The derived b-dependence of the intensity ratios of DGL to $100\,\mu$m emission is used for scientific discussion in Chapter 4.

In the present all-sky analysis, it is capable of investigating the isotropy of the residual light. Figure 3.14 and 3.15 illustrate $I_i(\mathrm{Obs}) - I_i(\mathrm{ZL}) - I_i(\mathrm{ISL}) - I_i(\mathrm{DGL})$ as functions of Galactic (b) and ecliptic latitude (β), respectively, with the derived parameters d_i. In general, the b-dependence traces the accuracy of the ISL or DGL evaluation since their intensities are also functions of b. On the other hands, the β-dependence is expected to measure the accuracy of the ZL model.

As shown in Figure 3.14, the residual light in each band tends to increase toward low-b regions. The phenomenon might stem from the contribution of stars with no entry in the 2MASS PSC or AllWISE catalog, possibly because they were masked by their nearest bright sources. According to the Explanatory Supplement to the 2MASS All-Sky Data Release and Extended Mission Products (Cutri et al. 2003), masking around bright stars can filter faint sources from the detection process. Although the masked area in the all-sky averages to 0.25% and 0.43% at 1.25 and 2.2 μm, respectively, the fraction of such regions tends to increase toward low-b regions as the number density of bright sources increases. In addition, 2MASS compensated for saturation caused by bright stars by fitting the unsaturated wings of their intensity profiles. This suggests that the 2MASS PSC could have missed the faint stars. It can be applied to the AllWISE catalog that adopts the detection strategy similar to 2MASS PSC.

The simply modeled ISL term, $I_i(\mathrm{ISL}) = c_i I_i(\mathrm{DISL})$, may also contribute to the latitude dependence of the residual light. If the spatial distribution of intensity as a function of b differs between $I_i(\mathrm{DISL})$ and the ISL of stars fainter than the detection limits of 2MASS PSC or AllWISE, the model assumption is not strictly valid.

In the region of $b \gtrsim 60°$ at 3.5 and 4.9 μm, the residual light shows the inverse behavior: it increases toward the north Galactic pole (NGP) region (Figure 3.14). To investigate this phenomenon, $I_i(\mathrm{Obs}) - I_i(\mathrm{ZL})$ and $I_i(\mathrm{ISL}) + I_i(\mathrm{DGL})$ are plotted with the residual light in Figure 3.16. Reasonably, the modeled Galactic components $I_i(\mathrm{ISL}) + I_i(\mathrm{DGL})$ increase toward the low-b regions. In contrast, $I_i(\mathrm{Obs}) - I_i(\mathrm{ZL})$ shows the same feature as the residual light in the $b \gtrsim 60°$ region, indicating that the trend is caused by $I_i(\mathrm{ZL})$. The fact that such a feature is larger at 4.9 μm than at 3.5 μm is then reasonable because of the stronger ZL component at 4.9 μm. However, the reason why such a feature is seen only at $b \gtrsim 60°$ is unclear. For one thing, Kelsall et al. (1998) pointed out that the intensity differences between the different ZL models are largest in the NGP region. Such a difficulty in the modeling of ZL near the NGP region may be related to the trend at $b \gtrsim 60°$.

As a function of β, the turbulence of the residual light is greater near the ecliptic plane

at 1.25 and 2.2 μm (Figure 3.15). Cambrésy et al. (2001), who similarly subtracted the ZL using the Kelsall model, reported the same trend. These results indicate the difficulty in using the DIRBE ZL model near the ecliptic plane, where the distribution of the IPD dust including the asteroidal dust bands and the circumsolar ring becomes complex. The residual light is relatively constant at 3.5 μm, while it is systematically larger toward the low-β region at 4.9 μm (Figure 3.15). This indicates the difficulty of modeling of ZL at 4.9 μm, where the ZL intensity is much stronger.

Based on the regional variation of the residual light, its isotropy is estimated. Considering only the "Regional variation" of d_i estimated from the longitudinal variation (Table 3.4), the deviations from isotropy are less than $\pm 10\%$, $\pm 5\%$, $\pm 30\%$ of the determined d_i at 1.25, 2.2, and 3.5 μm, respectively. These anisotropies are consistent with the variation of the residual light as functions of b and β (Figure 3.14, 3.15). This suggests that the residual light is isotropic within these values. Isotropy of the residual light at 4.9 μm is not discussed due to the large variation.
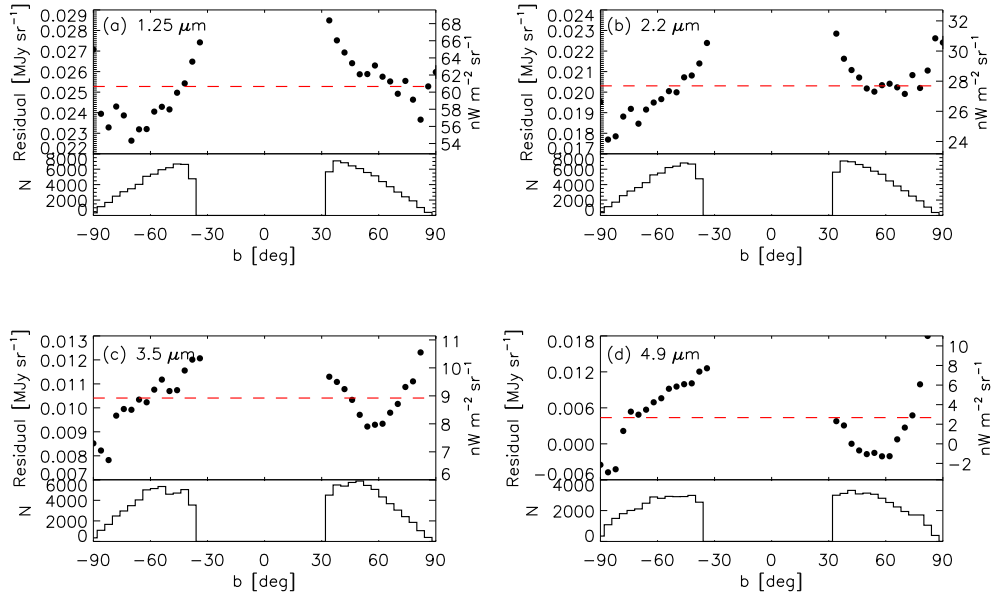
Figure 3.14 Galactic latitude-dependence of residual emission at 1.25 (a), 2.2 (b), 3.5 (c), and 4.9 μm (d). The upper part of each panel illustrates $I_i(\text{Obs}) - I_i(\text{ZL}) - I_i(\text{ISL}) - I_i(\text{DGL})$ derived in $|b| > 35°$ at 1.25, 2.2, 3.5 μm, and $|b| > 35°$, $|\beta| > 20°$ at 4.9 μm with filled circles indicating the weighted-mean values of the points within arbitrary x-axis bins. Horizontal red dashed lines represent the determined parameters d_i in each band (Table 3.4). The lower part represents a histogram of the data points within the x-axis bins.
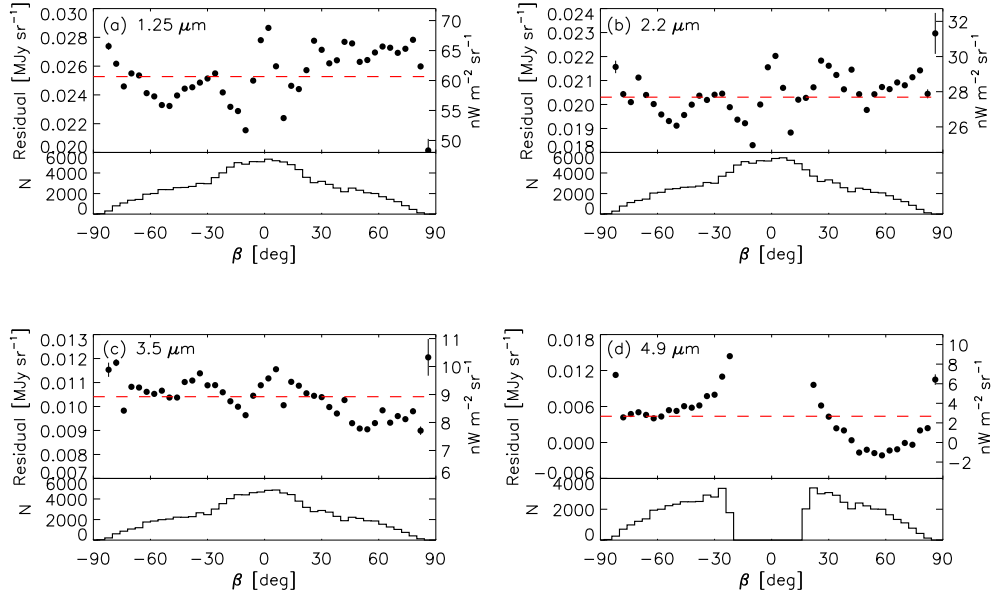
Figure 3.15 Same as Figure 3.14, but as a function of ecliptic latitude.
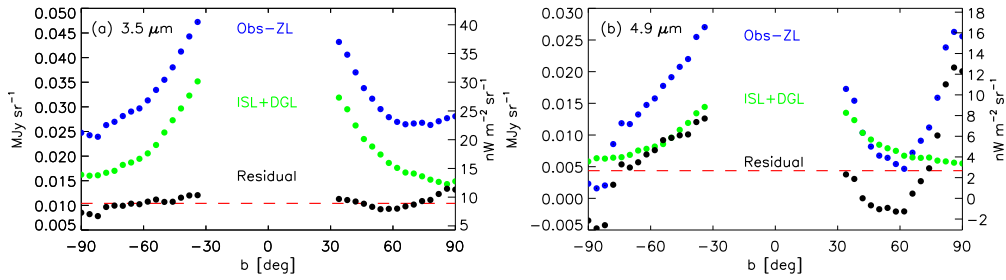
Figure 3.16 Galactic latitude-dependence of residual emissions $I_i(\mathrm{Obs}) - I_i(\mathrm{ZL}) - I_i(\mathrm{ISL}) - I_i(\mathrm{DGL})$ (black circles), $I_i(\mathrm{Obs}) - I_i(\mathrm{ZL})$ (blue circles), and $I_i(\mathrm{ISL}) + I_i(\mathrm{DGL})$ (green circles) at 3.5 (a) and 4.9 μm (b). Filled black circles denote the same quantities as those in Figure 3.14. Horizontal red dashed lines indicate the determined parameters d_i (Table 3.4).

3.3 Comparison with other observations

3.3.1 Zodiacal light

As shown in Table 3.3, the parameter a_i, the scaling factor of the DIRBE ZL model is determined to be unity within 1% uncertainty at $1.25\,\mu$m. This indicates that the DIRBE ZL model succeeds in reproducing the time variation of the sky brightness in this band. At $2.2\,\mu$m, a_i exceeds unity by approximately 4%. On average, a 4% variation in the DIRBE ZL model corresponds to $\sim 8\,\mathrm{nW\,m^{-2}\,sr^{-1}}$, which is slightly larger than the claimed systematic uncertainty of the model, $6\,\mathrm{nW\,m^{-2}\,sr^{-1}}$. This may suggest that the DIRBE ZL model underestimates the ZL intensity in this band for some reasons. In its development, the DIRBE ZL model sampled the sky every $\sim 5°$ or $\sim 10°$ as a spatial grid to avoid excessive computation for computers ~ 20 years ago.

At 3.5 and $4.9\,\mu$m, a_i is determined to be 10%–15% larger than unity in both bands (Table 3.3), indicating that the DIRBE ZL model underestimates the ZL brightness. This trend has also been reported by Tsumura et al. (2013a) and Matsumoto et al. (2015) in their analysis of the *AKARI* and *IRTS* data, respectively. Same as 1.25 and $2.2\,\mu$m, the incompleteness of the DIRBE ZL model might contribute to such deviations. Though the model revision is beyond the scope of this thesis, there seems room for improving the ZL model.

3.3.2 Integrated starlight

The parameter c_i, the scaling factors of the integrated light calculated from the 2MASS PSC or AllWISE catalog, exceeds unity by 1%–4% at 1.25 and $2.2\,\mu$m (Table 3.3). This excess is thought to originate from the stars fainter than the 2MASS detection limit by assuming these populations have the same spatial distribution as the brighter stars. To estimate the contribution of stars fainter than the 2MASS sensitivity, faint stars detected in UKIRT Infrared Deep Sky Survey (UKIDSS) are used. In the J and K bands, UKIDSS has conducted several deep surveys toward specific regions of the sky (e.g., Large Area Survey) and achieved the higher sensitivity than 2MASS (Lawrence et al. 2007). In the UKIDSS surveys, Deep Extragalactic Survey (DXS) observed four regions covering a few square degrees and achieved the nominal sensitivity of $21.0\,$mag in the K band. Therefore, the DXS source catalogs are suitable for investigating not only galaxies but also Galactic stars to be compared with the 2MASS PSC.

Figure 3.17 and 3.18 compare, respectively, the star counts from the 2MASS PSC with those from UKIDSS DXS in the J and K bands. Star counts expected from a star-counts
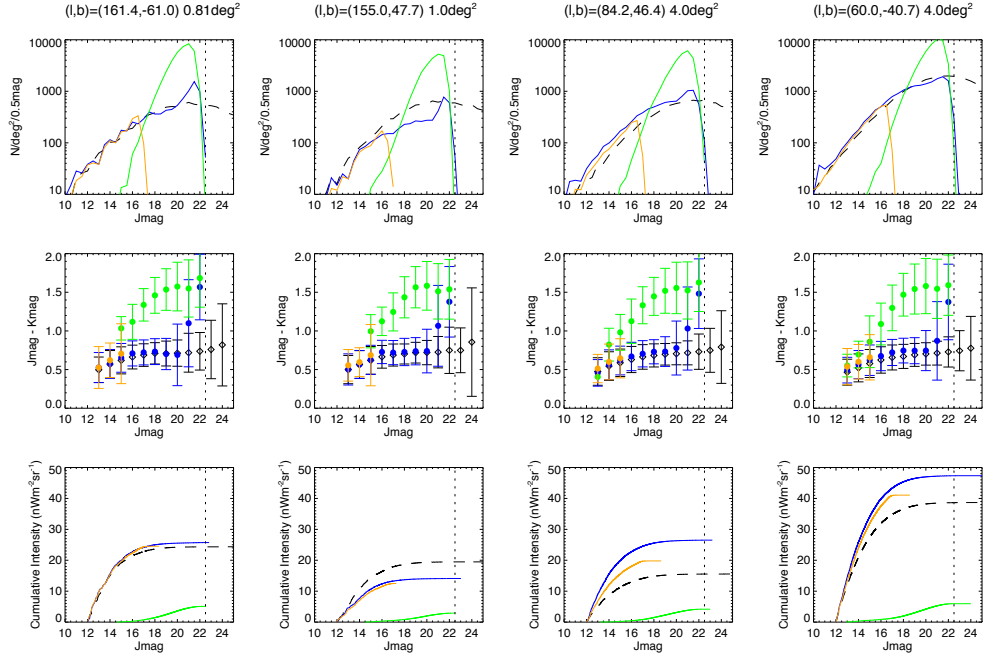
Figure 3.17 Comparison of differential number count (top), $J - K$ color (middle), and cumulative intensity of stars (bottom) as a function of J magnitude in the four DXS fields. In each panel, blue and green curves (symbols) indicate, respectively, stars and galaxies with their possibility of $> 90\%$ in the DXS catalog. Orange and black curves (symbols) represent the star counts from the 2MASS and TRILEGAL, respectively. Vertical dashed line indicates nominal sensitivity limit of the DXS catalog.
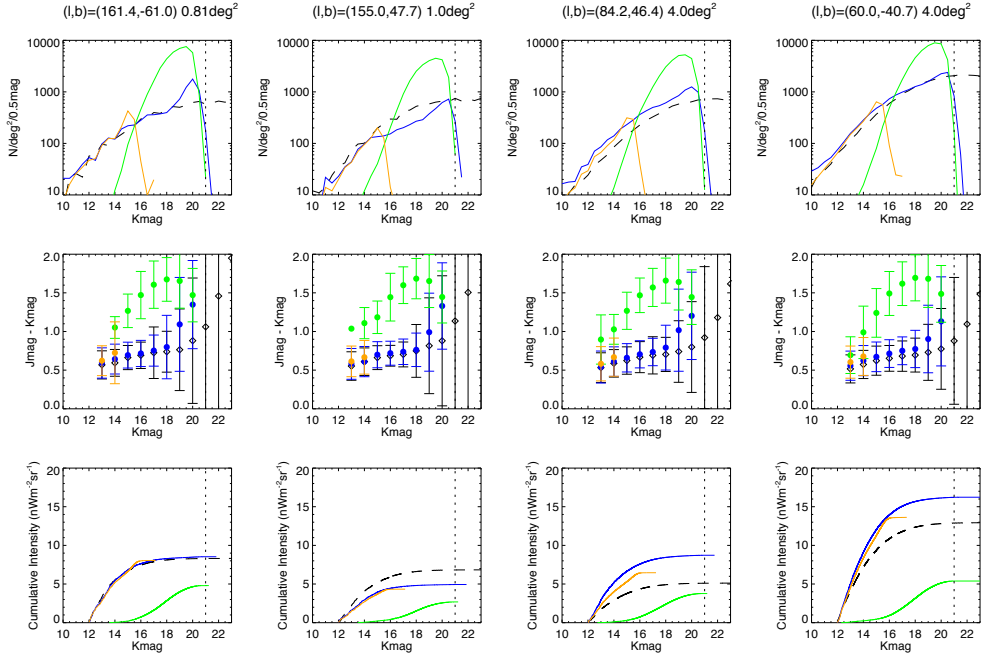
Figure 3.18 Same as Figure 3.17, but for the K band.

model TRILEGAL (Girardi et al. 2005) is also plotted. The UKIDSS differential star counts show a sudden increase around 20 mag in both bands. This trend may be caused by misidentification of stars as galaxies in that faint range. In fact, colors of the stars approach those of galaxies toward the fainter magnitude. Regardless of the possible contamination of galaxies, cumulative intensity is smoothly plotted from brighter to fainter magnitude and the shapes become flat below the detection limit of the DXS catalog. This indicates that stars fainter than ~ 20 mag do not contribute to the cumulative intensity.

The cumulative intensity of stars fainter than the 2MASS detection limit is calculated from the UKIDSS data, to be compared with the 2MASS-derived intensity of faint stars, i.e., $c_i - 1.0$. The results are listed in Table 3.8. The values (4) can be regarded as the missed fraction of the ISL evaluation in the present study. However, the difference is typically by one order of magnitude smaller than the residual emission d_i and is within the regional variation. In conclusion, the faint stellar population does not significantly contribute to the derived residual emission at 1.25 and 2.2 μm.

At 3.5 and 4.9 μm, the parameter c_i is determined to be less than unity (Table 3.3). Taking into account the contributions of stars fainter than the sensitivity limits of AllWISE, the parameter c_i should be more than unity. However, several studies have reported a similar trend in the correlation analysis of the DIRBE data against the ISL of the 2MASS sources

66

Table 3.8 Cumulative intensity of 2MASS and UKIDSS stars

Region (l, b)	$(161.4, -61.0)$	$(155.0, 47.7)$	$(84.2, 46.4)$	$(60.0, -40.7)$
Cumulative Intensity (nW m^{-2} sr^{-1})				
1.25 μm				
(1) 2MASS (5.0–15.8 mag)	76.1	49.8	112.5	207.4
(2) UKIDSS (15.8–20.0 mag)	3.3	1.9	4.0	8.1
(3) $(c_i - 1.0) \times$ (1)	1.5	1.0	2.3	4.1
(4) (2) - (3)	1.8	0.9	1.7	4.0
2.2 μm				
(1) 2MASS (4.0–14.3 mag)	26.6	18.4	32.6	82.3
(2) UKIDSS (14.3–20.0 mag)	2.6	1.6	3.0	6.0
(3) $(c_i - 1.0) \times$ (1)	0.8	0.6	1.0	2.5
(4) (2) - (3)	1.8	1.0	2.0	3.5

Note.—

(1) Cumulative intensity of 2MASS stars brighter than the detection limit.

(2) Cumulative intensity of UKIDSS stars from the 2MASS detection limit to 20 mag.

(3) Cumulative intensity of stars fainter than the 2MASS detection limit, estimated from parameter c_i.

(4) Intensity difference between (2) and (3).

(Cambrésy et al. 2001; Levenson et al. 2007). They reported that the parameter c_i is less than unity by $\sim 10\%$ at 2.2 μm. Cambrésy et al. (2001) attributed this to the different methods of photometric calibration adopted by DIRBE and 2MASS; that is, Sirius was used as a reference for DIRBE (Hauser et al. 1998), while several faint stars were used for 2MASS (Skrutskie et al. 2006) to avoid instrumetal saturation. Similar to the 2MASS calibration strategy, *WISE* was calibrated by several stars fainter than Vega (Wright et al. 2010). Therefore, the small c_i can be attributed to the fact that the photometric calibration difference between DIRBE and *WISE* is more dominant than the contribution of the fainter stars. The very small value of 0.570 ± 0.254 at 4.9 μm may also be contributed by the multicollinearity effect between ZL and ISL due to the intense ZL component and the weak ISL component (Table 3.5).

3.3.3 Diffuse Galactic light

As explained in Chapter 1, the previous DIRBE analysis failed to find the linear correlation between diffuse near-IR light and 100 μm emission due to the poor ISL estimation (Arendt et al. 1998). Though they did not explicitly show the relation between diffuse near-IR and 100 μm emission in the paper, their analysis is reproduced here in the high-b region from the DIRBE Zodi-Subtracted Mission Average (ZSMA) maps and the FSM to
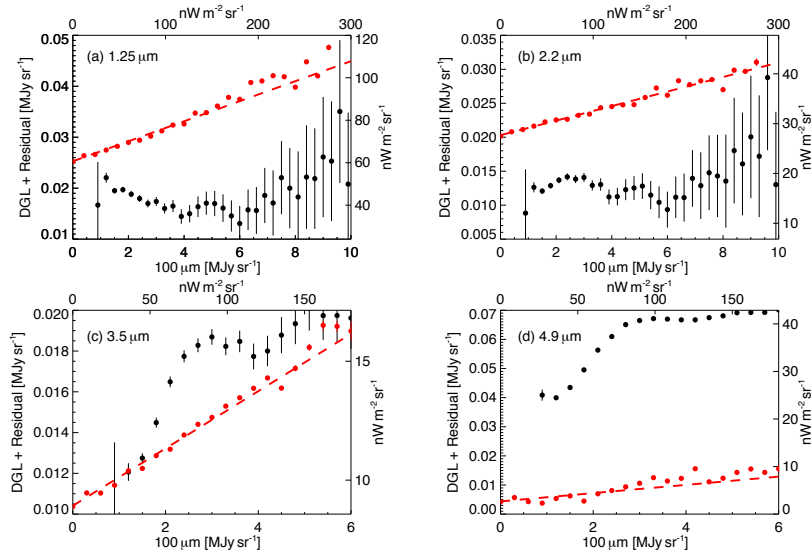
Figure 3.19 Correlation between $100\,\mu$m emission and DGL at 1.25 (a), 2.2 (b), 3.5 (c), and $4.9\,\mu$m (d), derived from present study (red circles) and from reproduction of the previous DIRBE analysis (black circles; Arendt et al. 1998). The reproduced values are derived by subtracting the FSM intensity from the DIRBE ZSMA map.

be compared with the present result.

Figure 3.19 compares the correlations from the reproduction of the previous analysis with those derived in the present study, which is identical to the panels (b) of Figure 3.6, 3.7, 3.8, and 3.9. In the reproduction of the previous analysis, linear correlation does not appear at 1.25 and $2.2\,\mu$m, consistent with non-detection of DGL (Arendt et al. 1998). At 3.5 and $4.9\,\mu$m, though the linear correlation appears in the region of low $100\,\mu$m intensity ($\lesssim 4\,\mathrm{MJy\,sr^{-1}}$), the relation breaks in the higher intensity. Since there is no clear reason for this trend, they are supposedly caused by the incompleteness in the ISL evaluation. It is also clear that the diffuse isotropic light corresponding to the y-intercept of each panel does not determined if the ISL and DGL are not correctly evaluated.

Other studies using 2MASS for the ISL evaluation have not evaluated the DGL contribution to the diffuse sky brightness (e.g., Gorjian et al. 2000, Cambrésy et al. 2001, Levenson et al. 2007). Their analyses have concentrated to the high-Galactic latitude small region, where the DGL is difficult to extract due to low intensity contrast of the $100\,\mu$m intensity.

In Figure 3.20, the present DGL results are compared with other observations. The present results are consistent with observations with *CIBER* (Arai et al. 2015) and *AKARI* (Tsumura et al. 2013b). In the previous DIRBE analysis, Arendt et al. (1998) derived
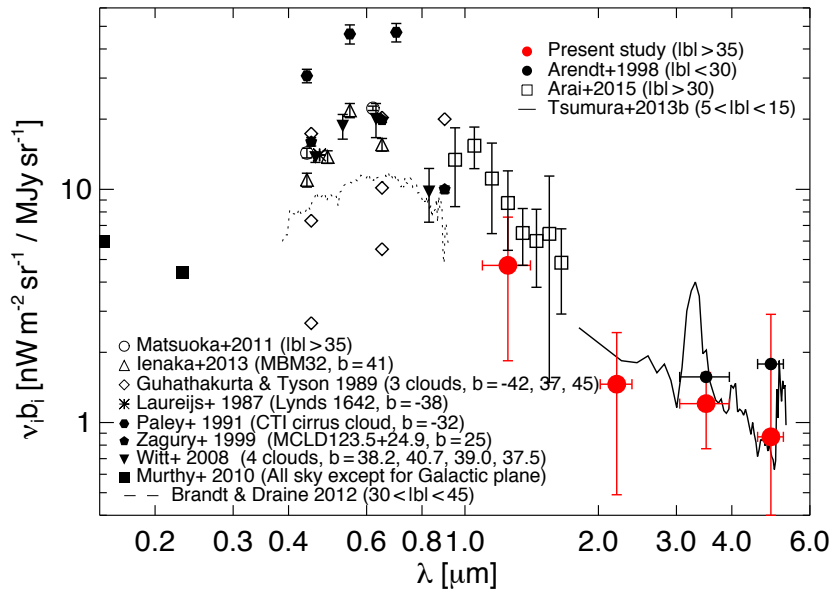
Figure 3.20 Observed results of intensity ratios of DGL to $100\,\mu$m emission $\nu_i b_i$ from UV to near-IR. Present results are plotted as filled red circles with horizontal error bars denoting the DIRBE bandwidth. References of the individual symbols are indicated in the upper right and lower left. The result from Brandt & Draine (2012) is scaled by factor 2.1.

slightly higher values than the present result at 3.5 and $4.9\,\mu$m probably because the analyzed regions were limited to low-b region ($|b| < 30°$) including Galactic plane. Most of the optical results come from observations of various clouds, but they show large difference up to about one order of magnitude. Ienaka et al. (2013) investigated optical depth dependence of the ratios and attributed the difference to its variation among the clouds. See discussion of Ienaka et al. (2013) for detail. Implications about the interstellar dust derived from the near-IR DGL are presented in Chapter 4 in comparison with models of the scattered light and thermal emission.

3.3.4   Diffuse isotropic light

Prior to comparison with other studies, additional uncertainties of the diffuse isotropic light d_i are estimated. Such uncertainties stem from the absolute gain of DIRBE, faint galaxies, and the DIRBE ZL model.

Hauser et al. (1998) reported an uncertainty of 3.1% in the absolute gain of the DIRBE at 1.25, 2.2, and $3.5\,\mu$m, and 3.0% at $4.9\,\mu$m. These uncertainties correspond to percentages of the derived parameters d_i. The values are listed in the row "Gain" in Table 3.4.

The 2MASS PSC may contain faint galaxies recognized as point sources in the detection process. Wright (2001) estimated that galaxies with $K_s < 14.3\,$mag contribute around 0.12 and $0.14\,\mathrm{nW\,m^{-2}\,sr^{-1}}$ to the diffuse isotropic light at 1.25 and $2.2\,\mu$m, respectively. The AllWISE catalog may also contain such faint galaxies. Levenson et al. (2007) estimated the contribution of such galaxies at $3.5\,\mu$m of $0.04\,\mathrm{nW\,m^{-2}\,sr^{-1}}$, which corresponds to galaxies of $K_s < 14.3\,$mag in the 2MASS PSC. Assuming this value is of the same order as the AllWISE sources, it is adopted to the uncertainty of faint galaxies at $3.5\,\mu$m. Assuming the spectra of galaxies do not drastically change between 3.5 and $4.9\,\mu$m, the same value is set at $4.9\,\mu$m. These uncertainties are listed in the "Galaxies" row in Table 3.4.

As described in Kelsall et al. (1998), the uncertainty of the DIRBE ZL model is estimated as the intensity difference between the two ZL models at NGP where the discrepancy is reported to be the largest. These two models were equally good in reproducing the observed seasonal variations of the ZL. These uncertainties are 15, 6, 2.1, and $5.9\,\mathrm{nW\,m^{-2}\,sr^{-1}}$ at 1.25, 2.2, 3.5, and $4.9\,\mu$m, respectively. These are listed in the row "ZL model" in Table 3.4.

The quadrature sum of the uncertainties is presented in the row "Quadrature sum" in Table 3.4. The uncertainties associated with the regional variation and the DIRBE ZL model dominate over the other uncertainties.

In Figure 3.21, the resultant diffuse isotropic light is compared with those of previous

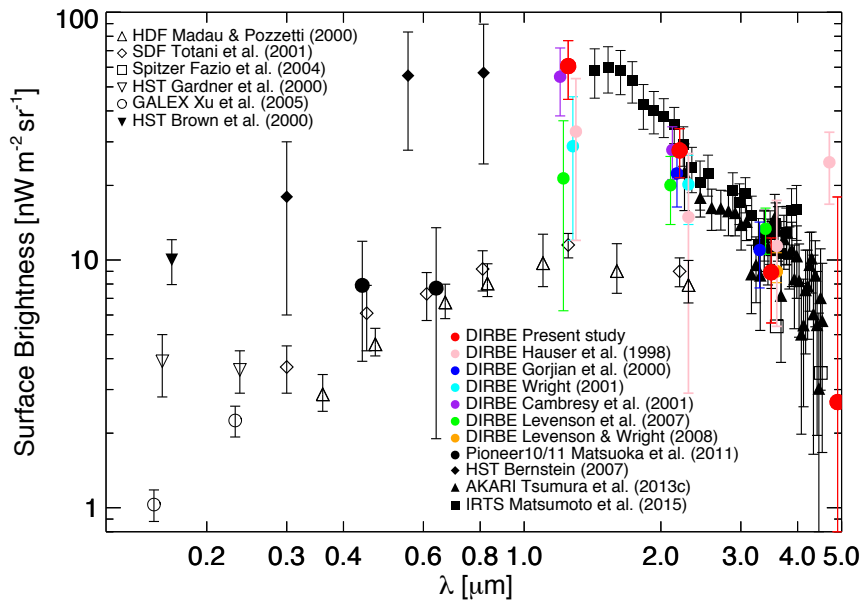Figure 3.21 Observed intensity of diffuse isotropic light and IGL from UV to near-IR. Present results are indicated by red circles. Results of diffuse residual emission are indicated by filled symbols, while those of the IGL observations are by open symbols. References of the individual symbols are written in the lower right and upper left. For clarity, some results are shifted a little from their exact wavelengths.

studies. At 1.25 and $2.2\,\mu m$, the present results are several times larger than the IGL observations (Madau & Pozzetti 2000; Totani et al. 2001) and the same level as earlier measurements (Cambrésy et al. 2001; Matsumoto et al. 2015). Compared with the diffuse isotropic light at 1.25 and $2.2\,\mu m$, the present result at $3.5\,\mu m$ is small, marginally consistent with the IGL level.

Using the FSM, Hauser et al. (1998) derived the residual light at high Galactic and ecliptic latitudes, as a first result of the DIRBE analysis. They reported the residual light at 1.25 and $2.2\,\mu m$ of 33.0 ± 21 and $14.9 \pm 12\,\mathrm{nW\,m^{-2}\,sr^{-1}}$, respectively (pink circles in Figure 3.21), which are smaller than the present results. This discrepancy can be explained by the following two things related to the ISL evaluation. At first, in converting the magnitudes of the sources into DIRBE flux densities, the present study adopts the zero magnitude of 1467 and $540\,\mathrm{Jy}$ at 1.25 and $2.2\,\mu m$, respectively, but Hauser et al. (1998) used higher one, i.e., 1547 and $612.3\,\mathrm{Jy}$ at 1.25 and $2.2\,\mu m$, respectively (COBE/DIRBE Explanatory Supplement 1998). The zero magnitudes used in the present analysis is derived by Levenson et al. (2007), who correlated the intensity of the 2MASS-derived ISL with that of the DIRBE and corrected the zero magnitude to fit the photometric scale of the 2MASS to that of the DIRBE. Therefore, the zero magnitudes adopted in the present study are suitable to estimate the ISL contribution in the DIRBE data. Next, Wright & Reese (2000) suggested that the Wainscoat et al.'s (1992) star-counts model, which is the basis of the FSM, overestimates the counts by $\sim 10\%$ in the $6 < K < 10$ range at high Galactic latitudes, compared with the 2MASS. This is within the 10%–15% uncertainty of the FSM, estimated in Arendt et al. (1998). Considering these differences associated with the ISL estimation, the ISL intensity in Hauser et al. (1998) can be higher than that in the present study by $\sim 15\%$ and $\sim 20\%$ at 1.25 and $2.2\,\mu m$, respectively. These percentages correspond to ~ 26 and $\sim 13\,\mathrm{nW\,m^{-2}\,sr^{-1}}$ at 1.25 and $2.2\,\mu m$, respectively, assuming the ISL intensity derived in the present study (Table 3.5). This overestimation of the ISL in Hauser et al. (1998) well explains the intensity differences between Hauser et al. (1998) and the present study at both 1.25 and $2.2\,\mu m$.

Using the DIRBE data, Cambrésy et al. (2001) derived the diffuse isotropic light at 1.25 and $2.2\,\mu m$ (purple circles in Figure 3.21) by subtracting the Galactic stars with 2MASS and the ZL with the DIRBE ZL model, which were similar to the present study except for the DGL evaluation. These authors targeted regions with low intensity of the dust emission (DIRBE $240\,\mu m$ brightness $I_{240} < 3\,\mathrm{MJy\,sr^{-1}}$). In such regions, the expected DGL brightness at 1.25 and $2.2\,\mu m$ is $\lesssim 7$ and $\lesssim 2\,\mathrm{nW\,m^{-2}\,sr^{-1}}$, respectively, assuming the intensity ratios of the DGL to the $100\,\mu m$ emission determined in the present study and the conversion factor between the 100 and $240\,\mu m$ intensities, 1.297 (Arendt et al. 1998).

In addition, the I_{100} histograms (Figure 3.6 and 3.7) show that regions of lower $100\,\mu$m intensity dominate in the sky. Therefore, the diffuse isotropic light derived in this study is reasonably consistent with that obtained by Cambrésy et al. (2001), despite the lack of any quantitative DGL evaluation, though they noticed fluctuations in residuals as a function of ecliptic latitude, which would be attributed to the DGL component at $1.25\,\mu$m.

In the measurement of diffuse near-IR emission, the ZL evaluation is controversial, as multiple ZL models are available. For instance, Gorjian et al. (2000), Wright (2001), and Levenson et al. (2007) used the Wright model (Wright 1998), whereas Cambrésy et al. (2001) and the present study adopted the DIRBE ZL model (Kelsall et al. 1998). As noted by Levenson et al. (2007), the ZL intensity at the ecliptic pole at 1.25 and $2.2\,\mu$m is ~ 22 and $\sim 5\,\mathrm{nW\,m^{-2}\,sr^{-1}}$ lower in the DIRBE ZL model than in the Wright model, respectively. Consequently, the difference between the two models tends to be larger at $1.25\,\mu$m than at $2.2\,\mu$m. As shown in Figure 3.21, the diffuse isotropic light obtained with the DIRBE ZL model can be a few times lower than that obtained with the Wright model especially at $1.25\,\mu$m. At $2.2\,\mu$m, the results of both models converge within their uncertainties.

As illustrated in Figure 3.20, the present DGL result at $3.5\,\mu$m in the high Galactic latitudes is comparable to the results obtained at low-Galactic latitudes (Arendt et al. 1998) within the uncertainty. As shown in Figure 3.21, this leads to the same level of the diffuse isotropic light as in the previous studies adopting the DGL result derived by Arendt et al. (1998) at $3.5\,\mu$m (Gorjian et al. 2000). At $4.9\,\mu$m, the residual light is not significantly detected due to large uncertainty associated with the ZL subtraction, same as the previous studies (Hauser et al. 1998; Tsumura et al. 2013c).

Chapter 4

Origin of the Near-Infrared Diffuse Galactic Light

4.1 Constraints on interstellar dust properties

By comparing the observed DGL with model spectra, interstellar dust properties are constrained in high Galactic latitudes. Figure 4.1 shows the observed $\nu_i b_i$ with the models of scattered light and thermal emission. As seen from the figure, scattered light and thermal emission are expected to coexist in the near-IR. Therefore, both models are necessary to constrain dust properties from the near-IR DGL observation.

4.1.1 Models of scattered light and thermal emission

Brandt & Draine (2012), hereafter BD12, estimated spectra of the scattered light assuming a plane-parallel galaxy, based on different dust models of Zubko et al. (2004), hereafter ZDA04, and Weingertner & Draine (2001), hereafter WD01. As summarized in Chapter 23 of Draine (2011), both models are composed of graphite, silicate, and PAH. The major difference between the two models is size distributions of the grains. The half-mass radius, $a_{0.5}$ (50% of the total mass in grains with the radius $a > a_{0.5}$), is 0.06 and 0.07 μm for the graphite and silicate grains, respectively, in ZDA04, but is 0.12 μm for both grains in WD01, leading to a much greater mass in $a \gtrsim 0.2 \, \mu$m in WD01. Draine (2011) suggests that the WD01 model better reproduces the observed extinction curve from UV to near-IR wavelengths (Fitzpatrick 1999).

For the ISRF model, BD12 adopted de-reddening correction of the local ISRF derived by MMP83 (section 1.1.2), and stellar population synthesis model of Bruzual & Charlot (2003), hereafter BC03. BD12 adopted the BC03 model with solar metallicity and a star
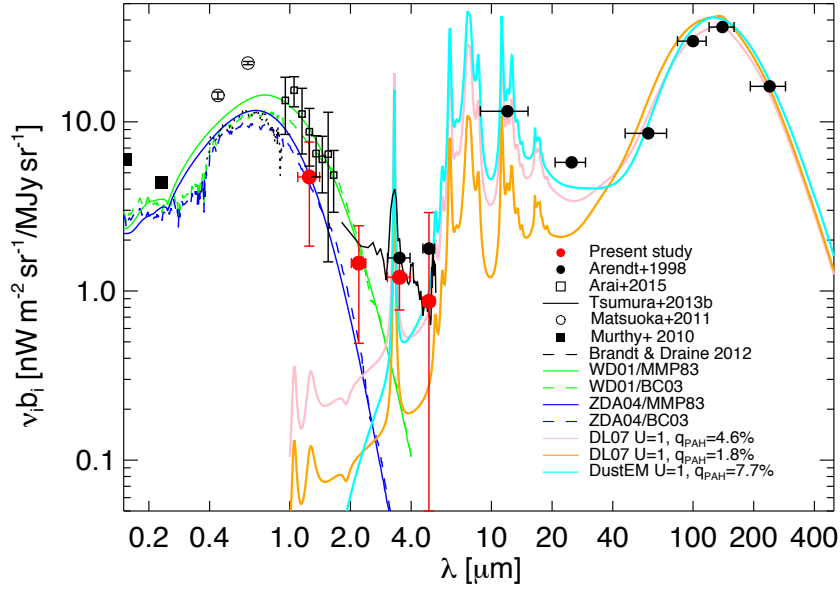
Figure 4.1 Intensity of scattered light and thermal emission from UV to far-IR, normalized by $100\,\mu$m emission. Observed results are indicated by the same symbols as those in Figure 3.20. Model spectra of scattered light for WD01/MMP83, WD01/BC03, ZDA04/MMP83, and ZDA04/BC03 are indicated by green solid, green dashed, blue solid, and blue dashed curves, respectively (BD12). Model spectra of thermal emission for DL07 ($q_{PAH} = 4.6\%$), DL07 ($q_{PAH} = 1.8\%$), and DustEM ($q_{PAH} = 7.7\%$) are indicated by pink, orange, and cyan curves, respectively. The ISRF parameter U is set to $U = 1$ in all models.

formation rate of $\propto \exp(-t/5\,\text{Gyr})$, where t denotes the timescale in units of Gyr. In Figure 4.1, These model spectra are indicated by blue solid (ZDA04/MMP83), blue dashed (ZDA04/BC03), green solid (WD01/MMP83), and green dashed (WD01/BC03) curves. In the models, intermediate Galactic latitude of $b = 40°$ is assumed. The model spectra are much more sensitive to the difference in the dust model than that in the ISRF model, except for the 4000 Å break in the BC03 models. This indicates that the difference between the dust models has larger influence on the near-IR DGL.

For the thermal emission models, Draine & Li (2007; hereafter DL07) and Compìegne et al. (2011; hereafter DustEM) are used. They calculated the model spectra as the intensity per hydrogen column density N_H in units of $\text{erg}\,\text{s}^{-1}\,\text{sr}^{-1}\,\text{H}^{-1}$. To convert this quantity to $\nu_i b_i$, the ratio of $100\,\mu\text{m}$ emission to hydrogen column density derived from DIRBE at high-latitude regions ($|b| > 25°$) — $18.6\,\text{nW}\,\text{m}^{-2}\,\text{sr}^{-1}/10^{20}\,\text{cm}^{-2}$ (Arendt et al. 1998) is used.

The model spectra are determined by two parameters U and q_PAH which are scaling factor of the local ISRF (MMP83) and mass fraction of the very small grains including PAH to the total dust, respectively. As shown in Figure 4.1, the models with $U = 1$ well reproduces the far-IR spectra observed by DIRBE (Arendt et al. 1998). Therefore, ISRF is fixed to $U = 1$. The parameter q_PAH influences the near to mid-IR emission. In Figure 4.1, the model spectra with DL07 ($q_\text{PAH} = 4.6\%$), DL07 ($q_\text{PAH} = 1.8\%$), and DustEM ($q_\text{PAH} = 7.7\%$) are indicated by pink, orange, and cyan curves, respectively. In these models, most locations of the PAH features are identical.

4.1.2 Mass fraction of very small grain and polycyclic aromatic hydrocarbon

To constrain the dust properties in high-b diffuse ISM, the present results in the near-IR are compared with the models of scattered light and thermal emission. In Figure 4.2, the observed near-IR DGL are shown with model spectra of the two scattered light (ZDA04/MMP83; WD01/MMP83) and three thermal emission (DL07 $q_\text{PAH} = 4.6\%$; DL07 $q_\text{PAH} = 1.8\%$; DustEM $q_\text{PAH} = 7.7\%$). At $3.5\,\mu\text{m}$, the DIRBE band includes the strong PAH feature of the C-H stretching mode at $3.3\,\mu\text{m}$. Therefore, the thermal emission dominantly contributes to the DGL in that band. By comparing the three thermal emission models with the present result at $3.5\,\mu\text{m}$, PAH parameter is constrained to $2\% \lesssim q_\text{PAH} \lesssim 8\%$. This mass fraction means that the size distribution of interstellar dust cannot be represented by single power law such as MRN. This result also suggests the presence of PAH in high-b region, though the previous studies with *AKARI* (Tsumura et al. 2013b) and *IRTS* (Mat-

sumoto et al. 2015) were not able to detect the PAH feature in high-b region possibly due to the spectroscopic observations with low signal-to-noise ratio. The IR emission colors obtained by the *Spitzer*/IRAC (Infrared Array Camera) observation toward several regions of lower Galactic latitudes (Flagey et al. 2006) are closer to that of the DL07 model with $q_{\mathrm{PAH}} = 4.6\%$, which are consistent with the present results. This may imply that the mass fraction of PAH is not significantly different between low and high-b regions.

At $4.9\,\mu$m, the result of Arendt et al. (1998) is two times higher than that of the model spectra (Figure 4.1). Li & Draine (2001) thus suggested an additional opacity of the ultra-small grains to explain this excess. However, such components may not be required by the present result at $4.9\,\mu$m, without taking into account the regional variation.
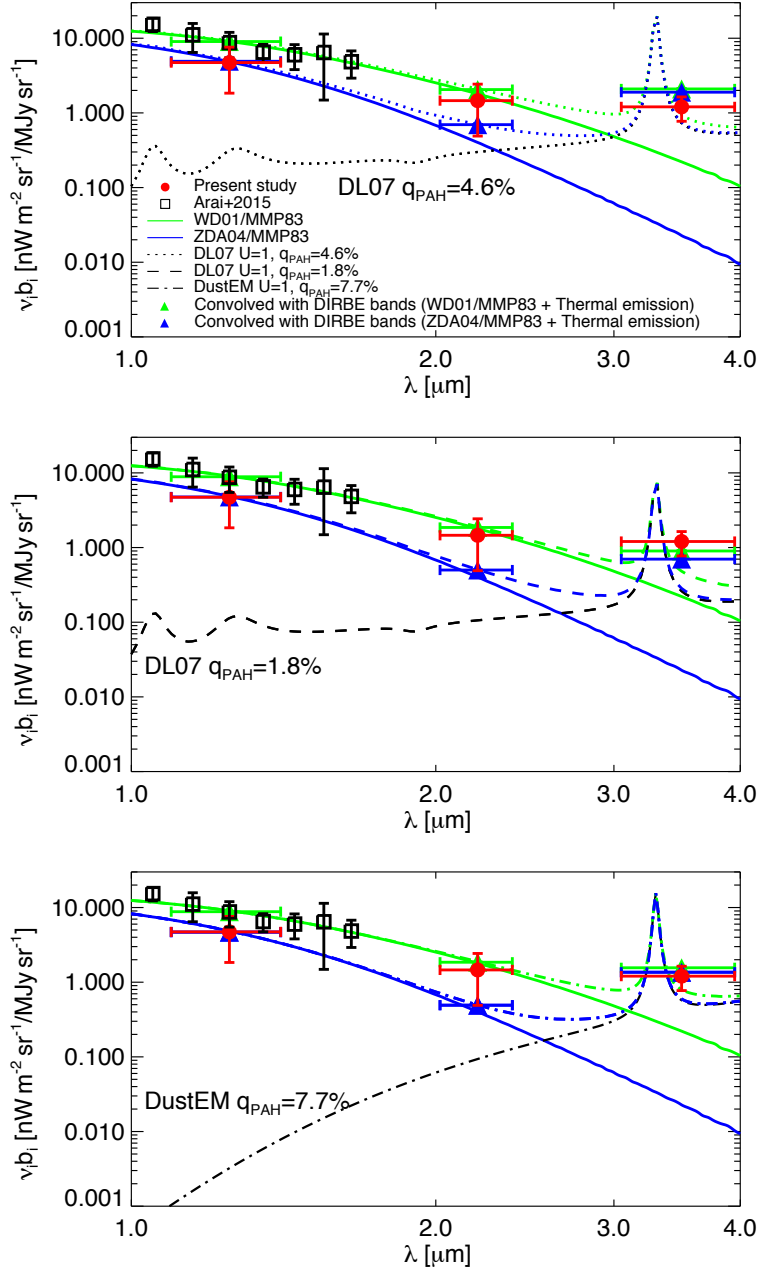
Figure 4.2 Comparison of observed near-IR DGL with model spectra of scattered light and thermal emission. Results from the present study and *CIBER* are represented by red circles and black squares, respectively. Green and blue solid curves represent, respectively, the scattered models assuming WD01/MMP83 and ZDA04/MMP83. Model spectra of thermal emission from DL07 ($q_{\mathrm{PAH}} = 4.6\%$), DL07 ($q_{\mathrm{PAH}} = 1.8\%$), and DustEM ($q_{\mathrm{PAH}} = 7.7\%$) are indicated by dotted, dashed, and dot-dashed curves, respectively. In each panel, the sum of scattered light and thermal emission models are indicated by green and blue curves with triangles denoting the value convolved with each DIRBE band.

4.1.3 Near-infrared albedo of interstellar dust

Now that the PAH parameter is constrained to $2\% \lesssim q_{\text{PAH}} \lesssim 8\%$ in high-b region, the corresponding thermal emission component is subtracted from the observed values at 1.25 and $2.2\,\mu\text{m}$ to be compared with the scattered light models (Figure 4.2). Figure 4.3 illustrates the relation between the scattered light component at 1.25 and $2.2\,\mu\text{m}$, which are derived in all high-b ($|b| > 35°$), longitude-divided, and latitude-divided regions. Colors of the scattered light models are represented by blue (ZDA04/MMP83) and green (WD01/MMP83) lines. As clearly seen from the figure, the present results prefer WD01 rather than ZDA04. As shown in Figure 4.2, the *CIBER* observation toward the several small regions in high latitudes also prefers the WD01 prediction (Arai et al. 2015).

The black dashed line in Figure 4.3 represents a best-fit line of the values derived in individual regions. The line shows a steeper gradient than the WD01/MMP83 model, indicating redder spectrum of the scattered light relative to the model prediction. In optically thin regions, color of the scattered light should be determined by that of albedo, extinction cross section, and ISRF (Equation 1.2). Since the extinction cross section is confirmed by observation (e.g., Fitzpatrick 1999) and near-IR ISRF is approximated by the sum of the Planck function (MMP83), the redder scattered light is supposedly caused by redder albedo spectrum. In the WD01 model, albedo ratio between $2.2\,\mu\text{m}$ and $1.25\,\mu\text{m}$ is $\omega_{2.2\,\mu\text{m}}/\omega_{1.25\,\mu\text{m}} \sim 0.75$. Since the observed ratio of the scattered light is by a factor of 1.3 larger than that of WD01 (Figure 4.3), the albedo ratio results in $0.75 \times 1.3 \sim 1.0$. Therefore, the albedo spectrum is expected to be flat from 1.25 to $2.2\,\mu\text{m}$ in the high latitudes.

Figure 4.4 shows optical to near-IR albedo values derived in various clouds or nebulae. By observing the Thumbprint nebula, Lehtinen & Mattila (1996) derived near-IR albedo of $0.57 < \omega_{1.25\,\mu\text{m}} < 0.80$ and $0.46 < \omega_{2.2\,\mu\text{m}} < 0.76$. As shown in Figure 4.4, these albedo values are higher than that of WD01 and show the flatter spectrum from 1.25 to $2.2\,\mu\text{m}$, consistent with the above discussion. To explain the high value and flat spectrum of near-IR albedo, they suggested the presence of large grain population up to size of $\sim 1\,\mu\text{m}$. Therefore, the flat albedo spectrum expected from the present study may imply the presence of large grains in the high-latitude diffuse ISM. Origin of the large grains is discussed in the last section of this chapter.
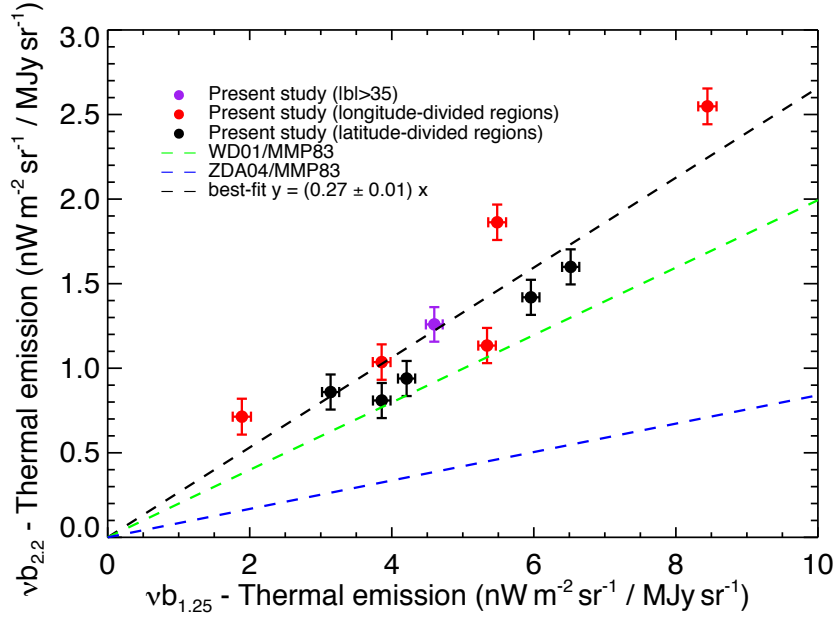
Figure 4.3 Relation between scattered light component at $1.25\,\mu$m (x-axis) and $2.2\,\mu$m (y-axis). The scattered light components are derived by subtracting the thermal emission models from the observed results in $|b| > 35°$ (purple circle), in longitude-divided fields except for the minus value (red circles), and in latitude-divided fields (black circles). Error bars represent quadrature sum of statistical uncertainty and difference of the thermal emission models. Green and blue curves represent, respectively, colors of scattered light in the WD01/MMP83 and ZDA04/MMP83 models. Black dashed line indicates value fitted to the observed results.
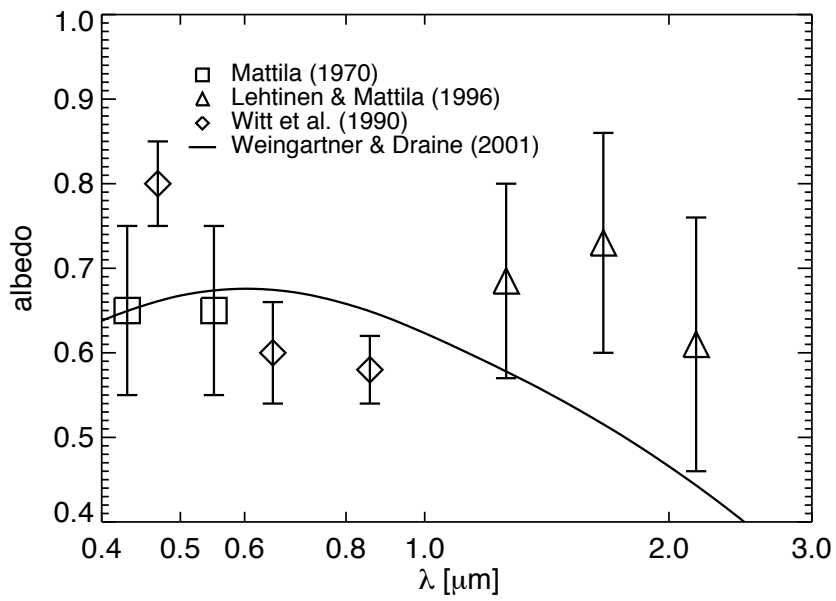
Figure 4.4 Optical to near-IR albedo of interstellar dust, derived from Mattila (1970; squares), Lehtinen & Mattila (1996; triangles), Witt et al. (1990; diamonds), and WD01 model with $R_V = 3.1$.

4.2 Latitude dependence of the diffuse Galactic light

As a result of the decomposition analysis, b-dependence of the intensity ratio of the DGL to $100\,\mu$m emission is found (Table 3.7). This trend is expected from forward scattering of the interstellar dust. Here, the interstellar dust property is investigated from the observed b-dependence.

4.2.1 Derivation of scattering asymmetry factor

As an initial investigation, the b-dependence of the DGL is compared with the previous scattered light model created by Jura (1979; hereafter J79). Figure 4.5 illustrates the derived parameters $\nu_i b_i$ in each band as a function of b, which are taken from Table 3.7.

Adopting the HG41 phase function (Equation 1.5) for interstellar scattering, J79 numerically calculated the scattered light intensity I_{sca} toward the region of optical depth τ and Galactic latitude $|b|$, illuminated by an infinite homogeneous disk in the Galactic plane (Equation 1.7). Bernstein et al. (2002) practically rewrote the intensity I_{sca} as

$$I_{\mathrm{sca}} = I_{\mathrm{ISRF}}\,\omega\,\tau\left(1 - 1.1g\sqrt{\sin|b|}\right), \tag{4.1}$$

where I_{ISRF}, ω, and g denote the ISRF intensity in the solar neighborhood, grain albedo, and scattering asymmetry factor, respectively. As explained in Chapter 1, the g-factor should trace the grain size of interstellar dust. In Equation (4.1), the parameters ω and g (i.e., the interstellar dust properties) are assumed to be independent of Galactic latitude.

As a solution of simple radiative transfer of starlight and scattered light through a dusty slab (see Appendix B.1), Ienaka et al. (2013) expressed the intensity of far-IR emission I_{FIR} as

$$I_{\mathrm{FIR}} \propto I_{\mathrm{ISRF}}\left[1 - \exp\{-(1-\omega)\tau\}\right]. \tag{4.2}$$

As shown in Figure 11 of BD12, the optical depth in the V band is less than ~ 0.2 in most of the high Galactic latitudes $|b| > 20°$, assuming $R_V = 3.1$ Milky Way dust. In the near-IR high-b region, I_{FIR} can be approximated as

$$I_{\mathrm{FIR}} \propto I_{\mathrm{ISRF}}(1-\omega)\tau. \tag{4.3}$$

From Equation (4.1) and (4.3), the intensity ratio of the scattered light to far-IR emission is modeled as

$$I_{\mathrm{sca}}/I_{\mathrm{FIR}} \propto \frac{\omega}{1-\omega}\left(1 - 1.1g\sqrt{\sin|b|}\right). \tag{4.4}$$

According to this formula, in case of fairly isotropic scattering ($g = 0$) the intensity ratio $I_{\mathrm{sca}}/I_{\mathrm{FIR}}$ is insensitive to Galactic latitude. Conversely, the value $I_{\mathrm{sca}}/I_{\mathrm{FIR}}$ increases toward low latitudes in case of forward scattering ($0 < g \leq 1$).
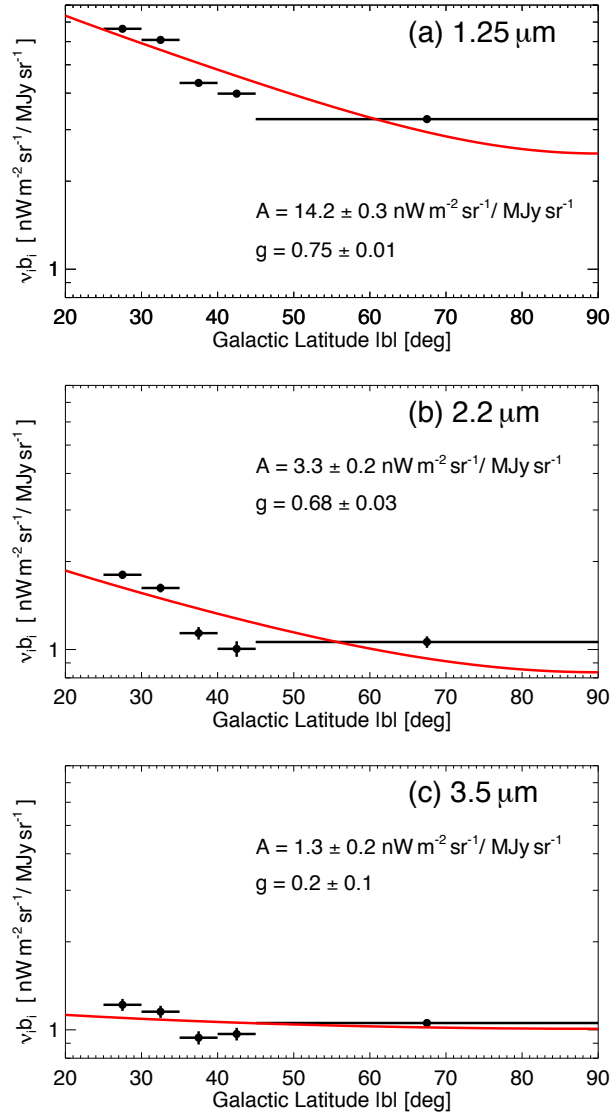
Figure 4.5 Intensity ratios of the near-IR DGL to $100\,\mu$m emission as a function of Galactic latitude $|b|$. Panels (a), (b), and (c) represent the results at 1.25, 2.2, and 3.5 μm, respectively. Filled circle indicates the value $\nu_i b_i$ determined at each field with horizontal error bar denoting the Galactic latitude range of the analyzed field (Table 3.7). In each panel, red curve represents the modeled intensity ratio of the scattered light (Jura 1979) to far-IR emission (Ienaka et al. 2013) in a form of $A\left(1 - 1.1g\sqrt{\sin|b|}\right)$, fitted to the derived values. The determined values A and g are also described in each panel.
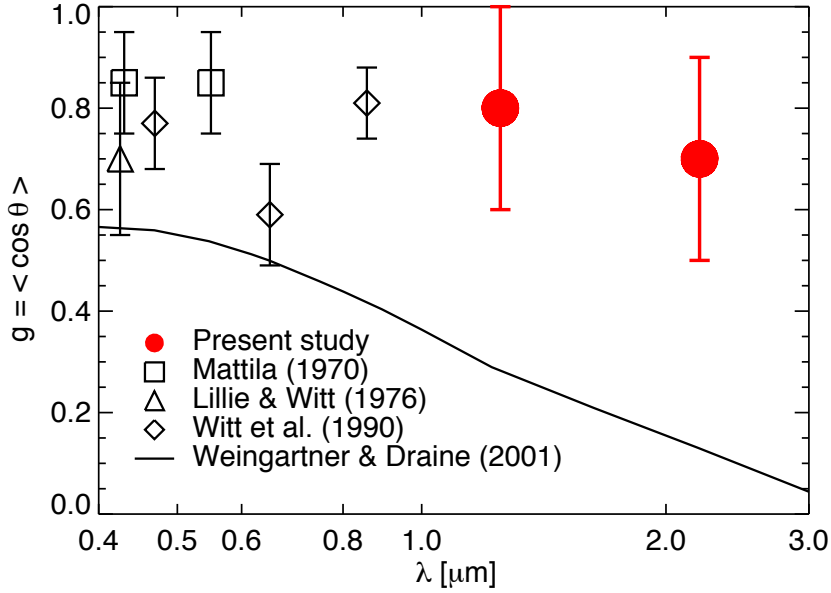
Figure 4.6 Optical to near-IR scattering asymmetry factor $g \equiv \langle \cos \theta \rangle$. The present results at 1.25 and 2.2 μm are indicated by filled red circles. The triangle, diamonds, and squares denote the results derived from Lillie & Witt (1976), Witt et al. (1990), and Mattila (1970), respectively. Solid curve represents the value expected from the WD01 model with $R_V = 3.1$ Milky Way dust (Draine 2003b).

To determine the scattering asymmetry factor g in each band, the values $\nu_i b_i$ obtained at the five different Galactic latitude regions (Figure 4.5) are fitted to the following function:

$$\nu_i b_i = A \left(1 - 1.1 g \sqrt{\sin |b|} \right), \tag{4.5}$$

where A and g are the free parameters. The result is indicated by red curve in each panel. According to J79, Equation (4.5) is accurate to better than factor 1.5. This uncertainty in the approximation roughly corresponds to the g-factor variation of 0.2. Considering this variation, the g values are derived as 0.8 ± 0.2 and 0.7 ± 0.2 at 1.25 and 2.2 μm, respectively. These values indicate strong forward scattering by dust grains.

In Figure 4.6, the derived g-factor is compared with the optical results obtained in some clouds (Mattila 1970; Witt et al. 1990) or a general interstellar field (Lillie & Witt 1976). Black solid line indicates the prediction from the WD01 model with $R_V = 3.1$ Milky Way dust (Draine 2003b). The optical results prefer strong forward scattering with $g \gtrsim 0.6$, comparable to the present near-IR values. The trouble is that the near-IR results conflict with prediction of the WD01 dust model. Since the typical grain size is $\sim 0.1 \, \mu$m in the

WD01 model, the g-factor is expected to be less than ~ 0.3 in the near-IR wavelengths where Rayleigh scattering is dominant.

The observed steep b-dependence may be attributed to the following possibility. For one thing, in addition to the scattered light, possible near-IR thermal emission also has b-dependence at 1.25 and 2.2 μm due to the ISRF gradient against b. Though the near-IR thermal emission has not been observed in the diffuse ISM, it has been detected in some reflection nebulae (Sellgren et al. 1992; Sellgren et al. 1996). For another thing, there is room for improving the scattered light model because the previous J79 form did not take into account the dust density gradient in the Milky Way. In addition, Draine (2003b; hereafter D03) reported discrepancy between the analytical HG41 form and the WD01 phase function in the near-IR. To investigate these possibilities, modeling analyses using the DL07 and BD12 models are conducted as follows.

4.2.2 Contribution of near-infrared thermal emission

The DL07 model is adopted to investigate the b-dependence of the near-IR thermal emission. As explained in section 4.1.1, model spectra of the IR emission are determined by the two parameters q_{PAH} and U. An increase of U makes the IR intensity higher in the entire wavelength range and the dust temperature also becomes higher. Therefore, the peak wavelength of the black body radiation shifts to the shorter far-IR wavelength.

The ISRF intensity is expected to be higher toward low-b region as the number of stars increases. Therefore, the intensity ratios of the near-IR to the 100 μm emission $I_{\lambda,\mathrm{em}}/I_{100}$ are investigated as a function of U to estimate the b-dependence. In the calculation, q_{PAH} is assumed to be independent of b and is set to $q_{\mathrm{PAH}} = 4.6\%$, which is consistent with the DGL observation in high-b region (section 4.1).

Figure 4.7 shows the intensity ratios of the near-IR to 100 μm emission $\nu I_{\lambda,\mathrm{em}}/I_{100}$ as a function of the ISRF parameter U. At both 1.25 and 2.2 μm, the ratios decrease as the ISRF intensity is higher. This trend is inverse of the observed b-dependence: the ratios increase toward low-b region where the ISRF is higher. As the ISRF intensity is higher, the peak wavelength of the Planck function is shifted to shorter far-IR wavelength as well as increase of the intensity in all wavelengths. Therefore, the intensity observed in the 100 μm band becomes much higher than that in the near-IR bands (see Figure 13 of DL07). This makes the ratios lower toward high ISRF intensity.

Based on the DIRBE observation, Arendt et al. (1998) showed linear correlation between the 100 μm intensity and hydrogen column density in high-b region ($|b| > 25°$). They derived the ratio of $I_{100}/N_{\mathrm{H}} = 18.6 \pm 0.3\,\mathrm{nW\,m^{-2}\,sr^{-1}}/10^{20}\,\mathrm{cm^{-2}}$. By combining the near-IR DL07
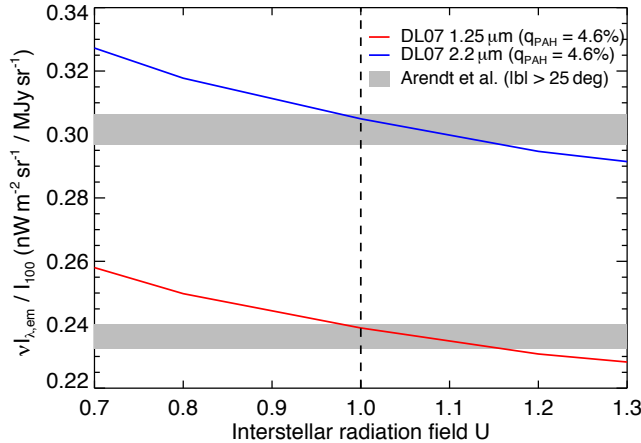
Figure 4.7 Intensity ratios of near-IR to $100\,\mu$m emission $\nu I_{\lambda,\mathrm{em}}/I_{100}$ as a function of the ISRF parameter U (MMP83). A vertical dashed line indicates the local ISRF intensity, $U = 1$. Red and blue curves represent, respectively, the intensity ratios at 1.25 and $2.2\,\mu$m to $100\,\mu$m in the DIRBE bands, which are expected from DL07 with $q_{\mathrm{PAH}} = 4.6\%$. Shaded regions represent the intensity ratios expected from combination of the DL07 value $I_{\lambda,\mathrm{em}}/N_{\mathrm{H}}$ and ratio I_{100}/N_{H} observed toward high-b region ($|b| > 25°$; Arendt et al. 1998).

value $I_{\lambda,\mathrm{em}}/N_{\mathrm{H}}$ with the observed ratio I_{100}/N_{H}, the intensity ratios of the near-IR to $100\,\mu$m emission are also estimated. The results are indicated by shaded regions in Figure 4.7. At both 1.25 and $2.2\,\mu$m, the DL07-derived values intersect the shaded regions at $U \sim 1.0$ which corresponds to the local ISRF. This indicates that the ISRF intensity can be assumed as nearly invariant with $U \sim 1.0$ throughout high-b region ($|b| > 25°$), where the present analysis focuses on.

As a summary of the above analysis, the intensity ratios of near-IR to $100\,\mu$m emission are expected to be nearly invariant in the high-b diffuse ISM and the near-IR thermal emission does not contribute to the observed b-dependence. As shown in Figure 4.2, the intensity of the near-IR emission predicated by DL07 is by several factors lower than that of scattered light at 1.25 and $2.2\,\mu$m. This fact also indicates that the near-IR thermal emission component is small.

4.2.3 Comparison with improved scattered light model

To reanalyze the b-dependence of the scattered light, a plane-parallel galaxy is assumed, same as BD12. The BD12 model assumes single scattering by dust grains, which is rea-

sonable for the optically thin diffuse ISM in the near-IR. The dust and stellar sheets are assumed to be located at z and z_s from the Galactic plane, respectively. Considering dust extinction of the starlight and scattered light, the scattered intensity is calculated as a function of b:

$$
\begin{aligned}
I_{\lambda,\text{sca}}(b) &= \omega_\lambda \csc|b| \int_0^{\tau_\lambda(0)} d\tau_\lambda \exp[-\csc|b|(\tau_\lambda(0) - \tau_\lambda)] \\
&\times \int_0^\infty R\,dR \int_0^{2\pi} d\theta\, \Phi_\lambda \frac{\exp[-A_\lambda(z, z_s, R)]}{4\pi[(z-z_s)^2 + R^2]} \\
&\times \int_0^\infty P_\lambda(z_s)\,dz_s,
\end{aligned}
\tag{4.6}
$$

$$
\tau_\lambda(z) \equiv \int_z^\infty \sigma_{\text{ext}}(\lambda)\rho(z')dz', \tag{4.7}
$$

$$
A_\lambda(z, z_s, R) \equiv |\tau_\lambda(z) - \tau_\lambda(z_s)| \frac{\sqrt{(z-z_s)^2 + R^2}}{|z - z_s|}, \tag{4.8}
$$

where ω_λ, Φ_λ, and $\sigma_{\text{ext}}(\lambda)$ denote, respectively, albedo, scattering phase function, and extinction cross section. These dust properties are assumed to be independent of b. The quantities $P_\lambda(z_s)$ and $\rho(z)$ are the surface power density of the stellar sheet and dust density, respectively. Once these quantities are supplied, scattered intensity is calculated by Equation (4.6) without free parameters. Similarly, total IR intensity reradiated from dust grains can be calculated from the absorbed radiation. Since the $100\,\mu$m-band intensity is proportional to the total IR intensity, the BD12 model results in the b-dependence of the $100\,\mu$m emission:

$$
I_{100} \propto \csc|b|. \tag{4.9}
$$

Therefore, the b-dependence of the intensity ratio $I_{\lambda,\text{sca}}/I_{100}$ is derived from Equation (4.6) and (4.9). See Appendix B.2 for detail about the calculation.

The dust density $\rho(z)$ and stellar power density $P_\lambda(z_s)$ are assumed to have the same distribution as BD12. The dust density $\rho(z)$ is set to the Gaussian distribution:

$$
\rho(z) \propto \exp\left(-\frac{z^2}{2\sigma^2}\right) \tag{4.10}
$$

with $\sigma = 250\,\text{pc}$ (Malhotra 1995; Nakanishi & Sofue 2003). For the stellar power density $P_\lambda(z_s)$, the following two cases, Case 1 and 2, are considered. In Case 1, stellar distribution is a sum of two exponential:

$$
P_\lambda(z_s) \propto 0.9\exp(-z_s/\sigma_1) + 0.1\exp(-z_s/\sigma_2) \tag{4.11}
$$

with $\sigma_1 = 300\,\text{pc}$ and $\sigma_2 = 1350\,\text{pc}$, respectively (Binney & Merrifield 1998; Gilmore & Reid 1983). Case 1 is thus based on the observed stellar distribution in the Milky Way. In

87

Case 2, all stars exist in the Galactic plane, which corresponds to $z_s = 0$ in Equation (4.6). This simplified stellar distribution was adopted in the previous estimation of b-dependence of the scattered light (J79).

In the calculation of scattered light (Equation 4.6), the phase function Φ_λ is expressed as a function of scattering angle, such as the HG41 form (Equation 1.5). In the near-IR, however, D03 suggests that the HG41 form deviates from the WD01 phase function estimated by the Mie theory. D03 thus developed a new analytical form which can be fitted to the WD01 phase function:

$$\phi_\alpha(\theta) = \frac{1}{4\pi} \frac{1 - g_\alpha^2}{(1 + g_\alpha^2 - 2g_\alpha \cos\theta)^{3/2}} \frac{1 + \alpha \cos^2\theta}{1 + \alpha(1 + 2g_\alpha^2)/3}, \tag{4.12}$$

where g_α and α are free parameters. In case of $g_\alpha = 0$ and $\alpha = 1$, this form represents Rayleigh scattering. Also, it is reduced to the HG41 form in case of $\alpha = 0$. By comparing the first and second moments of the WD01 phase function with those of the D03 form, the parameters g_α and α can be derived to reproduce the WD01 phase function. See Appendices of D03 for detail of this calculation.

To compare the b-dependence of the model with that observed with DIRBE, the calculation is conducted by using the WD01 dust properties at 1.22 and 2.19 μm, which are close to the two DIRBE bands at 1.25 and 2.2 μm. Since the analyzed region is diffuse ISM in high-b region, the $R_V = 3.1$ Milky Way dust is assumed. In the WD01 model adopted in this analysis, the grain abundances are reduced by factor 0.93 from the original WD01 to be consistent with the interstellar extinction (Draine 2003a). The data including the DL07 and WD01 models are available at the website: "www.astro.princeton.edu/$\sim$ draine/".

In Figure 4.8, the WD01 phase function is compared with the analytical forms of HG41 and D03 at 1.22 and 2.19 μm. The WD01 phase function shows stronger forward and backward scattering than the HG41 form. In contrast, D03 well reproduces the WD01 phase function in both bands. From 1.22 to 2.19 μm, the WD01 phase function becomes closer to the shape of Rayleigh scattering as difference between typical grain size and wavelength is larger.

Figure 4.9 illustrates the modeled ratios $I_{\lambda,\mathrm{sca}}/I_{100}$ as a function of $|b|$ in comparison with the observation. The numerical calculation is conducted for the two phase function (HG41 and D03) with two stellar distribution (Case 1 and 2). To see only the b-dependence, all are scaled to unity at $|b| = 20°$. The models assuming Case 2 with the HG41 form (red dashed curves) should be close to the J79 approximation. For comparison, the J79 form is represented by black dotted curves with the g-factor set to the first moment of the WD01 phase function, i.e., 0.289 and 0.131 at 1.22 and 2.19 μm, respectively. The difference between the present calculation and the J79 model is within $\sim 10\%$ in both bands. The
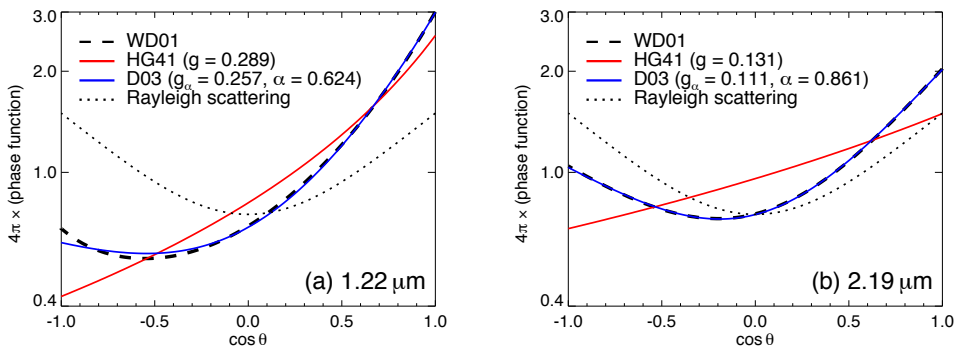
Figure 4.8 Comparison of scattering phase function as a function of cosine of scattering angle θ at (a) 1.22 and (b) 2.19 μm. In each panel, black dashed curve represents the WD01 phase function for the $R_V = 3.1$ dust. Red and blue curves indicate, respectively, the HG41 and D03 phase function formulated by Equation (1.5) and (4.12). The g-factor in the HG41 form comes from the first moment of the WD01 phase function. In the D03 form, the parameters g_α and α are determined to be fitted to the WD01 phase function (see Appendices of D03). For comparison, the phase function for Rayleigh scattering $[\Phi = (3/16\pi)(1 + \cos^2\theta)]$ is indicated by black dotted curve.
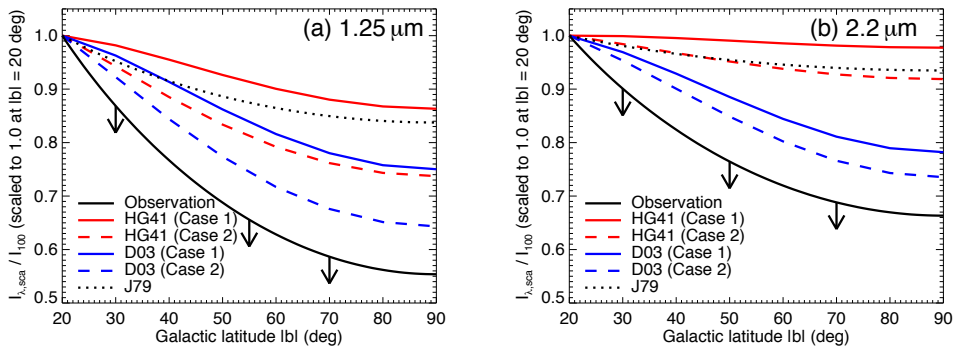
Figure 4.9 Intensity ratios of the scattered light to $100\,\mu$m emission $I_{\lambda,\mathrm{sca}}/I_{100}$ as a function of $|b|$, which are derived from the DIRBE observation and from the BD12 model at (a) 1.22 and (b) $2.19\,\mu$m. In each panel, black solid curve indicates the observed b-dependence represented by Equation (4.5) with 1-sigma lower limit of the derived g-factor. Case 1 and 2 assume, respectively, the stellar distribution to be the sum of two exponential and to be concentrated to the Galactic plane (see text). The solid (dashed) red and blue curves represent, respectively, the Case 1 (2) results assuming the HG41 and D03 forms. The black dotted curve indicates the previous approximation (J79) with g set to the first moment of the WD01 phase function. All are scaled to unity at $|b| = 20°$.

discrepancy may be caused by different assumption of the dust distribution: J79 did not take into account the gradient of the dust density toward z direction since they assumed a single cloud in a high-b region.

In section 4.2.1, the high g-factor is obtained from the J79 approximation that assumed the HG41 phase function (Equation 4.5). However, Figure 4.9 shows that the models adopting the D03 form cause the steeper b-dependence than those assuming the HG41 form. This indicates that the g-factor (i.e., the first moment of the phase function) is overestimated when comparing the observed b-dependence with scattered light models assuming the HG41 form. Therefore, fitting to the J79 form would overestimate the g-factor and the real value is lower than ~ 0.7.

As naturally expected from the geometry, Case 2 produces the steeper b-dependence than Case 1 (Figure 4.9). Though Case 1 should be closer to the current understanding of the stellar distribution in the Milky Way, it would be difficult to create the observed steep b-dependence (black solid curve in Figure 4.9). This may indicate that the interstellar dust properties should be modified from the WD01 model. Presence of larger grains is expected to make the phase function more forward directed and make the b-dependence steeper. Therefore, the observed b-dependence may suggest the population of large grains in addition to the WD01 model.

4.3 Implication of interstellar dust in high Galactic latitudes

In this chapter, interstellar dust properties in high-b diffuse ISM are investigated based on the near-IR DGL observation. From the color of the scattered light, the grain albedo supposedly show redder spectrum than the WD01 dust model. From the b-dependence of the scattered light, forward scattering characteristic is expected to be stronger than the WD01 dust. Both results may suggest the presence of large grains in the diffuse ISM. In the following, origin of the large dust is discussed in comparison with other observations.

At $3 \sim 10 \, \mu$m, interstellar extinction curve reportedly shows flat wavelength dependence (Wang et al. 2013; Nishiyama et al. 2009; Gao et al. 2009; Flaherty et al. 2007; Jiang et al. 2006; Indebetouw et al. 2015; Lutz 1999). To reproduce the flat extinction curve, Wang et al. (2015) added μm-sized grains to the WD01 model. Notably, this modification does not violate the observed extinction curve from UV to near-IR. The possible presence of large grains has also been suggested by the observation of high albedo in the near-IR (Block et al. 1994; Witt et al. 1994; Lehtinen & Mattila 1996).

Steinacker (2010) observed dense core parts of molecular clouds and found the scattered light component at 3.6 and 4.5 μm. This finding suggests the presence of sub-μm to μm-

sized grains and the grain growth in the dense part of the molecular clouds. It is thus possible that such large grains are also present in the diffuse ISM. They also proposed a phase function with strong forward scattering for the large grain population.

It is probable that the large grains exist as porous dust aggregates. Since the conventional Mie theory cannot be applied to the nonspherical grains, scattering and absorption properties are expected to be different from spherical dust. To estimate the scattering properties of the dust aggregates, several studies have developed various numerical methods, such as the discrete dipole approximation and the T-matrix method (e.g., Purcell & Pennypacker 1973; Draine & Flatau 1994; Mishchenko et al. 1996; Tazaki et al. 2016). Due to the change in the phase function, these additional factors including the size distribution and shape of the dust grains are expected to influence the b-dependence of the scattered light. Further analysis is needed to create a dust model that reproduces simultaneously the redder color and steep b-dependence of the scattered light.

In the present analysis, grain size distribution is assumed to be invariant throughout the high-b region. If this assumption is not true, the observed b-dependence may be affected by the regional variation of the g-factor. To invetigate the b-dependence of the dust properties in high latitudes, the scattered light measurements from UV to optical would be helpful in addition to the present near-IR analysis.

In principle, the scattered light depends on the ISRF intensity. The adopted MMP83 model is based on the stellar spectra observed in the solar vicinity. Derivation of more precise ISRF in various regions of the sky requires both photometric and astrometric information of stars, which will be provided by the GAIA mission in the future (Perryman et al. 2001). GAIA will measure the accurate distance and photometry of one billion stars.

Chapter 5

Origin of the Near-Infrared Diffuse Isotropic Light

As described in subsection 3.3.4, the diffuse isotropic light is several times larger than the IGL at 1.25 and $2.2\,\mu$m. This indicates the presence of a large diffuse light component. In this chapter, origin of the diffuse component is discussed.

5.1 Contribution of extragalactic sources

Several studies have suggested contribution of exotic sources to the EBL in addition to the IGL. In Figure 5.1, theoretical contributions of these sources are compared with the diffuse isotropic light. Salvaterra & Ferrara (2003) first suggested the contribution of primordial Pop-III stars to explain the near-IR excess observed with *IRTS* (Matsumoto et al. 2005). However, from theoretical constraints on the formation rate of Pop-III stars, Dwek et al. (2005a) concluded that Pop-III stars contribute only a fraction of the EBL intensity. This is consistent with recent predictions of the Pop-III contribution: $\lesssim 0.1\,\mathrm{nW\,m^{-2}\,sr^{-1}}$ in the near-IR (e.g., Cooray et al. 2012a, Inoue et al. 2013, Fernandez & Zaroubi 2013).

Several studies have calculated other exotic sources' contribution to the EBL, such as intrahalo light (IHL), accreting direct collapse black holes (DCBH), dark stars (DS), and sterile neutrino decay. Cooray et al. (2012b) and Zemcov et al. (2014) suggested the IHL contribution to explain a few arcsec-scale excess in the angular power spectrum of the diffuse near-IR background (Cooray et al. 2012a; Kashlinsky et al. 2005; Cooray et al. 2007; Thompson et al. 2007; Matsumoto et al. 2011; Kashlinsky et al. 2012). The IHL is thought to be created by tidally stripped stars from their parent galaxies by mergers and collisions (Cooray et al. 2012b). The IHL intensity estimated by Zemcov et al. (2014) is ~ 7 and $\sim 2\,\mathrm{nW\,m^{-2}\,sr^{-1}}$ at 1.25 and $2.2\,\mu$m, respectively (Figrue 5.1). Therefore, the sum
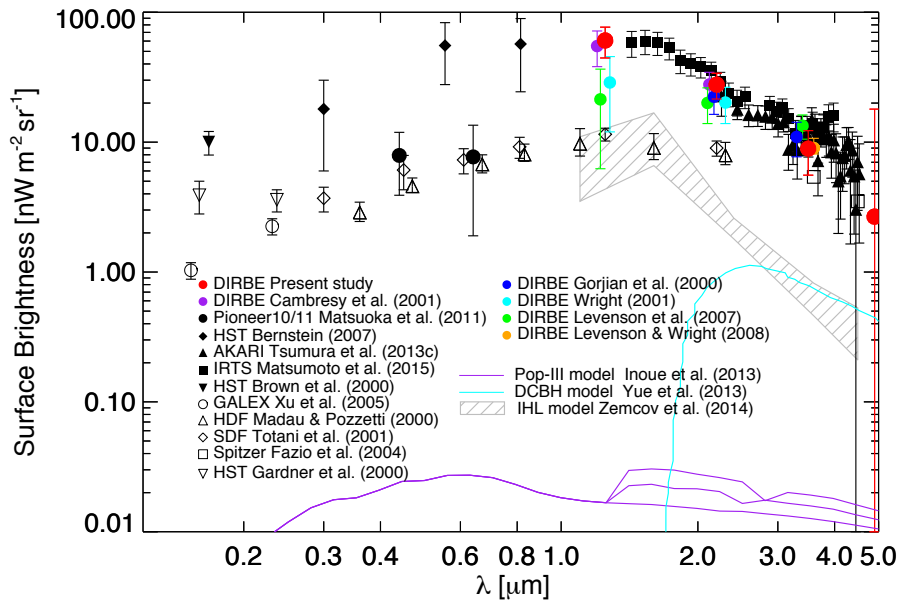
Figure 5.1 Contribution of hypothetical extragalactic objects to the EBL from UV to near-IR. Expected spectra from Pop-III stars (Inoue et al. 2013), DCBH (Yue et al. 2013), and IHL (Zemcov et al. 2014) are indicated by purple curve, cyan curve, and shaded area, respectively. Observed results of diffuse residual emission and IGL are indicated by the same symbols as those in Figure 3.21.

of the IHL and the observed IGL approaches the diffuse isotropic light derived by using the Wright model (Gorjian et al. 2000, Wright 2001, Levenson et al. 2007). To explain the excess in the power spectrum, Yue et al. (2013) suggested another candidate, DCBHs in the early universe. The contribution of DCBHs to the EBL intensity has a peak at $\sim 2\,\mu$m and is less than $\sim 1\,\mathrm{nW\,m^{-2}\,sr^{-1}}$ at IR wavelengths (Figure 5.1).

DSs are the hypothetical objects powered by annihilation of either accreted or captured weakly interacting massive particles before the standard nuclear fusion. Maurer et al. (2012) separately estimated the contribution of the colder DS and the hotter ones. As a result, the contribution of the hotter DSs could have reach the intensity of ~ 10 and $\sim 20\,\mathrm{nW\,m^{-2}\,sr^{-1}}$ at 1.25 and 2.2 μm, respectively. Mapelli & Ferrara (2005) calculated the contribution of sterile neutrino decay to the EBL. They found that the intensity is only less than $\sim 10^{-10}\,\mathrm{nW\,m^{-2}\,sr^{-1}}$ in the near-IR.

The sum of these exotic sources' contribution may reach the intensity of the derived diffuse isotropic light at 2.2 μm. In contrast, the total of these objects contributes less than $\sim 20\,\mathrm{nW\,m^{-2}\,sr^{-1}}$ at 1.25 μm. This indicates that the present result is approximately two times higher than the sum of the exotic sources' contribution and the observed IGL.

5.2   Constraint from γ-ray observation

As explained in Chapter 1, EBL intensity can be constrained by measuring attenuation of high-energy γ-ray emitted from blazars. The EBL constraints derived from the γ-ray observations with different assumptions of the intrinsic spectra (e.g., Dwek & Krennrich 2005, Schroedter 2005, Aharonian et al. 2006, Mazin & Raue 2007, Orr et al. 2011, Meyer et al. 2012, Abramowski et al. 2013) result in the low EBL intensity, close to the observed IGL level, except that Guy et al. (2000) allowed the higher upper limit of $\sim 60\,\mathrm{nW\,m^{-2}\,sr^{-1}}$ at $\sim 1\,\mu$m.

In Figure 5.2, the recent EBL constraint derived from H.E.S.S. (Abramowski et al. 2013) is indicated by shaded region. The IGL model from Domínguez et al. (2011) is plotted by a dotted curve. This model is comparable to other models (e.g., Stecker et al. 2006, Mazin & Raue 2007, Franceschini et al. 2008, Finke et al. 2010; Stecker et al. 2016) and is marginally consistent with the observed IGL intensity. The γ-ray constraint is the same level as the IGL model, though there seems room for presence of an additional component other than the IGL. However, the γ-ray limit conflicts with the derived diffuse isotropic light at 1.25 and 2.2 μm. Assuming that the near-IR excess observed with *IRTS* (Matsumoto et al. 2005) entirely originates from extragalactic sources, Dwek et al. (2005b) suggested that such a large emission would result in a physically unrealistic γ-ray spectrum of the blazar PKS
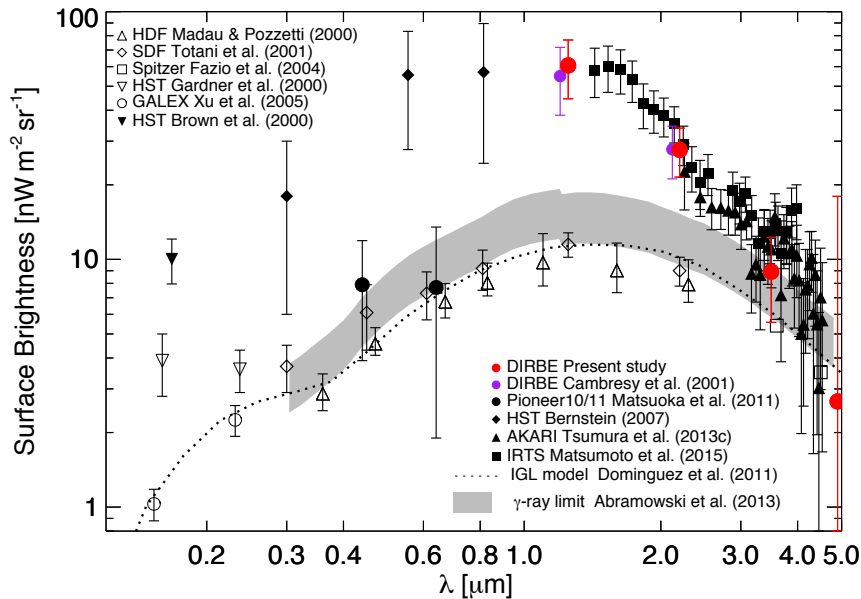
Figure 5.2 Comparison of diffuse isotropic light with IGL model and γ-ray constraint on the EBL. The IGL model spectrum is represented by black dotted curve (Domínguez et al. 2011). The γ-ray limit on the EBL are indicated by shaded region (Abramowski et al. 2013).

2155-304. These analyses indicate that all excess light cannot be attributed to extragalactic sources.

5.3   Contribution of local emission components

Considering the potential extragalactic sources' contribution and the γ-ray constraints, it is increasingly difficult to attribute all the diffuse isotropic light to the distant universe origin, particularly at $1.25\,\mu$m. Therefore, it is possible that the excess light contains light originating from the local universe, including the Milky Way and the solar system.

5.3.1   Diffuse isotropic light in the Milky Way

In the Milky Way, warm ionized medium (WIM) with temperature of $\sim 10^4\,$K is present in the halo region. From the WIM, the free-free, recombination, and two-photon processes of ionized hydrogen gas create the continuum in the optical and near-IR wavelengths. Based on the emissivities of these radiative process with electron temperature of $T_e = 8000\,$K

(Draine 2011) and typical emission measure of $1.9 \pm 0.3 \, \mathrm{cm}^{-6} \, \mathrm{pc}$ (Gaensler et al. 2008), the intensity of the radiation is estimated to be less than $\sim 1 \, \mathrm{nW} \, \mathrm{m}^{-2} \, \mathrm{sr}^{-1}$. This amount is negligible relative to the diffuse isotropic light in the near-IR. Bernstein (2002) estimated the comparable intensity in optical wavelengths.

In their interpretation of diffuse isotropic components derived in the far-IR (140 and $240 \, \mu \mathrm{m}$), Dwek et al. (1998) suggested that the Galactic component cannot produce that intensity because unreasonably massive gas and dust are needed. From this point of view, the diffuse near-IR isotropic light in the Milky Way, the counterpart of the isotropic far-IR emission from ISM, is unlikely to contribute to the diffuse isotropic light. Around M31, Lehner et al. (2015) reported the presence of massive circumgalactic medium. In the present understanding, however, it is unclear that such a component also exists around the Milky Way and creates a large isotropic light. In conclusion, diffuse isotropic light from the Milky Way probably do not explain the near-IR excess.

5.3.2 Hypothetical interplanetary dust in the solar system

In the DIRBE ZL model (Kelsall et al. 1998), the IPD parameters including optical properties and geometric configuration are derived by fitting to the seasonal variation of the ZL observed from the Earth. In this method, an isotropic ZL component was not taken into account even if it exists. Hauser et al. (1998) stated, "this method cannot uniquely determine the true ZL signal; in particular, an arbitrary isotropic component could be added to the model without affecting the parameter values determined in the fitting to the seasonal variation of the signal." In fact, the near-IR spectrum of the diffuse isotropic light (Matsumoto et al. 2005) is similar to that of the ZL (Dwek et al. 2005a). They suggested that difference between the diffuse isotropic light and the IGL corresponds to $\sim 20\%$ of the ZL if the entire excess originates from the ZL. From optical to near-IR, Figure 5.3 illustrates the scaled solar spectrum (Gueymard et al. 2002) in comparison with the difference between the diffuse isotropic light and the IGL model (hereafter "excess light"). Their spectra are similar in shape, indicating possible presence of an additional IPD component.

It is natural that the hypothetical IPD is distributed around the Sun. However, it is questionable that such a component can be seen as isotropic from the Earth. To simulate the isotropy of the hypothetical scattered sunlight, the intensity is calculated as a function of solar elongation angle ϵ as follows. The specific intensity of the hypothetical scattered light is calculated as

$$I_\lambda(\epsilon) = \int n(r) F_\lambda(r) \phi_\lambda(\theta) A_\lambda ds, \tag{5.1}$$

where $n(r)$ is line density of the hypothetical IPD as a function of heliocentric distance r

and $F_\lambda(r)$ is the solar flux incident on IPD grains at r. The parameters $\phi_\lambda(\theta)$ and A_λ are the scattering phase function and albedo of the hypothetical IPD. For simplicity, $n(r)$ is assumed to be constant in the calculation. The dust properties $\phi_\lambda(\theta)$ and A_λ are set to the same values as those determined in the DIRBE ZL model (Kelsall et al. 1998). If $n(r)$ and radius of the IPD cloud (R) are assumed, intensity of the hypothetical ZL can be calculated as a function of solar elongation angle ϵ (see Appendix C for detail).

The results are shown in Figure 5.4. In the calculation, n and R are arbitrarily set to reproduce the excess light (Figure 5.3). In the DIRBE ZL model, IPD line density at 1 AU is determined to be $1.13 \times 10^{-7}\,\mathrm{AU}^{-1}$. As shown in the figure, the hypothetical IPD with 5%–10% of this line density can explain the excess light in both bands. If the proper radius is assumed, the IPD with a certain line density reproduces the intensity of the excess light at 1.25 and 2.2 μm simultaneously. This indicates that the color of the excess light is similar to that of the hypothetical scattered sunlight.

In the mid-IR, thermal emission from the IPD dominates the diffuse sky brightness. Hauser et al. (1998) derived the residual light at 25 μm by subtracting the ZL component from the DIRBE sky brightness, using the DIRBE ZL model. Intensity of the residual light is 5%–10% of that of the DIRBE ZL model in the Lockman Hole (Figure 2 of Hauser et al. 1998). Therefore, the residual light at 25 μm is roughly comparable to the thermal emission from the hypothetical IPD that explains the near-IR excess. This means that the hypothetical IPD probably do not conflict with the mid-IR result.

In Figure 5.4, the intensity variation of the hypothetical scattered sunlight is marginally within the uncertainty of the excess light in $\epsilon \gtrsim 90°$, where space observations are conducted to avoid viewing the direct sunlight. This indicates that the isotropic EBL component would not be distinguished from the hypothetical scattered sunlight in the usual space observations from the Earth orbit.
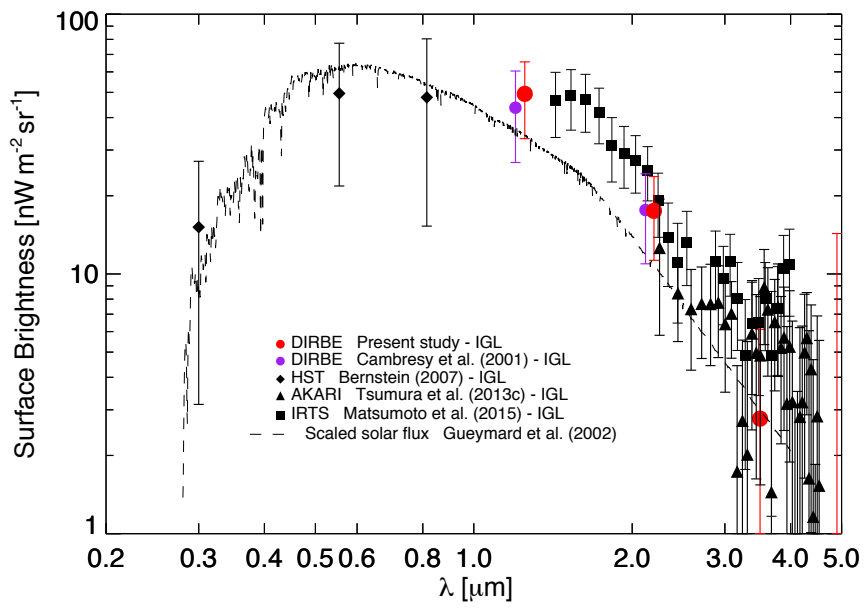
Figure 5.3 Optical to near-IR spectra of isotropic emission from which the IGL contribution is removed by using the IGL model (Domínguez et al. 2011). Dashed curve represents scaled solar spectrum (Gueymard et al. 2002).
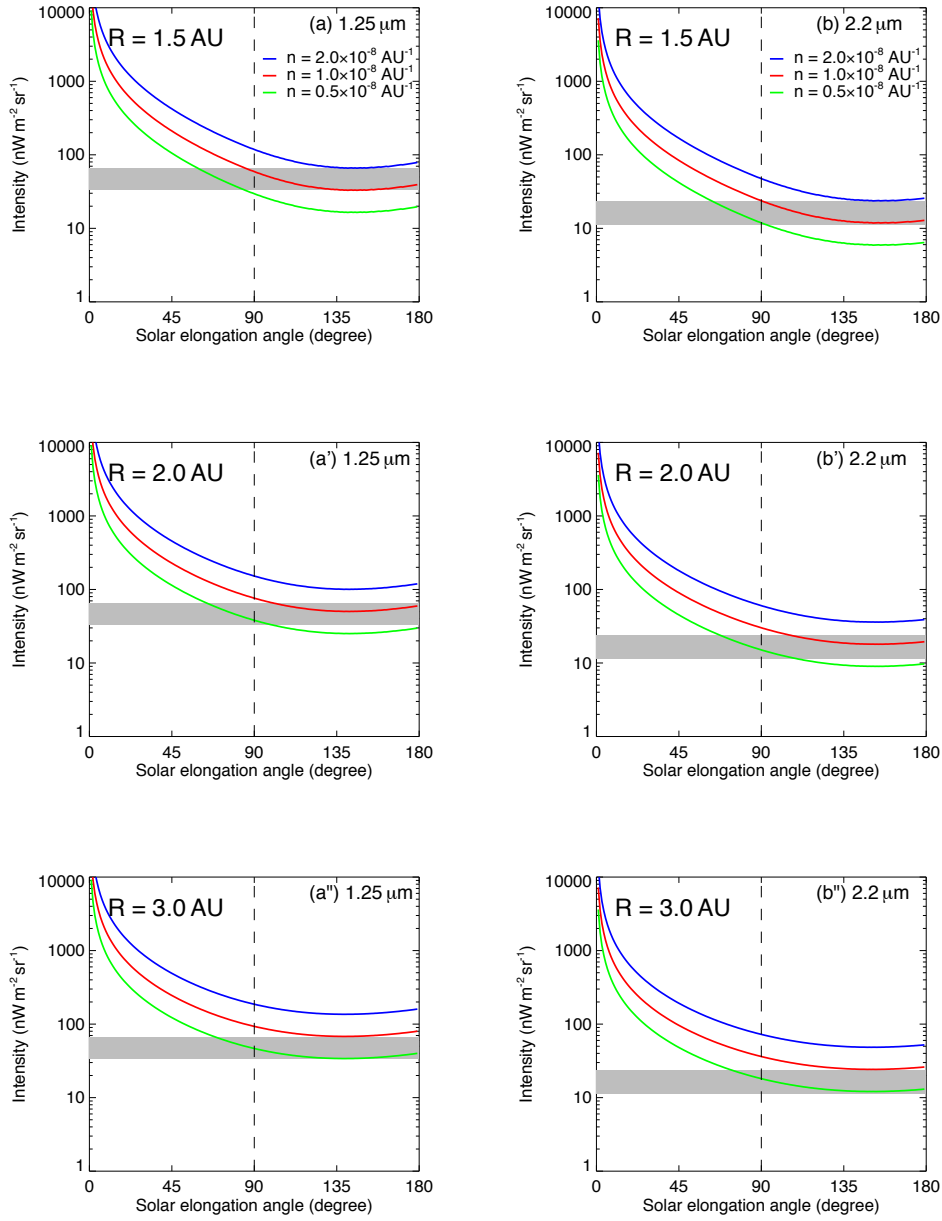
Figure 5.4 Intensity of hypothetical scattered sunlight as a function of solar elongation angle, calculated from Equation (5.1) at 1.25 (left panels) and 2.2 μm (right panels). Blue, red, and green curves indicate results for the hypothetical IPD density of 2.0×10^{-8}, 1.0×10^{-8}, and 0.5×10^{-8} AU^{-1}, respectively. Radii of the hypothetical IPD cloud are assumed as 1.5 AU (a and b), 2.0 AU (a' and b'), and 3.0 AU (a" and b"). Shaded regions indicate the present result of the diffuse isotropic light, from which the IGL is removed. (Domínguez et al. 2011).

5.4   Future prospect of diffuse light study

As shown in this chapter, the isotropic excess light can be explained by the hypothetical IPD distributed around the Sun. The presence of such an isotropic component might be related to the solar system formation, which includes the way to accumulate planetesimal. On the other hand, in comparison with the γ-ray constraint on the EBL (Figure 5.2), there is also room for the presence of extragalactic objects other than the normal galaxies. To reveal the origin of the excess light, following methods or projects would be useful as future prospects.

As seen from Figure 5.4, the diffuse isotropic light is expected to increase toward regions of small solar elongation angle if the additional scattered component is present in the solar system. In addition to the adopted DIRBE $\epsilon = 90°$ map, all-sky data obtained with various solar elongation angle ($64° < \epsilon < 124°$) are available in the DIRBE products. By applying the same decomposition analysis as the present study to these data, the diffuse isotropic light is derived as a function of solar elongation angle. This method is thought to be useful in searching for an additional IPD component in the solar system.

To measure the EBL without the uncertainty of the foreground subtraction, the dark cloud method would be the most effective, though several trials have not succeeded in deriving the EBL intensity. The failure is partly due to weak shielding effect of usual dark clouds with low optical depth. To achieve strong shielding, more dence clouds, so called infrared dark clouds ($A_V \gtrsim 20\,\mathrm{mag}$) would be appropriate targets. Since such objects are reportedly present near the Galactic plane, observation with a sharp point spread function is needed to suppress the contamination of Galactic stars. HST or James Webb Space Telescope (JWST) are expected to be suitable for such observations.

As shown in Figure 5.1 and 5.3, spectral measurements are also helpful in constraining origin of the isotropic component. In contrast to the near-IR observations, spectral shape of diffuse isotropic light is quite uncertain in the optical. In the near future, CIBER-II, a rocket-borne experiment is planned to observe diffuse sky brightness in optical wavelengths (Shirahata et al. 2016). By revealing the spectral shape in the optical, origin of the isotropic light will be constrained.

As a project to observe the diffuse sky brightness beyond the IPD region, EXo-Zodiacal Infrared Telescope (EXZIT), one of the science instruments of the Solar Power Sail spacecraft is planned for launch in 2020s (Matsuura et al. 2014). The EXZIT observation will reveal the three-dimensional structure of IPD and measure the absolute EBL intensity without assuming the ZL model.

Chapter 6

Summary of this thesis

Near-infrared (IR) diffuse light consists of zodiacal light (ZL), integrated starlight (ISL), diffuse Galactic light (DGL), and diffuse isotropic light including extragalactic background light (EBL). The ZL comprises scattered light and thermal emission from interplanetary dust (IPD) heated by sunlight. The near-IR DGL is composed of interstellar dust-scattered light and thermal emission from stochastic heating of very small grains including polycyclic aromatic hydrocarbon (PAH). The scattered light component in the DGL is therefore useful in constraining interstellar dust properties, such as grain size distribution, albedo, scattering asymmetry, while the thermal emission can be an indicator of mass fraction of the very small grains and PAH to the total dust. The EBL includes the entire radiation emitted from reionization to the present epoch. Therefore, the EBL measurement is of great importance in constraining the star-formation history of the universe and in searching for unknown radiation processes. To measure the DGL and EBL, it is necessary to evaluate the ZL and ISL accurately.

In 1990s, the Diffuse Infrared Background Experiment (DIRBE) onboard the *Cosmic Background Explorer* (*COBE*) satellite observed the all sky in 10 photometric bands from near to far-IR and analyzed the diffuse sky components. For the ISL evaluation, they used a star-counts model since all-sky photometric data of stars were not available at that time. Due to the large uncertainty in the ISL estimation, they failed to detect the DGL component in high Galactic latitudes. After that, contribution of the near-IR DGL to the sky brightness has been uncertain and ignored. In addition, there was also large uncertainty in the diffuse isotropic light.

In the present study, the diffuse near-IR radiation is reanalyzed by improving the ISL evaluation. The DIRBE all-sky maps at 1.25, 2.2, 3.5, and $4.9\,\mu$m are used as total diffuse near-IR brightnesses. The ISL is evaluated by all-sky source catalogs created by the Two Micron All-Sky Survey (2MASS) and *Wide-field Infrared Survey Explorer* (*WISE*) satellite.

The 2MASS sources are used at 1.25 and 2.2 μm, while the *WISE* data are used at 3.5 and 4.9 μm. The ZL is evaluated by the DIRBE ZL model and the DGL is assumed to be a component that linearly correlates with interstellar 100 μm emission. At each band, the total sky brightness is assumed as a linear combination of the ZL, DGL, ISL, and isotropic light. To decompose each component from the DIRBE brightness, a χ^2 minimum analysis is conducted in high Galactic latitudes ($|b| > 35°$).

As a result, the DIRBE brightness is decomposed into the four components. In particular, linear correlations between diffuse near-IR light and interstellar 100 μm emission are found, which confirms the presence of the near-IR DGL in the diffuse interstellar medium. The DGL results are consistent with the *Cosmic Infrared Background Experiment* (*CIBER*) and *AKARI* observations. The derived isotropic light is several times larger than the integrated galaxy light at 1.25 and 2.2 μm, consistent with the *Infrared Telescope in Space* (*IRTS*) observation.

By comparing the DGL results with models of scattered light and thermal emission, dust properties in high-latitude interstellar field are investigated. The DGL brightness at 3.5 μm is dominated by the strong PAH emission at 3.3 μm and mass fraction of the very small grains and PAH is constrained to be $\sim 2\%$–8% in comparison with the thermal emission models. This is consistent with the *Spitzer* observation toward low Galactic latitudes, indicating the similar mass fraction throughout the sky. At 1.25 and 2.2 μm, the scattered light component is extracted by subtracting the thermal emission. The scattered light color is redder than that expected from a current dust model, indicating flatter albedo spectrum in 1–2 μm. This trend may imply the presence of larger dust grains in the diffuse interstellar medium.

By conducting the decomposition analysis in different Galactic latitude regions, intensity ratios of the DGL to 100 μm emission are found to increase toward low Galactic latitudes at 1.25 and 2.2 μm. Theoretically, this trend is expected from a scattered light model taking into account the forward scattering by dust grains. Since the conventional Henyey-Greenstein phase function reportedly deviates from that of the current dust model, the modified phase function is adopted to estimate the Galactic latitude dependence of the scattered light. As a result, the observed latitude dependence is steeper than the model prediction, indicating stronger forward scattering than the current dust model. To enhance the forward scattering, the large grains should be added to the dust model. This implication is consistent with the redder color of the scattered light.

Finally, origin of the large isotropic light is discussed. Deviation of the component from isotropy is less than 10% at 1.25 and 2.2 μm. At 1.25 and 2.2 μm, intensity of the isotropic light is also larger than the EBL constraints from high-energy γ-ray observation and exceeds

potential contribution from exotic sources, such as Population III stars and intrahalo light. It is thus difficult to attribute the difference between the isotropic light and the integrated galaxy light to the EBL, indicating local origin of the excess light.

As the local candidates, possible isotropic components within the Milky Way and solar system is estimated. Typical contribution of continuous emission from warm ionized medium in the Milky Way is expected to be negligible in comparison with the excess light. In the solar system, contribution of the isotropic scattered light is possibly present since the conventional DIRBE ZL model takes into account only the seasonal variation of the sky brightness and may miss the isotropic component. Therefore, the scattered sunlight from the hypothetical IPD distributed around the Sun is estimated. As a result, additional 5%–10% IPD density relative to the conventional ZL model can explain the excess light at 1.25 and 2.2 μm. In addition, the hypothetical scattered light is close to isotropic toward regions of solar elongation angle $\gtrsim 90°$, where usual space observation is conducted. This means that the isotropic EBL cannot be distinguished from the hypothetical scattered light if it exists. As a future prospect, observation beyond the Earth orbit will be useful to confirm the origin of the diffuse isotropic light.

Appendix A

List of Abbreviations

Table A.1 Abbreviation	
CMB	cosmic microwave background
DGL	diffuse Galactic light
DCBH	direct collapse black hole
DS	dark star
EBL	extragalactic background light
FSM	faint source model
IGL	integrated galaxy light
IHL	intra halo light
IPD	interplanetary dust
IR	infrared
ISL	integrated starlight
ISM	interstellar medium
ISRF	interstellar radiation field
PAH	polycyclic aromatic hydrocarbon
UV	ultraviolet
ZL	zodiacal light

Table A.2 Astronomical satellites

Satellite	launch year
Infrared Astronomical Telescope (*IRAS*)	1983
Cosmic Background Explorer (*COBE*)	1989
Hubble Space Telescope (*HST*)	1990
Infrared Telescope in Space (*IRTS*)	1995
Wilkinson Microwave Anisotropy Probe (*WMAP*)	2001
Spitzer Space Telescope (*Spitzer*)	2003
Galaxy Evolution Explorer (*GALEX*)	2003
Infrared Imaging Surveyor (*IRIS, AKARI*)	2006
Cosmic Infrared Background Experiment (*CIBER*)	2009
Wide-field Infrared Survey Explorer (*WISE*)	2009
Planck	2009

Appendix B

Models of Interstellar Scattering

B.1 Scattered light in dusty slab

Considering the radiative transfer of scattered light I_{sca} and starlight I_{star} through the dusty slab with optical depth τ, Ienaka et al. (2013) estimated the monochromatic scattered intensity. Radiative transfer of $I_{\mathrm{sca}}(\tau)$ and $I_{\mathrm{star}}(\tau)$ are expressed as

$$\frac{dI_{\mathrm{sca}}(\tau)}{d\tau} = \omega[I_{\mathrm{star}}(\tau) + I_{\mathrm{sca}}(\tau)] - I_{\mathrm{sca}}(\tau), \tag{B.1}$$

$$\frac{dI_{\mathrm{star}}(\tau)}{d\tau} = -I_{\mathrm{star}}(\tau), \tag{B.2}$$

where ω is grain albedo. The solution of Equation (B.2) is

$$I_{\mathrm{star}}(\tau) = I_{\mathrm{star}}(0)e^{-\tau}. \tag{B.3}$$

Using this result, the solution of Equation (B.1) is given as

$$I_{\mathrm{sca}}(\tau) = I_{\mathrm{star}}(0)\exp[-(1-\omega)\tau][1 - \exp(-\omega\tau)]. \tag{B.4}$$

The total IR intensity $I_{\mathrm{IR}}(\tau)$ reemitted by dust grains is approximated as

$$\frac{dI_{\mathrm{IR}}(\tau)}{d\tau} \propto (1-\omega)[I_{\mathrm{star}}(\tau) + I_{\mathrm{sca}}(\tau)]. \tag{B.5}$$

Using the solutions of $I_{\mathrm{star}}(\tau)$ and $I_{\mathrm{sca}}(\tau)$ (Equation B.3 and B.4), the total IR intensity is expressed as

$$I_{\mathrm{IR}}(\tau) \propto I_{\mathrm{star}}(0)[1 - \exp\{-(1-\omega)\tau\}]. \tag{B.6}$$

Since the $100\,\mu\mathrm{m}$ emission is proportional to the total IR emission, the intensity ratio of scattered light to the $100\,\mu\mathrm{m}$ emission is

$$\frac{I_{\mathrm{sca}}(\tau)}{I_{100}} \propto \frac{\exp[-(1-\omega)\tau][1 - \exp(-\omega\tau)]}{1 - \exp[-(1-\omega)\tau]}. \tag{B.7}$$
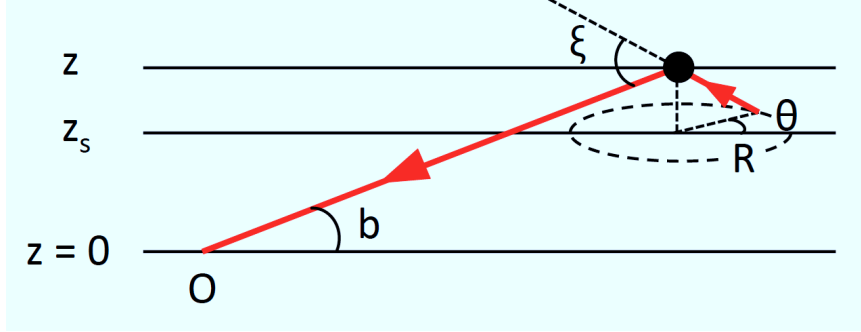
Figure B.1 Geometric configuration of a plane-parallel galaxy for calculating scattered light intensity as a function of Galactic latitude.

B.2 Scattered light in a plane-parallel galaxy

B.2.1 General formulation

Brandt & Draine (2012) estimated the scattered intensity in the Milky Way assuming the plane-parallel galaxy. From the calculation, b-dependence of the intensity ratio of the scattered light to $100\,\mu$m emission is estimated. The geometry used in the calculation is shown in Figure B.1. In this illustration, the Sun is located at the Galactic disk. The distances from the Galactic plane to uniform stellar and dust sheets are defined as z_s and z, respectively.

At first, vertical optical depth $\tau_{\lambda,\mathrm{ver}}(z)$ is defined as

$$\tau_{\lambda,\mathrm{ver}}(z) \equiv \int_z^\infty \sigma_{\mathrm{ext}}(\lambda)\rho(z')dz', \qquad (B.8)$$

where $\sigma_{\mathrm{ext}}(\lambda)$ and $\rho(z)$ are extinction cross section and density of the interstellar dust, respectively. Considering an annulus with radius R, which is centered on a foot of a perpendicular line from z to z_s, tilted optical depth $\tau_{\lambda,\mathrm{til}}(z, z_s, R)$ from the annulus to the grain is defined as

$$\tau_{\lambda,\mathrm{til}}(z, z_s, R) \equiv |\tau_{\lambda,\mathrm{ver}}(z) - \tau_{\lambda,\mathrm{ver}}(z_s)|\frac{\sqrt{(z - z_s)^2 + R^2}}{|z - z_s|}. \qquad (B.9)$$

Then total flux density incident on the grain is calculated as

$$F_\lambda(z, z_s) = \int_0^\infty 2\pi R\,dR \frac{1}{4\pi[(z - z_s)^2 + R^2]} P_\lambda(z_s) \exp[-\tau_{\lambda,\mathrm{til}}(z, z_s, R)], \qquad (B.10)$$

where $P_\lambda(z_s)$ is the surface power density at z_s. By converting variable of integration from R to r, $r = \frac{\sqrt{(z-z_s)^2 + R^2}}{|z-z_s|}$, Equation (B.10) is expressed as

$$F_\lambda(z, z_s) = \frac{1}{2} P_\lambda(z_s) \int_1^\infty dr \frac{\exp(-|\tau_{\lambda,\text{ver}}(z) - \tau_{\lambda,\text{ver}}(z_s)|r)}{r} \tag{B.11}$$

$$= \frac{1}{2} P_\lambda(z_s) E_1(|\tau_{\lambda,\text{ver}}(z) - \tau_{\lambda,\text{ver}}(z_s)|), \tag{B.12}$$

where E_1 is the first order exponential integral. The intensity of the total infrared emission radiated by dust grains is then derived as

$$I_{\text{TIR}}(b) = \int_0^\infty \int_0^\infty \int_0^{\tau_{\lambda,\text{ver}}(0)} \frac{1}{4\pi} (\csc|b| \, d\tau_{\lambda,\text{ver}}) F_\lambda(z, z_s)(1 - \omega_\lambda) dz_s d\lambda \tag{B.13}$$

$$= \frac{\csc|b|}{8\pi} \int_0^\infty (1 - \omega_\lambda) d\lambda \int_0^\infty P_\lambda(z_s) dz_s \int_0^{\tau_{\lambda,\text{ver}}(0)} d\tau_{\lambda,\text{ver}} \, E_1(|\tau_{\lambda,\text{ver}} - \tau_{\lambda,\text{ver}}(z_s)|), \tag{B.14}$$

where ω_λ is grain albedo. To convert the intensity of the total IR I_{TIR} to that of $100\,\mu$m emission in the DIRBE band I_{100}, the dust emission model should be assumed. In the DL07 model, the conversion formula is

$$\nu I_{100} = (0.52 \pm 0.05) I_{\text{TIR}}. \tag{B.15}$$

In the calculation of scattered intensity, the scattering anisotropy is taken into account. Considering an angle θ sweeping out the anulus from the opposite direction of us, law of cosine results in cosine of scattering angle ξ as

$$\cos\xi = \frac{R\cos\theta\cot b - (z - z_s)}{\sqrt{(1 + \cot^2 b)[(z - z_s)^2 + R^2]}}. \tag{B.16}$$

If a scattering phase function $\phi_\lambda(\cos\xi)$ is adopted, scattered intensity incident on the dust grain is calculated as

$$I_{\lambda,\text{sca}}(z, z_s, b) = \omega_\lambda \int_0^\infty \int_0^{2\pi} R \, d\theta \, dR \, \phi_\lambda(\cos\xi) \frac{1}{4\pi[(z - z_s)^2 + R^2]} P_\lambda(z_s) \exp[-\tau_{\lambda,\text{til}}(z, z_s, R)]. \tag{B.17}$$

By integrating the scattered intensity along the line of sight, the scattered intensity is calculated as a function of z_s:

$$I_{\lambda,\text{sca}}(z_s, b) = \omega_\lambda \int_0^{\tau_{\lambda,\text{ver}}(0)} (\csc|b| \, d\tau_{\lambda,\text{ver}}) \exp[-\csc|b|(\tau_{\lambda,\text{ver}}(0) - \tau_{\lambda,\text{ver}})]$$

$$\times \int_0^\infty R \, dR \int_0^{2\pi} d\theta \, \phi_\lambda(\cos\xi) \frac{1}{4\pi[(z - z_s)^2 + R^2]} P_\lambda(z_s) \exp[-\tau_{\lambda,\text{til}}(z, z_s, R)]. \tag{B.18}$$

Finally, the total scattered intensity is given as a function of b:

$$I_{\lambda,\text{sca}}(b) = \omega_\lambda \csc|b| \int_0^{\tau_{\lambda,\text{ver}}(0)} d\tau_{\lambda,\text{ver}} \exp[-\csc|b|(\tau_{\lambda,\text{ver}}(0) - \tau_{\lambda,\text{ver}})]$$

$$\times \int_0^\infty R \, dR \int_0^{2\pi} d\theta \, \phi_\lambda(\cos\xi) \frac{1}{4\pi[(z - z_s)^2 + R^2]} \int_0^\infty P_\lambda(z_s) dz_s \exp[-\tau_{\lambda,\text{til}}(z, z_s, R)]. \tag{B.19}$$

Combined with Equation (B.13) and (B.19), the intensity ratios of scattered light to the $100\,\mu$m emission is estimated as a function of b.

In the numerical calculation (Equation B.13 and B.19), the integral variable should be unified to z, since $\tau_{\lambda,\mathrm{ver}}$, and $\tau_{\lambda,\mathrm{til}}$ are expressed as a function of z. According to Definition (B.8), z changes from infinity to zero when $\tau_{\lambda,\mathrm{ver}}$ varies from zero to $\tau_{\lambda,\mathrm{ver}}(0)$. Therefore, Equation (B.13) is converted to

$$
\begin{aligned}
I_{\mathrm{TIR}}(b) &= \frac{\csc|b|}{8\pi}\int_0^\infty (1-\omega_\lambda)d\lambda \int_0^\infty P_\lambda(z_s)dz_s \int_0^\infty \sigma_{\mathrm{ext}}(\lambda)\rho(z)dz \int_0^\infty dR\, \frac{R}{(z-z_s)^2+R^2} \\
&\quad \times\ \exp\left(-\left|\int_{z_s}^z \sigma_{\mathrm{ext}}(\lambda)\rho(z')dz'\right| \frac{\sqrt{(z-z_s)^2+R^2}}{|z-z_s|}\right).
\end{aligned}
\tag{B.20}
$$

Similarly, Equation (B.19) is converted to

$$
\begin{aligned}
I_{\lambda,\mathrm{sca}}(b) &= \frac{\omega_\lambda \csc|b|}{4\pi}\int_0^\infty \sigma_{\mathrm{ext}}(\lambda)\rho(z)\exp\Bigg[-\Bigg(\csc|b|\int_0^z \sigma_{\mathrm{ext}}(\lambda)\rho(z')dz' \\
&\quad +\ \left|\int_{z_s}^z \sigma_{\mathrm{ext}}(\lambda)\rho(z')dz'\right|\frac{\sqrt{(z-z_s)^2+R^2}}{|z-z_s|}\Bigg)\Bigg]dz \\
&\quad \times\ \int_0^\infty R\,dR \int_0^{2\pi} d\theta\,\phi_\lambda(\cos\xi)\frac{1}{(z-z_s)^2+R^2}\int_0^\infty P_\lambda(z_s)dz_s.
\end{aligned}
\tag{B.21}
$$

B.2.2 Relation between the model and observation

In the numerical calculations, the dust density is assumed as

$$
\rho(z) = \rho_0 \exp\left(-\frac{z^2}{2\sigma^2}\right),
\tag{B.22}
$$

with $\sigma = 250\,\mathrm{pc}$ (Malhotra 1995; Nakanishi & Sofue 2003). The factor ρ_0 is derived from the observed optical depth τ_λ. Assuming that τ_λ is proportional to $\csc|b|$, the relation between τ_λ and $\rho(z)$ is

$$
\frac{\tau_\lambda}{\csc|b|} = \int_0^\infty \sigma_{\mathrm{ext}}(\lambda)\rho(z')dz'.
\tag{B.23}
$$

From Equation (B.23), ρ_0 is calculated as

$$
\rho_0 = \frac{\tau_\lambda}{\csc|b|}\frac{1}{\sigma_{\mathrm{ext}}(\lambda)\sigma}\sqrt{\frac{2}{\pi}}.
\tag{B.24}
$$

From the SFD reddening map $E(B-V)$, visual optical depth τ_V is derived as $\tau_V = 2.86\,E(B-V)$ for $R_V = 3.1$ dust. BD12 Figure 11 shows that the dust distribution is roughly between $\tau_V = 0.05\csc|b|$ and $\tau_V = 0.15\csc|b|$.

Once $\rho(z)$, $P_\lambda(z_s)$, interstellar dust properties ω_λ, ϕ_λ, and $\sigma_{\mathrm{ext}}(\lambda)$ are supplied, Equation (B.20) and (B21) are calculated without free parameters. The WD01 dust properties are shown in Figure B.2
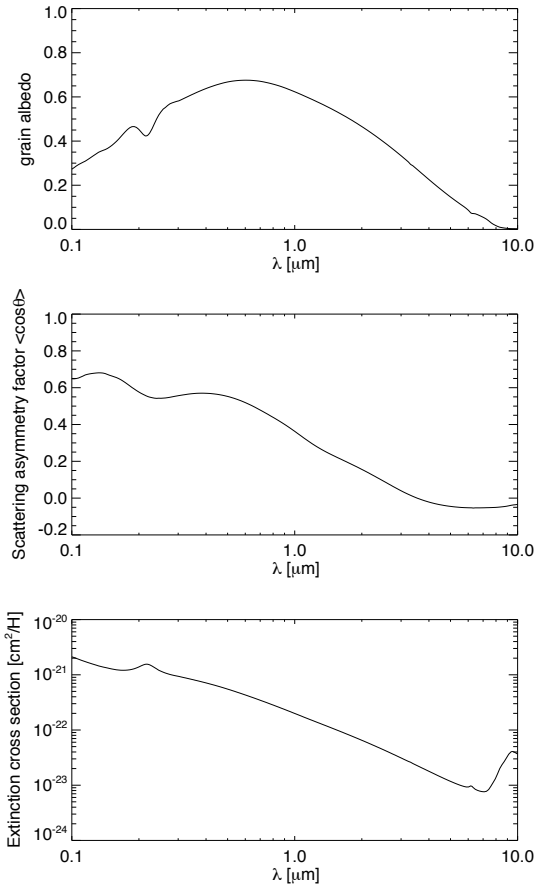
Figure B.2 Albedo, *g*-factor, and extinction cross section of interstellar dust in the WD01 model with $R_V = 3.1$ dust (Draine 2003b).

Appendix C

Calculation of Hypothetical Scattered Sunlight

Here is method to calculate scattered sunlight from hypothetical IPD distributed isotropically around the Sun. The geometry of the Earth, Sun, and hypothetical IPD is assumed as shown in Figure C.1. The radius of the hypothetical IPD cloud is set as R. The total scattered intensity toward the direction of solar elongation angle ϵ is calculated as

$$I_\lambda(\epsilon) = \int n(r) F_\lambda(r) \phi_\lambda(\theta) A_\lambda ds, \tag{C.1}$$

where $n(r)$ is the line density of the dust as a function of heliocentric distance r. $F_\lambda(r)$ is the solar flux incident on the dust grains at r:

$$F_\lambda(r) = \frac{F_\lambda(0)}{r^2}, \tag{C.2}$$

where $F_\lambda(0)$ is the solar flux at the Earth location, i.e., 1 AU from the Sun. The IPD phase function and albedo are described as $\phi_\lambda(\theta)$ and A_λ, respectively. Using the law of cosine, r and θ are described as a function of s:

$$r = \sqrt{s^2 - 2s \cos \epsilon + 1}, \tag{C.3}$$

$$\cos \theta = \frac{1 - (s^2 + r^2)}{2sr}. \tag{C.4}$$

Once $n(r)$ is supplied, the scattered intensity $I_\lambda(\epsilon)$ can be calculated by Equation (C.1).

The hypothetical IPD is assumed to show the same optical properties as the IPD determined in the DIRBE ZL model (Kelsall et al. 1998). In the DIRBE ZL model, the IPD phase function is approximated as

$$\phi_\lambda(\theta) = N[C_{0,\lambda} + C_{1,\lambda} \theta + \exp(C_{2,\lambda} \theta)], \tag{C.5}$$
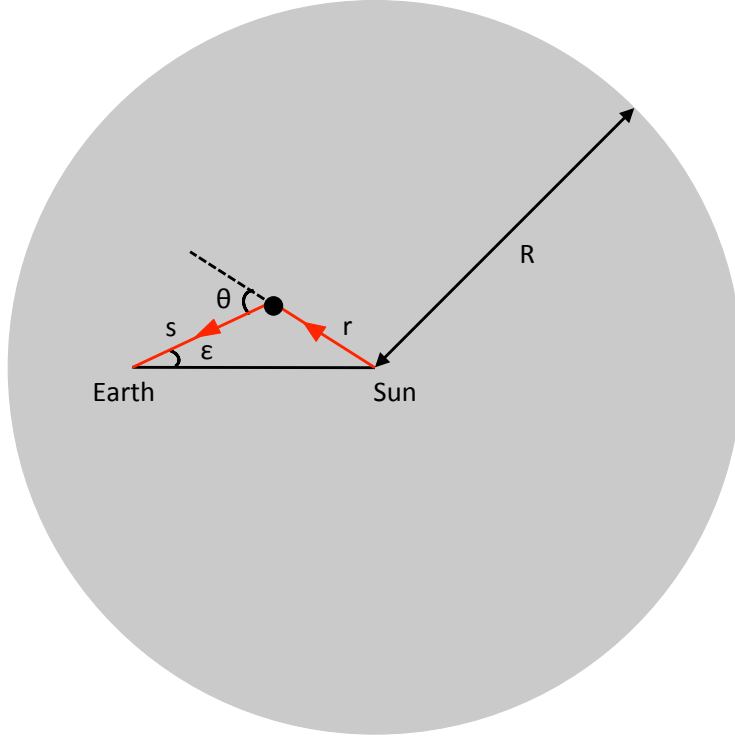
Figure C.1 Geometry of Sun, Earth, and hypothetical IPD for the scattered sunlight calculation.

$$N = \frac{1}{2\pi} \frac{1}{2\,C_{0,\lambda} + \pi\,C_{1,\lambda} + \frac{\exp(\pi\,C_{2,\lambda})+1}{C_{2,\lambda}^2+1}}, \tag{C.6}$$

where N is the normalization factor to yield the integration of the phase function over 4π to unity. The parameters $C_{0,\lambda}$, $C_{1,\lambda}$, and $C_{2,\lambda}$ were determined by fitting to the seasonal variation of the DIRBE intensity (Kelsall et al. 1998). The albedo and parameters of phase function at 1.25 and $2.2\,\mu$m are listed in Table C.1. The phase function $\phi_\lambda(\theta)$ (Equation C.5) is illustrated in Figure C.2.

Table C.1 IPD parameters at 1.25 and 2.2 μm in the DIRBE ZL model (Kelsall et al. 1998).

Band (μm)	1.25	2.2
A_λ	0.204 ± 0.001	0.255 ± 0.002
$C_{0,\lambda}$ (sr^{-1})	-0.942	-0.527
$C_{1,\lambda}$ $(\mathrm{rad}^{-1}\,\mathrm{sr}^{-1})$	0.121	0.187
$C_{2,\lambda}$ (rad^{-1})	-0.165	-0.598
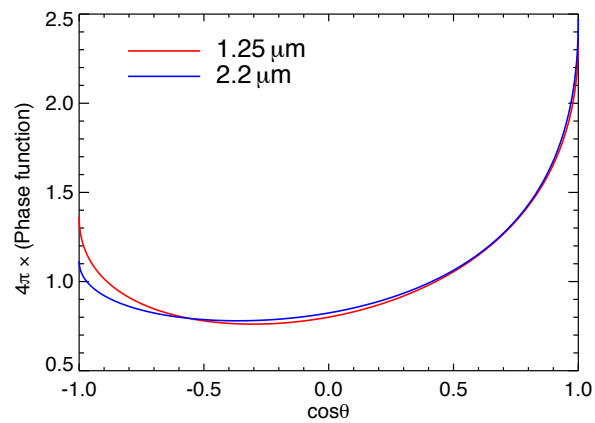
Figure C.2 IPD phase function in the DIRBE ZL model at 1.25 (red curve) and 2.2 μm (blue curve), represented by Equation (C.5).

Acknowledgements

Bibliography

Abramowski, A., Acero, F., Aharonian, F., et al. 2013, A&A, 550, A4

Aharonian, F., Akhperjanian, A. G., Bazer-Bachi, A. R., et al. 2006, Nature, 440, 1018

Albert, J., Aliu, E., Anderhub, H., et al. 2008, Science, 320, 1752

Arai, T., Matsuura, S., Bock, J., et al. 2015, ApJ, 806, 69

Arendt, R. G., Odegard, N., Weiland, J. L., et al. 1998, ApJ, 508, 74

Beichman, C. A. 1987, ARA&A, 25, 521

Bernstein, R. A. 2007, ApJ, 666, 663

Bernstein, R. A., Freedman, W. L., & Madore, B. F. 2002, ApJ, 571, 56

Berta, S., Magnelli, B., Nordon, R., et al. 2011, A&A, 532, A49

Binney, J., & Merrifield, M. 1998, Galactic Astronomy (Princeton, NJ: Princeton Univ. Press)

Binzel, R. P., Rivkin, A. S., Bus, S. J., Sunshine, J. M., & Burbine, T. H. 2001, Meteoritics and Planetary Science, 36, 1167

Block, D. L., Witt, A. N., Grosbol, P., et al. 1994, A&A, 288, 383

Bond, J. R., Carr, B. J., & Hogan, C. J. 1986, ApJ, 306, 428

Brandt, T. D., & Draine, B. T. 2012, ApJ, 744, 129

Brown, T. M., Kimble, R. A., Ferguson, H. C., et al. 2000, AJ, 120, 1153

Bruzual, G., & Charlot, S. 2003, MNRAS, 344, 1000

Bus, J. S., & Binzel, P. R. 2002, Icarus, 158, 106

Cambrésy, L., Reach, W. T., Beichman, C. A., & Jarrett, T. H. 2001, ApJ, 555, 563

Cassini, J.-D. 1685, Mem. Acad. Roy. Sci., Tome VIII

Caulet, A., Hook, R. N., Fosbury, R. A. E. 1994, A&AS, 108, 271

COBE Diffuse Infrared Background Experiment (DIRBE) Explanatory Supplement, Version 2.3. 1998, ed. Hauser, M. G., Kelsall, T., Leisawitz, D., & Weiland, J.

Cohen, M., 1993, AJ, 105, 1860

Cohen, M., 1994, AJ, 107, 582

Cohen, M., 1995, AJ, 444, 875

Compiègne, M., Verstraete, L., Jones, A., et al. 2011, A&A, 525, A103

Cooray, A., Gong, Y., Smidt, J., & Santos, M. G. 2012a, ApJ, 756, 92

Cooray, A., Smidt, J., de Bernardis, F., et al. 2012b, Nature, 490, 514

Cooray, A., Sullivan, I., Chary, R., et al. 2007, ApJ, 659, L91

Cutri, R. M., Skrutskie, M. F., van Dyk, S., et al. 2003, The IRSA 2MASS All Sky Point Source Catalog, NASA/IPAC Infrared Science Archive

Debye, P. 1909, Anp, 335, 57

Dermott, S. F., Jayraraman, S., Xu, Y. L., Gustafson, B. Å. S., & Liou, J. C. 1994, Nature, 369, 719

Désert, F.-X., Boulanger, F., & Puget, J. L. 1990, A&A, 237, 215

Désert, F.-X., Abergel, A., Bernard, J.-P., et al. 1996, Limits on the far infrared CIBR from DIRBE, FIRAS and HI surveys, in Dwek, E. (ed.) Unveiling the cosmic infrared background, AIP Conf. Proc. 348, 96

de Vries, C. P., & Le Poole, R. S. 1985, A&A, 145, L7

Domínguez, A., Primack, J. R., Rosario, D. J., et al. 2011, MNRAS, 410, 2556

Dole, H., Lagache, G., Puget, J.-L., et al. 2006, A&A, 451, 417

Draine, B. T. 2011, Physics of the Interstellar and Intergalactic Medium (Princeton University Press)

Draine, B. T. 2003b, ApJ, 598, 1017

Draine, B. T. 2003a, ARA&A, 41, 241

Draine, B. T., & Flatau, P. J. 1994, JOSAA, 11, 1491

Draine, B. T., & Li, A. 2007, ApJ, 657, 810

Driver, S. P., Andrews, S. K., Davies, L. J., et al. 2016, ApJ, 827, 108

Dwek, E., Arendt, R. G., Fixsen, D. J., et al. 1997, ApJ, 475, 565

Dwek, E., & Arendt, R. G. 1998, ApJ, 508, L9

Dwek, E., Arendt, R. G., Hauser, M. G., et al. 1998, ApJ, 508, 106

Dwek, E., Arendt, R. G., & Krennrich, F. 2005a, ApJ, 635, 784

Dwek, E., & Krennrich, F. 2005, ApJ, 618, 657

Dwek, E., Krennrich, F., & Arendt, R. G. 2005b, ApJ, 634, 155

Dwek, E., & Krennrich, F. 2013, APh, 43, 112

Edelstein, J., Bowyer, S., & Lampton, M. 2000, ApJ, 539, 187

Elbaz, D., Cesarsky, C. J., Chanial, P., et al. 2002, A&A, 384, 848

Elvey, C. T., & Roach, F. E. 1937, ApJ, 85, 213

Fazio, G. G., Ashby, M. L. N., Barmby, P., et al. 2004, ApJS, 154, 39

Fernandez, E. R., & Zaroubi, S. 2013, MNRAS, 433, 2047

Finkbeiner, D. P., Davis, M., & Schlegel, D. J. 1999, ApJ, 524, 867

Finkbeiner, D. P., Davis, M., & Schlegel, D. J. 2000, ApJ, 544, 81

Finke, J. D., Razzaque, S., & Dermer, C. D. 2010, ApJ, 712, 238

Fitzpatrick, E. L. 1999, PASP, 111, 63

Flagey, N., Boulanger, F., & Verstraete, L., et al. 2006, A&A, 453, 969

Flaherty, K. M., Pipher, J. L., Megeath, S. T., et al. 2007, ApJ, 663, 1069

Franceschini, A., Rodighiero, G., & Vaccari, M. 2008, A&A, 487, 837

Frayer, D. T., Huynh, M. T., Chary, R., et al. 2006, ApJ, 647, L9

Gaensler, B. M., Madsen, G. J., Chatterjee, S., & Mao, S. A. 2008, PASA, 25, 184

Gao, J., Jiang, B. W., & Li, A. 2009, ApJ, 707, 89

Gilmore, G., & Reid, N. 1983, MNRAS, 202, 1025

Gilmore, G., Madau, P., Primack, J. R., Somerville, R. S., & Haardt, F. 2009, MNRAS, 399, 1694

Gilmore, G., Somerville, R. S., Primack, J. R., & Domínguez, A. 2012, MNRAS, 422, 3189

Girardi, L., Croenewegen, M. A. T., Hatziminaoglou, E., & da Costa, L. 2005, A&A, 436, 895

Gondhalekar, P. M. 1990, in: Bowyer, S. and Leinert Ch. (eds.) Galactic and Extragalactic Background Radiation, Proc. of IAU Symposium No. 139. Kluwer, Dordrecht, p. 49

Gorjian, V., Wright, E. L., & Chary, R. R., 2000, ApJ, 536, 550

Gueymard, C., Myers, D., Emery, K. 2002, Solar Energy, 73, 443

Guhathakurta, P., & Tyson, J. A. 1989, ApJ, 346, 773

Guy, J., Renault, C., Aharonian, F. A., et al. 2000, A&A, 359, 419

Hanner, M. S., Weinberg, J. L., DeShields, L. M., II, Green, B. A., & Toller, G. N. 1974, J.Geophys. Rev., 79, 3671

Hauser, M. G., Arendt, R. G., Kelsall, T., et al. 1998, ApJ, 508, 106

Hauser, M. G., & Dwek, E. 2001, ARA&A, 39, 249

Henyey, L. G., & Greenstein, J. L. 1941, ApJ, 93, 70

Hinshaw, G., Weiland, J. L., Hill, R. S., et al. 2009, ApJS, 180, 225

Ienaka, N., Kawara, K., Matsuoka, Y., et al. 2013, ApJ, 767, 80

Indebedouw, R., Mathis, J. S., Babler, B. L., et al. 2005, ApJ, 619, 931

Inoue, Y., Inoue, S., Kobayashi, M. A. R., et al. 2013, ApJ, 768, 197

Ishiguro, M., Yang, H., Usui, F., et al. 2013, ApJ, 767, 75

Jiang, B. W., Gao, J., Omont, A., Schuller, F., & Simon, G. 2006, A&A, 446, 551

Jones, A. P., Duley, W. W., & Williams, D. A. 1990, QJRAS, 31, 567

Jura, M. 1979, ApJ, 227, 798

Kashlinsky, A., Arendt, R. G., Ashby, M. L. N., et al. 2012, ApJ, 753, 63

Kashlinsky, A., Arendt, R. G., Mather, J., & Moseley, S. H. 2005, Nature, 438, 45

Kawada, M., Baba, H., Barthel, P. D., et al. 2007, PASJ, 59, 389

Kelsall, T., Weiland, J. L., Franz, B. A., et al. 1998, ApJ, 508, 44

Kneiske, T. M., Bretz, T., Mannheim, K., & Hartmann, D. H. 2004, A&A, 413, 807

Kneiske, T. M., & Dole, H. 2010, A&A, 515, A19

Kondo, T., Ishihara, D., Kaneda, H., et al. 2016, AJ, 151, 71

Lagache, G., Haffner, L. M., Reynolds, R. J., & Tufte, S. L., 2000, A&A, 354, 247

Laureijs, R. J., Mattila, K., & Schnur, G. 1987, A&A, 184, 269

Lawrence, A., Warren, S. J., Almaini, O., et al. 2007, MNRAS, 379, 1599

Lehner, N., Howk, C., & Wakker, B. P. 2015, ApJ, 804, 79

Leger, A., & Puget, J. L. 1984, A&A, 137, L5

Lehtinen, K., & Mattila, K. 1996, A&A, 309, 570

Leinert, Ch., Grun, E. 1990, interplanetary Dust, in: Physics and Chemistry in Space, Schwenn, R. and Marsch, E. (eds.) - Space and Solar Physics 20. Springer, Berlin, Heidelberg, p. 207

Leinert, Ch., Bowyer, S., Haikala, L. K., et al. 1998, A&AS, 127, 1

Levenson, L. R., Wright, E. L., & Johnson, B. D. 2007, ApJ, 666, 34

Levenson, L. R., & Wright, E. L. 2008, ApJ, 683, 585

Li, A., & Greenberg, J. M. 1997, A&A, 323, 566

Li, A., & Draine, B. T. 2001, ApJ, 554, 778

Lillie, C. F., & Witt, A. N. 1976, ApJ, 208, 64

Low, F. J., Beintema, D. A., Gautier, T. N., et al. 1984, ApJ, 278, L19

Lutz, D. 1999, in The Universe as Seen by ISO, Vol. 427, ed. P. Cox & M. Kessler (Noordwijk: ESA Special Publ.), 623

Madau, P., & Pozzetti, L. 2000, MNRAS, 312, L9

Magner, T. J. 1987, Opt. Eng., 26, 264

Malhotra, S. 1995, ApJ, 448, 138

Mann, I., Köhler, M., Kimura, H., Cechowski, A.,& Minato, T. 2006, A&ARv, 13, 159

Mapelli, M., & Ferrara, A. 2005, MNRAS, 364, 2

Mather, J. C., Cheng, E. S., Eplee, JR., R. E., et al. 1990, ApJ, 354, L37

Mathis, J. S., Rumpl, W., & Nordsieck, K. H. 1977, ApJ, 217, 425

Mathis, J. S., Mezger, P. G., & Panagia, N. 1983, A&A, 128, 212

Mathis, J. S., & Whiffen, G. 1989, ApJ, 341, 808

Mathis, J. S. 1996, ApJ, 472, 643

Matsumoto, T., Kawada, M., Murakami, H., et al. 1996, PASJ, 48, L47

Matsumoto, T., Kim, M. G., Pyo, J., & Tsumura, K. 2015, ApJ, 807, 57

Matsumoto, T., Matsuura, S., Murakami, H., et al. 2005, ApJ, 626, 31

Matsumoto, T., Seo, H. J., Jeong, W.-S., et al. 2011, ApJ, 742, 124

Matsuoka, Y., Ienaka, N., Kawara, K., & Oyabu, S. 2011, ApJ, 736, 119

122

Matsuura, S., Matsumoto, T., & Matsuhara, H. 1995, Icarus, 115, 199

Matsuura, S., Shirahata, M., Kawada, M., et al. 2011, ApJ, 737, 2

Matsuura, S., et al. 2014, "Joint Planetary and Astronomical Science with the Solar Power Sail Spacecraft." Trans. JSASS, Aerospace Tech. Japan, 12, ists29, Tr_1

Mattila, K. 1970, A&A, 9, 53

Mattila, K. 1979, A&A, 78, 253

Mattila, K. 2006, MNRAS, 372, 1253

Maurer, A., Raue, M., Kneiske, T., et al. 2012, ApJ, 745, 166

Mazin, D., & Raue, M. 2007, A&A, 471, 439

Meyer, M., Raue, M., Mazin, D., & Horns, D. 2012, A&A, 542, A59

Mie, G. 1908, Anp, 330, 377

Mishchenko, M. I., Travis, L. D., & Mackowski, D. W. 1996, JQSRT, 55, 535

Murakami, H., Baba, H., Berthel, P., et al. 2007, PASJ, 59, 369

Murthy, J., Henry, R. C., & Sujatha, N. V. 2010, ApJ, 724, 1389

Nakanishi, H., & Sofue, Y. 2003, PASJ, 55, 191

Nesvorný, D., Jenniskens, P., Levison, H. F., et al. 2010, ApJ, 713, 816

Nishiyama, S., Tamura, M., Hatano, H., et al. 2009, ApJ, 696, 1407

Onaka, T., Yamamura, I., Tanabé, T., Roellig, T. L., & Yuen, L. 1996, PASJ, 48, L59

Onaka, T., Matsuhara, H., Wada, T., et al. 2007, PASJ, 59, 401

Ootsubo, T., Onaka, T., Yamamura, I., et al. 2000, Adv. Space Res., 25, 2163

Ootsubo, T., et al. 2009, in ASP Conf. Ser., 418, AKARI, a Light to Illuminate the Misty Universe, ed. T. Onaka et al. (San Francisco: ASP), 395

Ootsubo, T., Doi, Y., Takita, S., et al. 2016, PASJ, 68, 35

Orr, M. R., Krennrich, F., & Dwek, E. 2011, ApJ, 733, 77

Paley, E. S., Low, F. J., McGraw, J. T., Cutri, R. M., & Rix, H.-W. 1991, ApJ, 376, 335

Papovich, C., Dole, H., Egami, E., et al. 2004, ApJS, 154, 70

Penzias, A. A. & Wilson, R. W. 1965, ApJ, 142, 419

Perryman, M. A. C., de Boer, K. S., Gilmore, G., et al. 2001, A&A, 369, 339

Purcell, E. M., & Pennypacker, C. R. 1973, ApJ, 186, 705

Perlmutter, S., Aldering, G., Goldhaber, G., et al. 1999, 517, 565

Pyo, J., Matsumoto, T., Jeong, W.-S., & Matsuura, S. 2012, ApJ, 760, 102

Reach, W. T., Franz, B. A., Weiland, J. L., et al. 1995, Nature, 374, 521

Riess, A. G., Filippenko, A. V., Challis, P., et al. 1998, AJ, 116, 1009

Salvaterra, R., & Ferrara, A. 2003, MNRAS, 339, 973

Sano, K., Kawara, K., Matsuura, S., et al. 2015, ApJ, 811, 77

Sano, K., Kawara, K., Matsuura, S., et al. 2016a, ApJ, 818, 72

Sano, K., Matsuura, S., Tsumura, K., et al. 2016b, ApJ, 821, L11

Sano, K. & Matsuura, S. will be submitted

Schlegel, D. J., Finkbeiner, D. P., & Davis, M. 1998, ApJ, 500, 525

Schmidt, B. P., Suntzeff, N. B., Phillips, M. M. 1998, ApJ, 507, 46

Schroedter, M. 2005, ApJ, 628, 617

Sellgren, K., Werner, M. W., & Dinerstein, H. L. 1992, ApJ, 400, 238

Sellgren, K., Werner, M. W., & Allamandola, L. J. 1996, ApJS, 102, 369

Shirahata, M., Arai, T., Battle, J., et al. 2016, SPIE, 9904

Siebenmorgen, R., & Krügel, E. 1992, A&A, 259, 614

Skrutskie, M. F., Cutri, R. M., Stiening, R., et al. 2006, ApJ, 131, 1163

Smoot, G. F., Bennett, C. L., Kogut, A., et al. 1992, ApJ, 396, L1

Spiesman, W. J., Hauser, M. G., Kelsall, T., et al. 1995, ApJ, 442, 662

Stecker, F. W., Malkan, M. A., & Scully, S. T. 2006, ApJ, 648, 774

Stecker, F. W., Scully, S. T., & Malkan, M. A. 2016, ApJ, 827, 6

Steinacker, J., Pagani, L., Bacmann, A. & Guieu, S. 2010, A&A, 511, A9

Struve, O. 1943, ApJ, 98, 129

Tanaka, M., Matsumoto, T., Murakami, H., et al. 1996, PASJ, 48, L53

Tazaki, R., Tanaka, H., Okuzumi, S., Kataoka, A., & Nomura, H. 2016, ApJ, 823, 70

Tokunaga, A. T., & Vacca, W. D. 2005, PASP, 117, 421

Thompson, R. I., Eisenstein, D., Fan, X., Rieke, M., & Kennicutt, R. C. 2007, ApJ, 666, 658

Totani, T., Yoshii, Y., Iwamuro, F., Maihara, T., & Motohara, K., 2001, ApJ, 550, L137

Trumpler, R. J. 1930, PASP, 42, 214

Tsumura, K., Battle, J., Bock, J., et al. 2010, ApJ, 719, 394

Tsumura, K., Matsumoto, T., Matsuura, S., et al. 2013a, PASJ, 65, 119

Tsumura, K., Matsumoto, T., Matsuura, S., et al. 2013b, PASJ, 65, 120

Tsumura, K., Matsumoto, T., Matsuura, S., et al. 2013c, PASJ, 65, 121

Tsumura, K., Arimatsu, K., Egami, E., et al. 2014, ApJ, 789, 122

van de Hulst, H. C., & de Jong, T. 1969, Phy, 41, 151

Wainscoat, R. J., Cohen, M., Volk, K., Walker, H. J., & Schwartz, D. E. 1992, ApJS, 83, 111

Wang, S., Gao, J., Jiang, B. W., Li, A., & Chen, Y. 2013, ApJ, 773, 30

Wang, S., Li, A., & Jiang, B. W. 2015, ApJ, 811, 38

Weingartner, J. C., & Draine, B. T. 2001, ApJ, 548, 296

Witt, A. N., Lindell, R. S., Block, D. L., & Evans, R. 1994, ApJ, 427, 227

Witt, A. N., Mandel, S., Sell, P. H., Dixon, T., & Vijh, U. P. 2008, ApJ, 679, 497

Witt, A. N., Oliveri, M. V., & Schild, R. E. 1990, AJ, 99, 888

Wright, E. L. 1998, ApJ, 496, 1

Wright, E. L., & Reese, E. D. 2000, ApJ, 545, 43

Wright, E. L. 2001, ApJ, 553, 538

Wright, E. L. 2004, NewAR, 48, 465

Wright, E. L., Eisenhardt, P. R. M., Mainzer, A. K., et al. 2010, AJ, 140, 1868

Xu, C. K., Donas, J., Arnouts, S., et al. 2005, ApJ, 619, L11

Yang, H., & Ishiguro, M. 2015, ApJ, 813, 87

Yue, B., Ferrara, A., Salvaterra, R., Xu, Y., & Chen, X. 2013, MNRAS, 433, 1556

Zagury, F., Boulanger, F., & Banchet, V. 1999, A&A, 352, 645

Zemcov, M., Smidt, J., Arai, T., et al. 2014, Science, 346, 732

Zubko, V., Dwek, E., & Arendt, R. G. 2004, ApJS, 152, 211